

**STRESS INTENSITY FACTOR DEPENDENCE OF HG-AL LIQUID METAL  
EMBRITTLMENT**

by

**SCOTT G. KELLER**  
B.S. University of Central Florida, 2008

A thesis submitted in partial fulfillment of the requirements  
for the degree of Master of Science in Mechanical Engineering  
in the Department of Mechanical, Materials and Aerospace Engineering  
in the College of Engineering and Computer Science  
at the University of Central Florida  
Orlando, Florida

Fall Term  
2009

Major Professor: Ali P. Gordon

© 2009 Scott G. Keller

## ABSTRACT

When high strength aluminum alloys are subjected to liquid metals, physical and chemical reactions ensue resulting in what is known as liquid metal embrittlement (LME). A subset of environmentally-assisted cracking, LME is exhibited when a liquid metal, e.g. Hg or Ga, comes into intimate contact with a solid metal having significant susceptibility. As mechanical loads are applied, the interaction between the two metals results in a reduction in the flow properties of the solid metal. Several theories have been proposed to identify the underlying microstructural failure mechanism; however, none have been widely accepted, as failures can typically incorporate features common to several failure theories. In an effort to confirm, extend or replace the physically-based theories, fracture mechanics experiments on Al 7075-T651 in liquid mercury have been conducted. Experiments were conducted in a custom environmental chamber capable of exposing specimens to liquid environments while applying a mechanical load. Through both plane-strain fracture and stress intensity factor-dependent (SIF) tests, fracture toughness values along with incubation periods were analyzed and provided data for a load-based theory of LME. These mechanical test data, along with metallographic analysis, show that the phenomena of LME is both strongly time- and SIF-dependent.

To my big sisters, Joanne and Elizabeth

Thank you for your guidance,  
support and motivation in my academic adventures

## ACKNOWLEDGMENTS

This work would not have been possible without the help and support of several individuals. Their contributions have helped to form this thesis and I am truly grateful for their assistance.

First and foremost, my advisor, Dr. Ali P. Gordon, deserves much credit. Through his guidance, teachings, editing and most importantly his patience, I was able to labor through the theoretical and experimental portions required by this work. He provided support every step of the way, at all hours of the day (even night!). Dr. Gordon has truly made a lasting impression on my academic career and future. In no way could any of this have been possible without his support and expertise.

Several experiments were conducted during the course of this research, several of which were assisted by a friend and colleague, Justin Karl. Throughout the experimental portions of this work, Justin assisted in every way possible. His unique insight on experimental techniques proved to be extremely useful in the completion of this study.

Additional support was provided by an undergraduate student, Adriano Rampolla, as he assisted in several areas of this work, including some of the photographs presented. The metallurgical analysis was greatly aided by Kirk Scammon, a research engineer at the UCF Materials Characterization Facility. His guidance and discussions provided the skills necessary to operate the SEM and EDX equipment used during the course of this work.

Lastly, my family deserves just as much credit as the others. Without their love and support in every facet of my life, I would not be where I am today. I am truly blessed to have the family that I have and I cannot say thanks enough!

# TABLE OF CONTENTS

LIST OF FIGURES .....	viii
LIST OF TABLES .....	xiv
LIST OF NOMENCLATURE .....	xv
CHAPTER ONE: INTRODUCTION.....	1
1.1 BACKGROUND AND MOTIVATION .....	1
1.2 RESEARCH OBJECTIVES .....	3
CHAPTER TWO: BACKGROUND .....	5
2.1 INTRODUCTION TO FRACTURE MECHANICS .....	5
2.2 FRACTURE BEHAVIOR OF AL 7075-T651 IN AIR .....	12
2.3 STRESS CORROSION CRACKING .....	16
2.4 LIQUID METAL EMBRITTLEMENT .....	21
2.5 PREVIOUS LIQUID METAL EMBRITTLEMENT RESEARCH .....	30
2.6 FOCUS OF CURRENT RESEARCH .....	35
CHAPTER THREE: EXPERIMENTAL METHOD .....	38
3.1 MECHANICAL TESTING .....	38
3.2 FRACTURE TESTING .....	39
3.3 MATERIAL SELECTION .....	43
3.4 FRACTURE SPECIMEN PREPARATION .....	46
3.5 ENVIRONMENTAL BATH .....	52
3.6 ROUTINES AND METHODS .....	56
3.7 MODIFICATIONS .....	61

3.8 METALLURGICAL ANALYSIS .....	66
CHAPTER FOUR: EXPERIMENTAL RESULTS .....	70
4.1 CRACK MOUTH OPENING DISPLACEMENT .....	70
4.2 FRACTURE TOUGHNESS TESTING IN AIR .....	73
4.3 FRACTURE TOUGHNESS TESTING IN SALTWATER .....	76
4.4 FRACTURE TOUGHNESS TESTING IN LIQUID MERCURY .....	80
4.5 STRESS INTENSITY FACTOR INCUBATION .....	85
CHAPTER FIVE: DISCUSSION .....	90
5.1 CRACK MOUTH OPENING DISPLACEMENT .....	90
5.2 FRACTURE TOUGHNESS IN AIR .....	91
5.3 FRACTURE IN SALTWATER .....	94
5.4 FRACTURE IN LIQUID MERCURY .....	96
5.5 INCUBATION EXPERIMENTS IN LIQUID MERCURY .....	103
CHAPTER SIX: CONCLUSIONS .....	113
CHAPTER SEVEN: FUTURE WORK .....	116
7.1 MOTIVATION .....	116
7.2 ADDITIONAL SOLID-LIQUID COUPLES .....	117
7.3 CRACK INITIATION STUDIES.....	119
APPENDIX A: INCUBATION SPECIMEN DATA.....	122
APPENDIX B: SEM IMAGES .....	131
LIST OF REFERENCES .....	143

## LIST OF FIGURES

Figure 1.1: A heat exchanger that employs liquid metal as the working fluid in extracting heat from heated microchips .....	2
Figure 1.2: Fracture of aluminum alloy 5083-H111 in air (top) and in liquid mercury (bottom), Krupowicz, 1989 .....	2
Figure 2.1: Mode I – Opening (left), Mode II – Shearing (center) and Mode III – Tearing (right) .....	6
Figure 2.2: Tensile fracture specimens: Compact, C(T) (left) and Circular (right) .....	9
Figure 2.3: Fracture surfaces of Al 7075-T651 in air at two magnifications (present work) .....	13
Figure 2.4: Fatigue crack growth rates of Al 7075-T651 in air (Kapp, et al., 1986 and Kolman et al., 2002) .....	14
Figure 2.5: Effect of humidity level on fatigue crack growth rates of Al 7075-T651 in air (Speidel, 1975) .....	15
Figure 2.6: Transition from fatigue pre-cracking to fast fracture, revealing characteristic features of each (present work) .....	16
Figure 2.7: Catastrophic failure of a Liberty Ship hull during the WWII era (Sanford, 2003) .....	17
Figure 2.8: Cycles endured until crack initiation in Al 7075-T7651 in two environments (Gordon et al., 1986) .....	19
Figure 2.9: Crack tip velocities in Al 7075-T651 immersed in 3.5% NaCl solution (Jiang, 2009) .....	20
Figure 2.10: Competition between oxidation and LME (Wheeler et al., 1989) .....	21
Figure 2.11: Image of failed rotor surface revealing copper-filled cracks (Lynch, 2003) .....	22
Figure 2.12: Embrittler atom, B, attacking the bond A-A <sub>0</sub> and lowering the cohesive strength .....	23
Figure 2.13: Adsorption Induced Dislocation Emission Model, as proposed by Lynch, 1977.....	26
Figure 2.14: Example of experimental setup used in liquid metal testing, similar to Krupowicz, 1989 .....	31

Figure 2.15: Slow strain rate tests on aluminum specimen in (top) air and (bottom) liquid Hg (Krupowicz, 1989)	32
Figure 2.16: Temperature dependence of diffusivity of mercury in aluminum (Sawayanagi and Hasiguti, 1978)	33
Figure 2.17: Crack tip velocities reported on Al 7075-T651 in the S-L orientation	35
Figure 3.1: MTS Insight 5 (left) and Servohydraulic (right) load frames	39
Figure 3.2: MTS Clip-On Gage used in measuring the crack tip opening displacement of a C(T) specimen with knife edges	41
Figure 3.3: Top-down view of a fracture specimen (S-L-13) displaying the location of the pre-crack measurements	43
Figure 3.4: Cold-rolled sheet of Al 7075 – T651 used in the fracture experiments (left) with associated grain orientation (right)	44
Figure 3.5: Safety equipment in use during experimental setup	45
Figure 3.6: Specimen dimension requirements for C(T) specimen used in plane-strain fracture toughness testing, as per ASTM E399	46
Figure 3.7: Clevis dimension requirements used in plane-strain fracture toughness testing of C(T) specimens, as per ASTM E399	47
Figure 3.8: Adapter designed to attach the clevis to the MTS load frame during fracture testing. All units are in inches	48
Figure 3.9: C(T) specimen dimensions used in the fracture toughness testing. All units are in inches	49
Figure 3.10: Crack plane orientation code for Rectangular Sections, as per ASTM E399	49
Figure 3.11: Fracture specimen surface as obtained after machining, with a surface roughness of <math><64R_a</math>	51
Figure 3.12: Specimen surface after sanding and polishing with 1 $\mu\text{m}$ alumina powder	52
Figure 3.13: Cutaway view of the assembled fracture chamber with specimen	53
Figure 3.14: Cutaway view of the assembled fracture chamber with specimen secured in load frame	55
Figure 3.15: Inexpensive dummy specimen used in validation testing	57

Figure 3.16: Specimen subjected to pre-soaking routine	58
Figure 3.17: Environmental chamber secured in load frame during saltwater testing	59
Figure 3.18: Pre-soaking of specimen in Hg prior to pre-cracking routines	60
Figure 3.19: Failed specimen where crack propagated through knifed-edge	61
Figure 3.20: Close-up image of knifed-edge revealing an increase in stresses	62
Figure 3.21: Modified specimen with rounded valley in knifed-edge	62
Figure 3.22: FEA results from static analysis around pin hole	63
Figure 3.23: Failure of specimen through load pin hole	64
Figure 3.24: Specimen dipped in PlastiDip, covering load pin hole	64
Figure 3.25: Specimen sprayed with PlastiDip, within clevis tolerance	65
Figure 3.26: Pure mercury (left) compared with Al contaminated mercury (right)	66
Figure 3.27: Digital microscope image of several cracks emanating from notch	67
Figure 3.28: Fatigue striations, shown at 2500x magnification, are a result of cyclic loading (S-L-23)	69
Figure 3.29: EDX graph which details the materials present on the fracture surface of a specimen (S-L-11)	69
Figure 4.1: Relationship between crosshead and clip gage displacement readings	71
Figure 4.2: Relationship between SIF and crack length as measured during experimentation	72
Figure 4.3: Fracture specimen fractured in air (S-L-16)	74
Figure 4.4: Low magnification view of fast fracture surface of specimen fractured in air (S-L-16)	75
Figure 4.5: High magnification view of fatigue pre-crack region on specimen fractured in air (S-L-16)	75
Figure 4.6: Close up view of fast fracture surface, displaying intergranular and transgranular cracking of grains and inclusions, respectively (S-L-16)	76

Figure 4.7: Fracture specimen fractured in 3.5% NaCl (S-L-14)	77
Figure 4.8: Low magnification view of fast fracture surface of specimen fractured in 3.5% NaCl (S-L-14)	78
Figure 4.9: Magnified view of fast fracture surface of specimen fractured in 3.5% NaCl with salt residue remaining on fracture surface (S-L-14)	79
Figure 4.10: Magnified view of fast fracture surface, displaying intergranular and transgranular cracking of grains and inclusions, respectively, in 3.5% NaCl (S-L-14)	79
Figure 4.11: Specimen fractured in a liquid Hg environment (S-L-11)	82
Figure 4.12: Multiple crack initiation sites along EDM starter notch (S-L-11)	82
Figure 4.13: Region A, from Fig. 4.11, magnified to show transition between failure modes (S-L-11)	83
Figure 4.14: Fatigue pre-crack region of a specimen tested in liquid Hg, with large transgranular crack (S-L-11)	84
Figure 4.15: Fast fracture surface of a specimen fractured in liquid Hg (S-L-26)	84
Figure 4.16: Time required for complete failure of a specimen based on an initial SIF value	86
Figure 4.17: Side view of a specimen incubated in liquid Hg (S-L-30)	87
Figure 4.18: Intergranular flake from specimen incubated in liquid Hg (S-L-30)	87
Figure 4.19: Fast fracture surface of an incubated specimen in liquid Hg (S-L-26)	88
Figure 4.20: Detailed view of Region A from Fig. 4.19, displaying transgranular-like cleavage fracture (S-L-26)	89
Figure 4.21: Fast fracture surface of an incubated specimen in liquid Hg (S-L-26)	89
Figure 5.1: Comparison of loading rates during fatigue pre-cracking of specimens	91
Figure 5.2: Representative comparison between crack lengths when failure occurs	104
Figure 5.3: Comparison of incubation times for S-L Al 7075-T651 specimens in liquid environments	105
Figure 5.4: Overview of fracture surfaces at the macroscopic level	108

Figure 5.5: Full scale count graph from EDX analysis on a fracture specimen fractured in air (S-L-16) .....	109
Figure 5.6: Full scale count graph from EDX analysis on a fracture specimen fractured in liquid mercury (S-L-11) .....	110
Figure 7.1: Modified experimental chamber with clip gage and heating element additions.....	118
Figure 7.2: Sketch of modified C(T) specimen to be used in 4-pt bending experiments .....	120
Figure 7.3: Machining techniques used to manufacture specimens with various notch radii and identical nominal stresses .....	121
Figure B.1: View of fast fracture surface of a specimen fractured in air .....	132
Figure B.2: View of fast fracture surface of a specimen fractured in air .....	132
Figure B.3: Fatigue pre-crack region of a specimen fractured in air .....	133
Figure B.4: Fatigue pre-crack region of a specimen fractured in air .....	133
Figure B.5: Low magnification of a pre-crack region of a specimen fractured in air .....	134
Figure B.6: Fast fracture region of a specimen fractured in air .....	134
Figure B.7: Fast fracture region of a specimen fractured in 3.5% NaCl .....	135
Figure B.8: Transition region from pre-crack to fast fracture of a specimen fractured in 3.5% NaCl .....	135
Figure B.9: Transition between failure modes of a specimen fractured in liquid Hg.....	136
Figure B.10: Failure of a specimen through the load pin hole in liquid Hg .....	136
Figure B.11: Crack initiation at the load pin hole of a specimen fractured in liquid Hg .....	137
Figure B.12: Crack initiation at the load pin hole of a specimen fractured in liquid Hg .....	137
Figure B.13: Flat surface observed in the fast fracture region of a specimen fractured in liquid Hg .....	138
Figure B.14: Flat surface observed in the fast fracture region of a specimen fractured in liquid Hg .....	138
Figure B.15: View of fast fracture surface of a specimen fractured during an incubation experiment liquid Hg .....	139

Figure B.16: View of fast fracture surface of a specimen fractured during an incubation experiment liquid Hg .....	139
Figure B.17: View of fast fracture surface of a specimen fractured during an incubation experiment liquid Hg .....	140
Figure B.18: Pre-crack region of a specimen fractured during an incubation experiment in liquid Hg .....	140
Figure B.19: Pre-crack region of a specimen fractured during an incubation experiment in liquid Hg .....	141
Figure B.20: Pre-crack region of a specimen fractured during an incubation experiment in liquid Hg .....	141
Figure B.21: Fast fracture region of a specimen fractured during an incubation experiment in liquid Hg .....	142
Figure B.22: Fast fracture region of a specimen fractured during an incubation experiment in liquid Hg .....	142

## LIST OF TABLES

Table 2.1: Fracture Properties of Al 7075-T651, Averages .....	13
Table 3.1: MTS Load Frame Specifications .....	40
Table 3.2: MTS Clip-On Gage – 632.03E-20 .....	42
Table 3.3: Chemical Composition of Al 7075-T651, Wt % .....	44
Table 3.4: Mechanical Properties of Al 7075-T651 (Jiang, 2009) .....	44
Table 3.5: Fracture Properties of Al 7075-T651, Averages (ASM Handbook, 2007) .....	44
Table 4.1: Plane Strain Fracture Toughness Values, $K_{Ic}$ , in Air .....	73
Table 4.2: Plane Strain Fracture Toughness Values, $K_{Ic}$ , in 3.5% NaCl .....	77
Table 4.3: Plane Strain Fracture Toughness Values, $K_{Ic}$ , in Liquid Mercury .....	80

## LIST OF NOMENCLATURE

### Variable

$\varepsilon$	Strain: [ $m/m$ ( $in/in$ )]
$\varepsilon_f$	Fracture strain: [ $m/m$ ( $in/in$ )]
$\nu$	Poisson's ratio: [ $m^2/m^2$ ( $in^2/in^2$ )]
$\sigma$	Stress: [ $MPa$ ( $ksi$ )]
$\sigma_o$	Flow (yield) stress: [ $MPa$ ( $ksi$ )]
$\sigma_y$	Tensile yield stress: [ $MPa$ ( $ksi$ )]
$\sigma_{uts}$	Ultimate tensile stress: [ $MPa$ ( $ksi$ )]
$a$	Crack length: [ $mm$ ( $in$ )]
$a_c$	Critical crack length: [ $mm$ ( $in$ )]
$a_t$	Transitional crack length: [ $mm$ ( $in$ )]
$A_n$	Nominal area: [ $m^2$ ( $in^2$ )]
$B$	Specimen width: [ $mm$ ( $in$ )]
$da/dt$	Crack tip velocity: [ $m/s$ ( $in/s$ )]
$da/dN$	Crack extension per cycle: [ $m/cycle$ ( $in/cycle$ )]
$K$	Stress intensity factor: [ $MPa\sqrt{m}$ ( $ksi\sqrt{in}$ )]
$\Delta K$	Stress intensity factor range: [ $MPa\sqrt{m}$ ( $ksi\sqrt{in}$ )]
$K_c$	Critical stress intensity factor: [ $MPa\sqrt{m}$ ( $ksi\sqrt{in}$ )]
$K_I$	Mode I stress intensity factor: [ $MPa\sqrt{m}$ ( $ksi\sqrt{in}$ )]
$K_{I0}$	Mode I initial stress intensity factor: [ $MPa\sqrt{m}$ ( $ksi\sqrt{in}$ )]
$K_{Ic}$	Mode I plane strain fracture toughness: [ $MPa\sqrt{m}$ ( $ksi\sqrt{in}$ )]

$K_t$	Stress concentration: [ $MPa/MPa$ ( $ksi/ksi$ )]
$P$	Load: [ $N$ ( $lbf$ )]
$r$	Distance from crack tip: [ $mm$ ( $in$ )]
$R_l$	Load ratio, Min/Max: [ $N/N$ ( $lbf/lbf$ )]
$R_s$	Stress ratio, Min/Max: [ $MPa/MPa$ ( $ksi/ksi$ )]
$V_m$	Crack mouth opening displacement: [ $m/m$ ( $in/in$ )]

### **Acronyms**

<i>ASTM</i>	American Standards for Testing and Materials
<i>CCG</i>	Creep Crack Growth
<i>CMOD</i>	Crack Mouth Opening Displacement (aka <i>CTOD</i> )
<i>C(T)</i>	Compact Tension (type of fracture specimen)
<i>CTOD</i>	Crack Tip Opening Displacement (aka <i>CMOD</i> )
<i>DCB</i>	Double Cantilever Beam (type of fracture specimen)
<i>EAC</i>	Environmentally-Assisted Cracking
<i>EDM</i>	Electric Discharge Machined/Machining
<i>FCG</i>	Fatigue Crack Growth
<i>LEFM</i>	Linear-Elastic Fracture Mechanics
<i>LME</i>	Liquid Metal Embrittlement
<i>MVC</i>	Microvoid Coalescence
<i>SCC</i>	Stress Corrosion Cracking
<i>SCG</i>	Static Crack Growth

# CHAPTER 1

## INTRODUCTION

### 1.1 Background and Motivation

Aluminum alloys are commonly used in all facets of engineering design. From structural applications in aerospace to underwater applications on vessels, aluminum alloys have become a top choice when choosing a lightweight, high strength material. The material does, however, have limitations to its uses, as several alloys are susceptible to Environmentally-Assisted Cracking (EAC), such as Stress Corrosion Cracking (SCC) and Liquid Metal Embrittlement (LME). The latter has been of particular interest for several decades, as a significant loss of plastic deformation prior to failure is witnessed.

Aluminum alloys, particularly higher strength alloys such as Al 7075, exhibit susceptibility when in contact with liquid metals. Notably, liquid Mercury (Hg), Gallium (Ga) and Indium (In), when coupled with Al alloys, exhibit various levels of LME severity. These liquid metal couples come about in multiple industries, e.g. petrochemical processing plants, in convective cooling systems in nuclear power applications and microchip cooling, as shown in Fig 1.1. As repeated mechanical loads are imposed and cracks are formed in the solid metal, the reaction between the solid and liquid metal will result in a reduction in ductility and flow properties, Fig 1.2. Researchers have identified various theories regarding the underlying microstructural failure mechanism of LME under stress (Gordon and An, 1982), yet no theory has been widely accepted. When LME is the decided cause of failure, it is usually attributed to a combination of the failure theories.

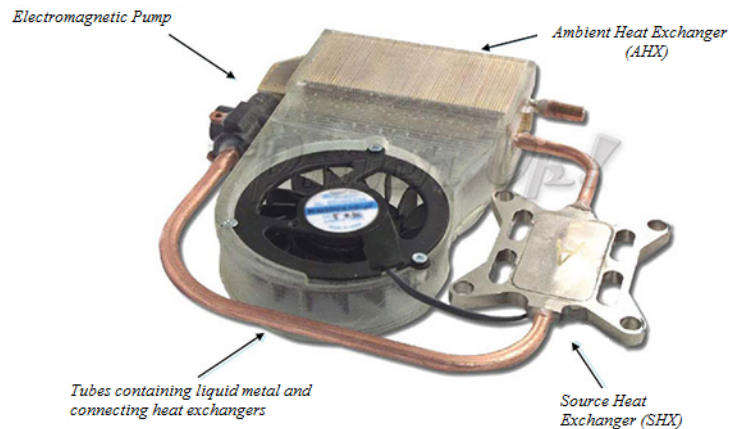


**Figure 1.1:** A heat exchanger that employs liquid metal as the working fluid in extracting heat from heated microchips.

As there is no widely accepted theory, a few key models have been singled out as more valid than others. The models that have received the most notoriety include the Decohesion Model (Stoloff and Johnston, 1963 and Westwood and Kamdar, 1963), Surface Structure Model (Lynch, 1977), Stress-Assisted Dissolution Model (Robertson, 1966 and Glikman et al., 1976) and Grain Boundary Diffusion Model (Krishtal, 1970). Primary interests have been focused around the Decohesion model, but researchers are hesitant to limit all occurrences of LME to this one model.

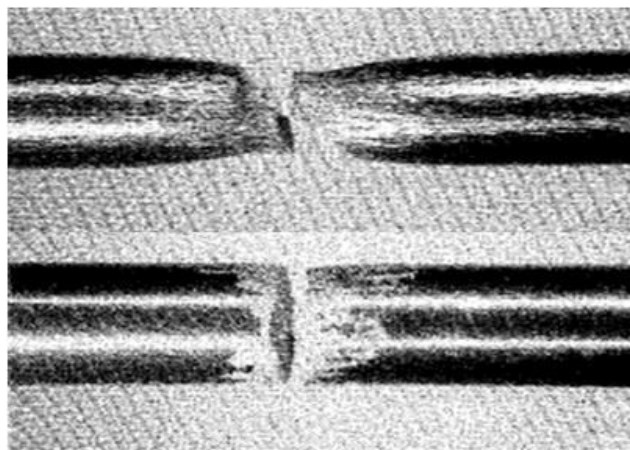


**Figure 1.2:** Fracture of aluminum alloy 5083-H111 in air (top) and in liquid mercury (bottom) (Krupowicz, 1989).

Narrowing down the mechanisms to identify the true underlying cause of LME can be a tedious task. Problems constantly occur with “wetting” of the solid metal with the liquid metal. If any oxidation is formed at the crack tip, the liquid metal will not properly interact with the solid metal, resulting in a failure mechanism other than LME (Joseph et al., 1998). Methods of applying the liquid metal have been investigated, such as those by Gordon and An (1982) and Wheeler et al., 1986 and 1988-89. Even with these methods, researchers have noted that there still exists competition between LME and oxidation at the crack tip (Wheeler et al., 1989).

Determining the underlying microstructural mechanism behind LME has proven to be a cumbersome task. Between supplying an adequate amount of liquid metal to the crack tip to the post-mortem fractographic analysis, no mechanism has been widely accepted. There is also the possibility that the liquid Hg (originally 99.99% pure) becomes less pure as the fracture process progresses. Competition between theories inhibits a complete and definitive answer to cases involving LME and the underlying root of failure.

## **1.2 Research Objectives**

Building upon the work of previous researchers in the area of LME, a new approach to studying LME under stress will be taken. Previous works have carried out test routines that include static tensile tests, fracture tests on notched specimens and delayed failure tests. Regardless of the specimen or test routine used, there were key components missing from the studies. Specifically, these tests did not focus on the cracking of the material under continuous exposure to Hg. Others neglected to study crack propagation under the application of a constant stress intensity factor or to record the time to failure under constant loads. New methods of testing, which incorporate a large supply of Hg available at the crack tip, constant SIF and incubation time tests, will be developed and presented.

- **Develop an environmental chamber capable of continuously exposing specimens to an aggressive environment during testing.** In an effort to have a constant supply of a liquid embrittler at the crack tip, a new chamber must be fabricated. This chamber will allow for the new test regimes to be implemented, all while ensuring that only the liquid embrittler is available to the crack tip. Previous works (Wheeler et al., 1989) suggested that there was a competition between oxidation and LME at the crack tip, therefore the goal is to force LME conditions at all steps of the experiment.
- **Produce load-based control routines used in initial SIF-based incubation experiments.** The objective is to explore how various initial stress intensity factors affect the time to failure of fracture mechanics specimens. Specifically, the routines are desired to apply loads that result in a variety of applied SIF values to aluminum submerged in liquid mercury. Initial results are expected to establish the critical stress intensity factor,  $K_{Ic}$ , followed by the LME threshold,  $K_{ILME}$ . Incubation tests will then provide data regarding the dependence of the applied SIF.
- **Confirm, extend or replace the existing theories regarding the underlying microstructural mechanism behind LME.** Whether the results display characteristics of an existing theory or not, an effort will be made to unify the theories into one. Comparison between existing results and those obtained here will enable a more comprehensive analysis, with more emphasis on the diffusion based properties of LME. Incorporating the new SIF incubation tests will provide vital information that has been lacking from previous research attempts. The overall goal will be to exactly identify the mechanism of crack growth during LME, either by proving/disproving existing theories, or through the development of an entirely new theory.

## **CHAPTER 2 BACKGROUND**

Fracture mechanics, as a discipline, is relatively young when compared to other engineering mechanics. With most of the major developments contributed in the mid-to-late 20<sup>th</sup> century, the field overall is less than 50 years old (Sanford, 2003). Although ancient civilizations fabricated many structures that prevented fracture by designing each member to support compressive loads, the manner in which brittle fractures occurred in normally ductile materials was unknown. Following several events, typically major disasters, researchers scour failed components in an effort to gain knowledge of the failure and to prevent future catastrophes. Through these efforts, fracture mechanics has evolved from simple observations to a fully dedicated field of research and a primary interest to mechanical designers.

### **2.1 Introduction to Fracture Mechanics**

For as long as structures have been built, failed surfaces of materials have been observed. Whether with the naked eye or magnification techniques, analyzing these surfaces provides vital information regarding the failure itself. Early studies on the quality of metallic materials were conducted by Réaumur in 1722, allowing for the assessment and suggestion of material improvements (Lynch, 2006). Major advancements in the observation of the fracture surface came in the 20<sup>th</sup> century, first with optical observation followed by SEM and TEM in the latter half of the century. Observing the surface is merely one technique now used in the study of fracture mechanics.

During the 19<sup>th</sup> and 20<sup>th</sup> centuries, when mechanical designs were becoming more complex and versatile, catastrophic failures started occurring that left engineers searching means by which to avoid future accidents. The train crash of Versailles, in which the front axle failed (through what has later identified as a fatigue failure), was thoroughly researched by Rankine

(Sanford, 2003). Additional failures resulted in significant research; however, it was not until the failure of the Liberty ships in the mid-20<sup>th</sup> century that entirely new safety considerations were made based upon on-going research (Hagedorn and Pardun, 1998).

Many of the advancements of the time were based upon the development of mathematical models of Inglis and Griffith (Sanford, 2003 and Hagedorn and Pardun, 1998). Inglis used the theory of elasticity to solve the problem of an elliptical hole, while Griffith used energy methods to quantify brittle fractures. It was not until the work of Irwin that previous foundations in fracture research were applied to ductile materials (Gordon, 2009). With the application of methods to ductile materials, measures can be taken to avoid catastrophic failures and crack propagation to fracture of ductile engineering materials.

Much of the work contained within this thesis will be based upon the development of Linear Elastic Fracture Mechanics (LEFM) relations. The relations used in LEFM are dependent upon material, geometry and orientation of the specimen (Perez, 2004). Initial importance is directed toward the loading type, Fig. 2.1. The different modes all correspond to a different stress intensity factor (SIF or  $K$ ), where emphasis here will be placed on the Mode I SIF, i.e.  $K_I$ . Mode I specimens are loaded through simple tensile or bend tests, resulting in cracks that are

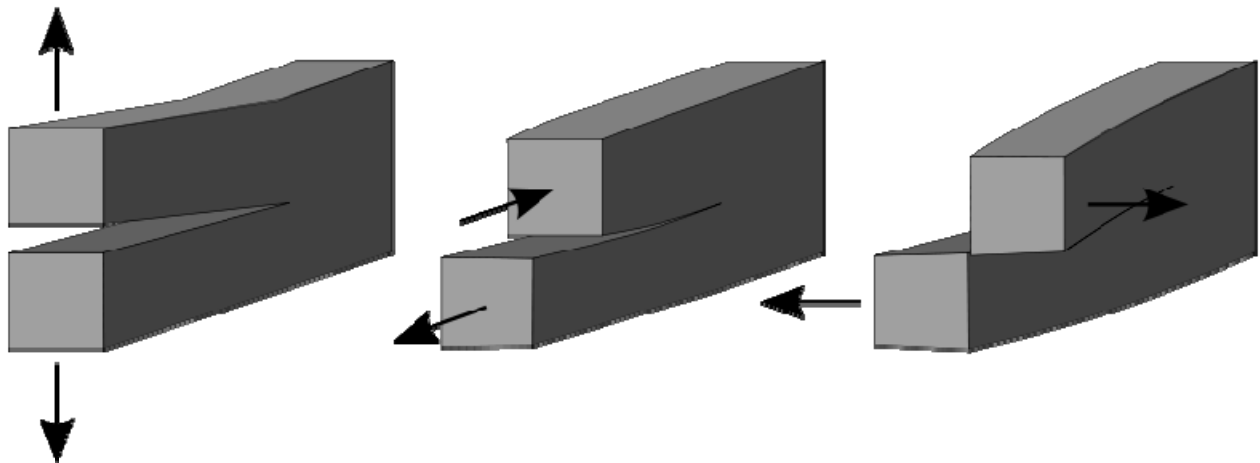


**Figure 2.1:** Mode I – Opening (left), Mode II – Shearing (center) and Mode III – Tearing (right).

expected to propagate perpendicular to the load direction. With the assumption of the path of crack propagation and the ease at which tensile loads can be imposed, Mode I cracks are the most commonly studied through experimental routines.

Several methods have been proposed in study of fracture, focused on energy- and stress-based methods. Often being hard to visualize, the energy relations have given way to the more practical stress field approach (Sanford, 2003). This approach allows for the calculation of stresses at a location relative to the crack tip using geometrical relations and the defining crack tip stress parameter,  $K$ , that is the crack tip driving force under elastic conditions, i.e.,

$$\sigma_x = \frac{K}{\sqrt{2\pi r}} f_x(\theta) + \sigma_{ox} \quad (2.1)$$

$$\sigma_y = \frac{K}{\sqrt{2\pi r}} f_y(\theta) \quad (2.2)$$

$$\tau_{xy} = \frac{K}{\sqrt{2\pi r}} f_{xy}(\theta), \quad (2.3)$$

where  $r$  is the distance from the crack tip,  $f$  is function dependent on  $\theta$ , and  $\sigma_{ox}$  is the constant stress ahead of the crack tip in the x-direction. Investigating crack propagation in ductile materials, independent of the mode, begins with a crack present within a body with a given length,  $a$ . If no cracks are present, the repeated loading encountered during service can possibly generate new cracks, known as fatigue crack initiation. Regardless, when a crack is present, it will propagate at rates strongly dependent upon the applied load history until it reaches a critical crack length, referred to as  $a_c$ . At this point, the crack propagation will become unstable and the component will fail in a brittle manner. Essentially, once  $a_c$  is achieved, the ductile material will fail in a manner similar to a ceramic plate being dropped on the ground (i.e., the pieces can be

reassembled to achieve a shape similar to the initial geometry). Calculating  $K$  involves knowledge of the stress,  $\sigma$ , geometry and crack length, i.e.,

$$K = \sigma \sqrt{\pi a} \cdot f\left(\frac{a}{W}\right), \quad (2.4)$$

where the function  $f(a/W)$  is used to account for geometric concerns of the test specimen implemented. Simple manipulation of Eq. 2.4, disregarding the geometrical function  $f$ , yields the transitional crack length,  $a_t$ , i.e.,

$$a_t = \frac{1}{\pi} \left( \frac{K_c}{\sigma_o} \right)^2, \quad (2.5)$$

where  $\sigma_o$  is the flow (or yield) stress of the material. Once the crack length has reached  $a_t$ , the material can be expected to fail in a brittle manner as opposed to a normal ductile fracture ( $a_t$  will be used instead of the previously mentioned  $a_c$ ) (Dowling, 2007). When this occurs, and the crack has propagated through until failure, the stress intensity factor,  $K$ , becomes the critical stress intensity factor,  $K_c$ , i.e.,

$$K_{@failure} = K_c.$$

This value of the critical stress intensity factor is a material property and extremely important when designing structures to resist fracture.

Obtaining the critical stress intensity factor is done experimentally and is highly dependent upon the specimen used. Fracture toughness testing is conducted through a variety of experiments, most of which involve universal load frames and sensitive metering devices. Additional testing can be done with this setup, including static crack growth and fatigue crack growth tests. Each of these tests are strictly governed by experimental standards, e.g. ASTM, and deserve individualized attention.

### 2.1.1 Fracture Toughness Testing

Fracture toughness testing is the process used in determining the ability of a material to resist fracture. Methods of testing include tensile, bend and impact methods; all of which help to characterize a materials resistance to fracture. In regards to determining the  $K_{Ic}$  of a material, tensile and bend tests are most commonly used. Additionally, Mode I loading conditions are prevalent, as both of these methods lend very well to testing materials in this configuration. Accordingly, test standards have adapted to incorporate both forms of load application (tensile and bending loads) in an effort to achieve conformity of results.

One governing standards organization is the American Society for Testing and Materials (ASTM) International. Producing thousands of standards in a variety of disciplines, ASTM provides detailed standards into the fatigue and fracture of metallic materials. In regards to the fracture toughness, ASTM E399 (1990) is an extremely thorough standard that details proper methods of testing. By adhering to this method, valid  $K_{Ic}$  values of metallic materials can be obtained experimentally.

Standard E399 allows for the use of several test specimens, including bend, compact, arc and disk shaped specimens, with two examples shown in Fig. 2.2. Included for each specimen type are the specimen size requirements; required to ensure plane-strain conditions exist. Any

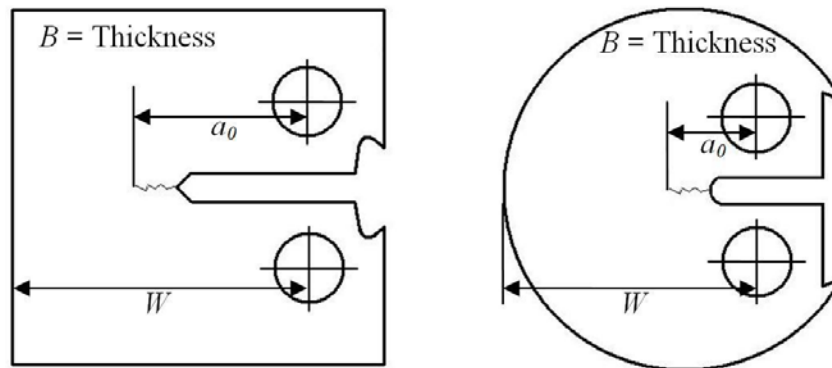


**Figure 2.2:** Tensile fracture specimens: Compact, C(T) (left) and Circular (right).

additional fixturing hardware required for testing is also given. Specific requirements for the specimen type used in this research will be presented in Chapter 3.4. Regardless of the choice, the result of the test should be a valid material property.

Contained within this method are additional procedures for crack length measurement, displacement gage use and calculation/verification of the experimentally obtained critical stress intensity factor. Particularly, the pre-crack generation is necessary in  $K_{Ic}$  testing, which is also outlined in the annex portion E399. While thorough, more detailed standards were developed individually to deal with this particular issue, as in the case of static and fatigue crack growth testing.

### 2.1.2 Static Crack Growth Testing

Static crack growth testing is typically referred to as static, as it is the load or displacement that is being held constant. Through this constant load or displacement, the material tends to creep, causing the material to plastically deform in an effort to reduce the stress on the body. Void nucleation and coalescence can occur, resulting in crack initiation and propagation. Each of these phenomena is highly material dependent.

Utilizing ASTM Standard E1457 (2000) the crack tip velocity can be analyzed. Specimen variety is supported; however, it is suggested that the C(T) specimen be used. Crack propagation can be measured via potential-drop method or crack tip opening displacements (CTOD). Following the procedures, a method for generating  $K$  with respect to crack tip velocity ( $da/dt$  or  $V$ ) data is given under the presence of a static load.

It is noted in the standard that a fatigue pre-crack is suggested, but not required. Specifically, a sharp notch can be generated by electric discharge machining (EDM) or preferably a pre-crack can be generated by fatigue pre-cracking. While useful information can

be obtained through static crack growth experiments, more attention will be given to fatigue crack growth, as it is necessary in both static crack growth tests and plane strain fracture toughness tests.

### 2.1.3 Fatigue Pre-cracking

Regardless of the tests previously mentioned, fatigue pre-cracks are necessary in the investigation of fracture behavior. An EDM machined starter-notch is sufficient to control the location and direction of crack propagation, as defined in both E399 and E1457; however, fatigue pre-cracking provides the infinitesimally small crack tip radius within the body.

The ASTM standard governing fatigue pre-cracking is E647 (2000). All aspects of fatigue pre-cracking, including specimen type and dimensions, acceptable  $R$  values, and crack length measurement are thoroughly covered. Ensuring that subsequent tests can be conducted, the specimen type used in fatigue pre-cracking is suitable for both static pre-cracking and fracture toughness testing. This similarity enables a multitude of experiments to be completed on the same specimen.

Working with C(T) specimens, the fixturing apparatus is the same as the one used in both E399 and E1457. Given the dimensions on the specimen, only one setup is required and multiple routines can be programmed to test the specimen. Specific details regarding the test speed and acceptable  $da/dN$  rates are detailed, providing methods for pre-cracking specimens with rates of  $da/dN$  greater or less than  $10^{-8}$  m/cycle. The difference between the two rates is the test control; i.e., whether the test is controlled through a constant-force-amplitude (large plastic zone ahead of crack tip) or constant-displacement-amplitude (small plastic zone ahead of crack tip). Each test provides slightly different results, but ultimately a fatigue pre-crack is generated.

The most important aspect mentioned is that when one routine is followed for a specimen, the routine must remain the same for all subsequent tests. One cannot cycle a specimen through constant-force-amplitude tests and then others through constant-displacement-amplitude, unless this is an explicit goal of the study. The differences will be noticeable in subsequent tests, creating uncertainty in results. Overall, following one pre-cracking routine will establish uniformity and lead to more precise conclusions.

## **2.2 Fracture Behavior of Al 7075-T651 in Air**

The fracture behavior of a material in ambient conditions must be established before any environmental effects can be accounted for. This characterization will provide a basis for comparison between all successive testing conducted in environments. Key elements in the characterization include both static and cyclic effects. A further discussion on each is necessary and provided in subsequent sections, while material composition and additional mechanical properties are provided in Section 3.3.1.

### 2.2.1 Static Behavior

Static characterization, in terms of fracture experiments, includes tensile, compressive and static crack growth rate experiments. The directional tensile properties are fully detailed in Table 3.4. While compression tests can be done, there is considerable difficulty in obtaining values of its compressive strength (Papirno et al., 1983). As such, compressive properties will not be included as this study on fracture behavior in corrosive environments does not focus on compressive loading.

Plane strain fracture toughness values have been obtained and reported by methods of ASTM standards, Table 2.1. Orientations of the grain boundary are provided, ranging from the orientation of least fracture resistance to the highest. These orientations will be further discussed

**Table 2.1 – Fracture Properties of Al 7075-T651, Averages** (ASM Handbook, 2007)

Orientation	S-L	T-L	L-T
Fracture Toughness, $K_I$ [MPa-m <sup>1/2</sup> (ksi-in <sup>1/2</sup> )]	17.6 (16.0)	24.2 (22.0)	28.6 (26.0)

in Section 3.3.1. Specifically, the S-L orientation is the weakest in terms of strength and fracture resistance. Additionally, it is the orientation that has the least amount of published data in regards to mechanical behaviors.

Regarding the static crack growth rates, it was found that there were little-to-no major studies conducted on crack growth rates under static loads on Al 7075 in air. As in designs that involve static loads, the use of a sufficient safety factor prevents crack formation and propagation. Consequently, the formation of cracks is more commonly studied under the presence of cyclic loading (Romaniv et al., 1976). Unlike steels and other select materials, static crack growth in Al 7075 has not been as widely studied as much as other alloys.

Scanning electron microscopy images have been used to analyze the fracture surfaces of Al 7075 fractured in laboratory air [Ramulu and Taggart, 1986]. The bulk of the cracking is intergranular along the grain boundaries of the material. Fracture surfaces at two levels of magnification display the typical mode of fracture and fatigue striations, Fig. 3 (present work).

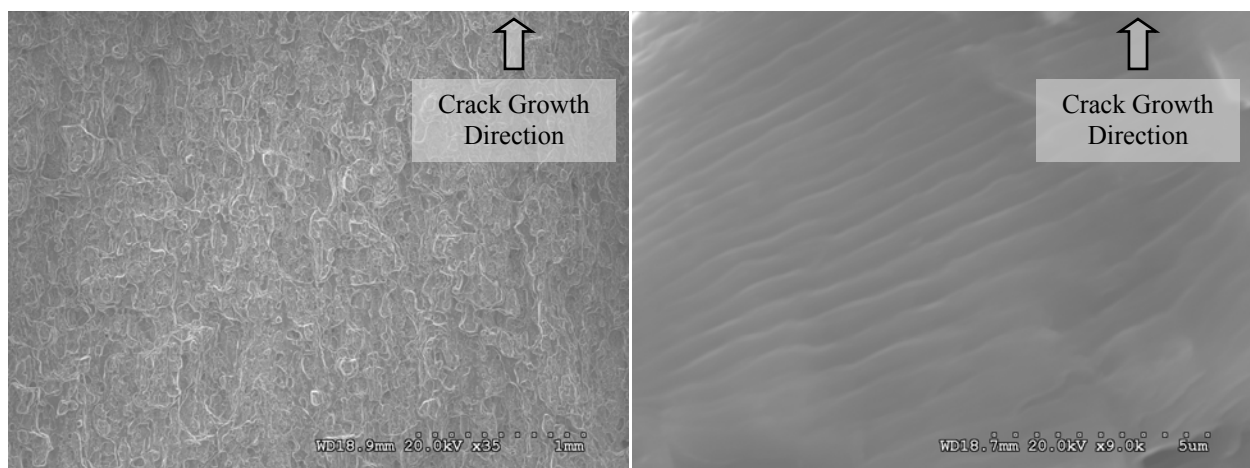


**Figure 2.3:** Fracture surfaces of Al 7075-T651 in air at two magnifications (present work).

## 2.2.2 Cyclic Behavior

Fatigue crack growth rate experiments are far more prevalent for all tempers of Al 7075, including the temper T651. Almost all investigations into the fracture behavior include detailed information regarding the crack growth rates. Usually, this is the first step taken in establishing a baseline value in studies that involve a particular environmentally-assisted cracking (EAC) mechanism. Results are typically reported as  $\Delta K$  versus  $da/dN$  or  $\Delta K$  versus  $da/dt$  graphs.

Fatigue crack growth rates, in terms of extension per cycle, in air at ambient temperatures have been studied by Kapp et al. (1986) as well as at elevated temperatures by Kolman et al. (2002). It was shown in this study that there was no effect of loading frequency on fatigue crack growth in air but at slightly elevated temperatures, crack growth rates per cycle are smaller, Fig. 2.4. The crack growth rate was solely dependent upon the applied  $\Delta K$  for a given temperature (Kapp et al., 1986). This allows for the proper determination of  $\Delta K$  when conducting load controlled FCG experiments on Al 7075-T651 in accordance with ASTM E647.

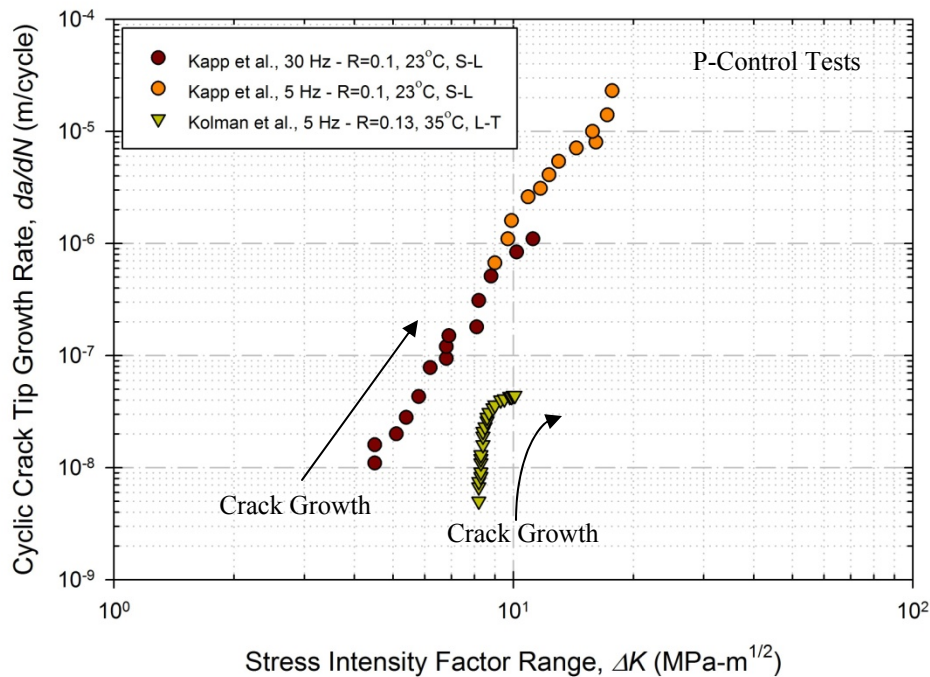


**Figure 2.4:** Fatigue crack growth rates of Al 7075-T651 in air (Kapp, et al., 1986 and Kolman et al., 2002).

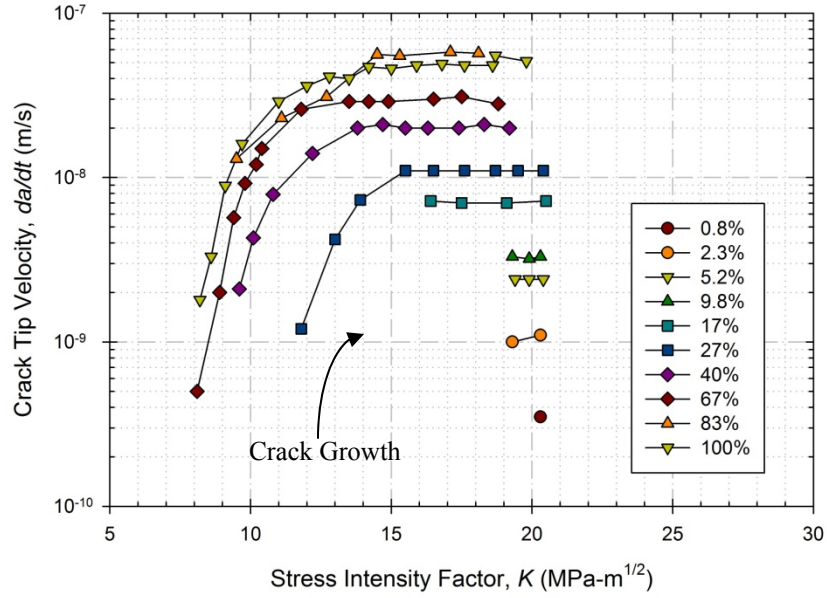


**Figure 2.5:** Effect of humidity level on fatigue crack growth rates of Al 7075-T651 in air (Speidel, 1975).

Crack growth rates, in terms of crack tip velocity, are more commonly reported in FCG experiments. A comprehensive study was done, examining what affect the level of humidity in air had on the crack tip velocity (Speidel, 1975). It was shown that as the level of humidity existing in the air increases, the crack tip velocity increases, Fig. 2.5. For all levels of humidity, there is a plateau value seen for crack tip velocity, which also increased with increasing humidity. Maximum crack tip velocities in air were observed to be around  $1.28 \cdot 10^{-5}$  m/s ( $5.04 \cdot 10^{-5}$  in/s) at an 83% humidity level.

Fractographic analyses have shown that fatigue fracture initiates along grain boundaries. Upon fast fracture, the surface reveals that a more brittle failure occurs, as exhibited by cleavage-like fracture characteristics, e.g. river marks [ASM, 2007]. This has been confirmed in the present study, as the transition from fatigue pre-cracking to fast fracture contains both beach marks and cleavage like features, respectively, Fig. 2.6.

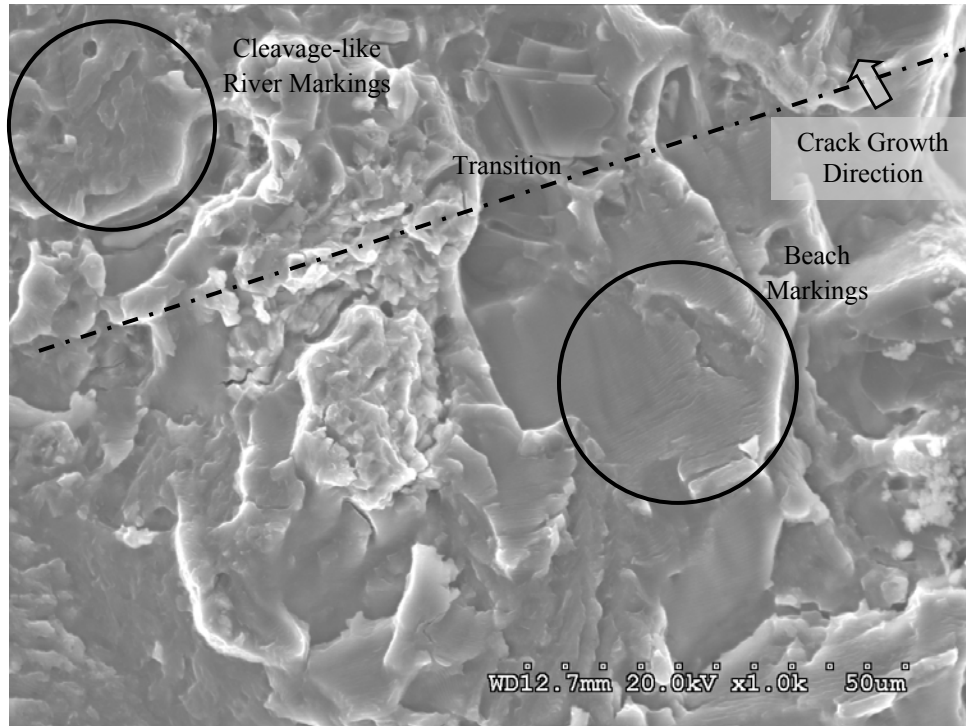


**Figure 2.6:** Transition from fatigue pre-cracking to fast fracture, revealing characteristic features of each (present work).

The latter study, conducted by Speidel (1975), leads way to the phenomena of stress corrosion cracking (SCC). Through the introduction of a solution other than pure air, different mechanical behaviors are observed. This is a special field and requires a separate discussion.

### 2.3 Stress Corrosion Cracking

When materials come into contact with particular solutions, liquid or aqueous, the mechanical behavior can drastically change. As shown in Fig. 2.5, even the addition of moisture in ambient air increases the crack tip velocity by orders of magnitude. This phenomenon, known as stress corrosion cracking (SCC), is a result of a chemical reaction between the solid metal and the surrounding environment. Extensive research has been conducted as a result of failures of mechanical systems due to SCC; some of which have led to catastrophic failure with the loss of lives.

### 2.3.1 Notable Failures

As mentioned in a previous section, the through-hull failures of the Liberty ships helped to usher in fracture mechanics as a science (Sumpter and Kent, 2004). These particular failures, caused by propagation of cracks at weld points, were assisted by colder temperatures and the interaction between the saltwater environment (3.5% NaCl) and the microstructure of the hull steel. These failures were widely publicized, as pictures of the failures were extremely remarkable, Fig. 2.7.

A lesser-known failure, that of an F-16 in 1992, was deemed a failure as a result of an unforeseen SCC issue (Lynch, 2003). Specifically, the failure of a lever arm was a result of the interaction of a through pin (Nitronic 60) used on a vane-positioning arm (IN718) and a chloride-rich environment. Designers failed to account for susceptibility of Nitronic 60 to SCC, which led to the pilot ejecting and the plane crashing. Fortunately, no loss of life was sustained and designers have since replaced the pin with that of a different material, IN625 (Lynch, 2003).

More commonly known is the failure of a commercial passenger airliner in 1988. In this event, Aloha Airlines flight 243 suffered a disastrous failure, in which a portion of the upper



*Figure 2.7: Catastrophic failure of a Liberty Ship hull during the WWII era (Sanford, 2003).*

fuselage peeled away from the aircraft. During flight, at approximately 24,000ft, a portion of the fuselage opened up along the top seam. The design of the aircraft was to allow for a slow decompression and to maintain the integrity of the plane; however, the design considerably helped in the failure.

The initial failure was that of a bonding adhesive used in the lap joint, which resulted in larger-than-normal hoop stresses on the rows of rivets. Over time, the rivets were cycled through several cycles as the cabin was pressurized and de-pressurized. Coupled with the corrosive saltwater environment, fatigue and corrosion caused a coalescence of cracks, in turn, ripping the skin off the fuselage. It was shown that there was a 4.57 m (180 in) crack generated, which gave rise to the damage to the plane and the loss of a life (Johnson, 1991).

Whether the failure resulted in the loss of life or not, the effects of SCC are widely known. The few examples provided here, in the maritime and aerospace industries, are just a small number of SCC characterized failures. Collectively, SCC failures have generated extensive research programs to understand the underlying failure mechanisms. In light of this research and the similarity to LME, the SCC behavior of Al7075-T651 is carefully studied.

### 2.3.2 Stress Corrosion Cracking of Aluminum Alloys

Stress corrosion cracking has been observed in all types of materials, including steels and aluminum alloys. In terms of aluminum alloys, it is known that higher strength alloys, 2XXX and 7XXX, display more susceptibility to SCC (Gordon et al., 1986 and Speidel, 1975). During mechanical loading, all aspects of failure, from crack initiation to crack tip velocity and time to failure, are seen to increase with exposure to a corrosive environment.

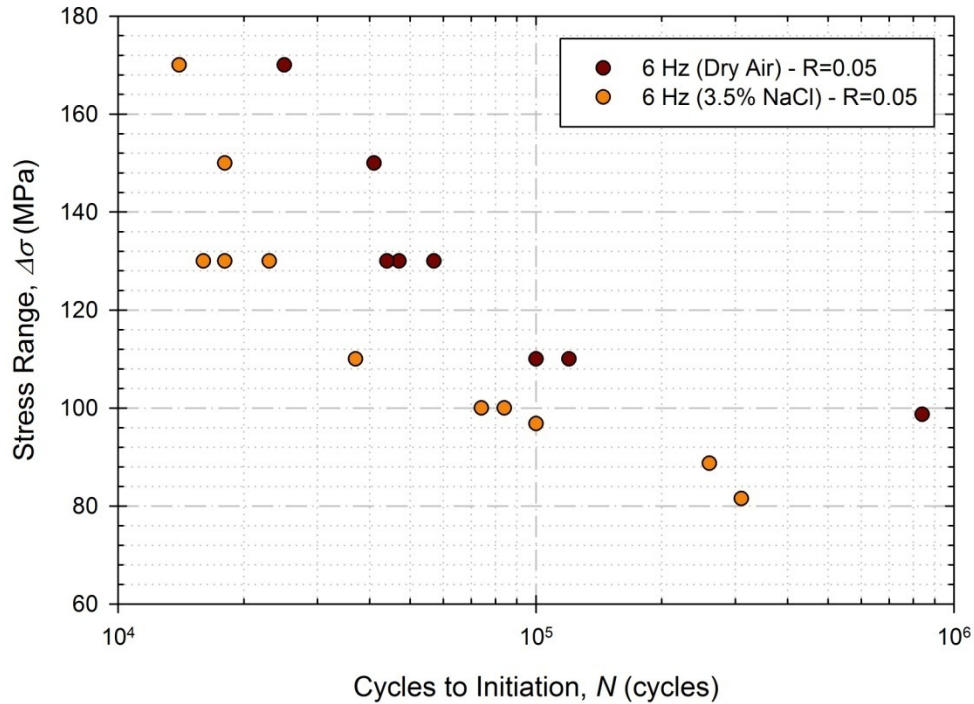


**Figure 2.8:** Cycles endured until crack initiation in Al 7075-T7651 in two environments (Gordon et al., 1986).

Crack initiation over a given stress range provides evidence that a microstructural failure mechanism is at work. In studying crack initiation, it is seen that the crack initiation resistance was lower for specimens exposed to 3.5% NaCl, Fig. 2.8 (Gordon et al., 1986). Using identical load histories, the environment significantly affected the specimen by reducing the number of cycles required for crack initiation. At lower stress ranges, it is seen that the number of cycles to crack initiation in 3.5% NaCl is less than a third of those required in air. Not only is the formation of cracks affected, but the velocity of the crack tip is considerably increased, although the authors do not provide any evidence to support an initiation mechanism. It is merely noted that the initiation times are decreased in the presence of a saltwater environment.

Recent studies have compared the crack tip velocity of specimens immersed in 3.5% NaCl to those of specimens in humid air (Jiang et al., 2009). It was found that for similar values of the stress intensity factor, the plateau velocity was greater for specimens immersed in 3.5% NaCl, Fig. 2.9. In a particularly dry environment, the crack tip velocity is observed to be less

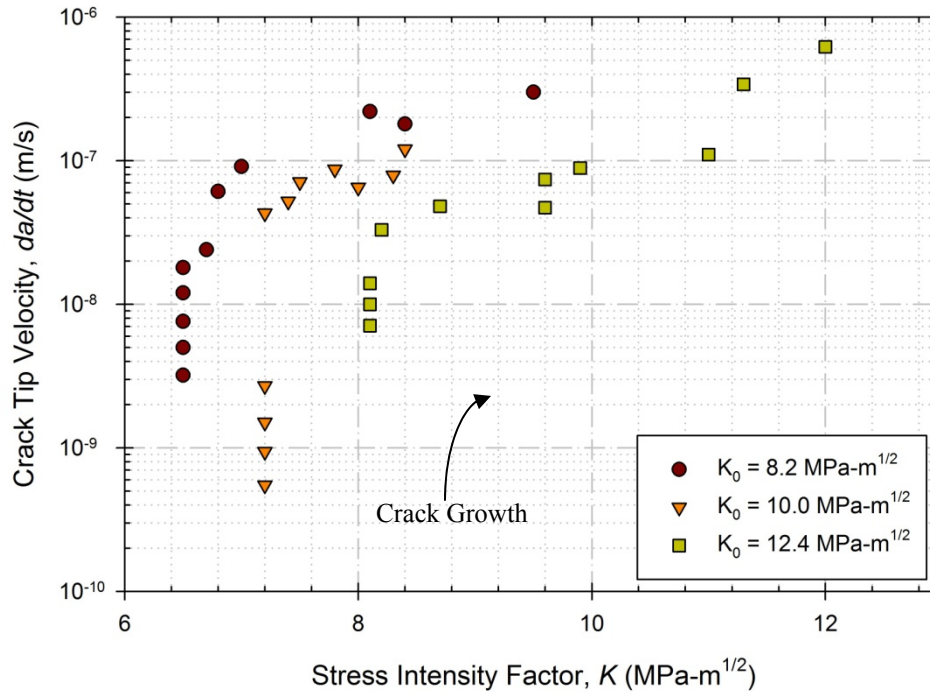


**Figure 2.9:** Crack tip velocities in Al 7075-T651 immersed in 3.5% NaCl solution (Jiang, 2009).

than that of a 3.5% NaCl environment by an order of magnitude, as compared to values obtained in the work by Speidel (Fig. 2.5). Additionally, crack tip velocities are achieved at a lower  $K$ , suggesting chemical interactions contribute to a decrease in the materials ability to resist fracture.

Stress corrosion cracking of higher strength aluminum alloys is a considerable concern, as nearly all (90%) SCC failures occur in three alloys; 7075-T6, 7079-T6 and 2024-T3 (Speidel et al., 1975). With the susceptibility to SCC established (but not necessarily fully understood), other substances are called into question, particularly, how these high strength alloys would behave in a more corrosive environment, such as liquid metals. Liquid metals are regarded as an embrittling agent in these alloys and present the phenomena known as liquid metal embrittlement (LME).

## 2.4 Liquid Metal Embrittlement

Through intimate contact with a liquid metal, a solid metal used in a structural component can fail prematurely. When this failure occurs, fracture surfaces can reveal a brittle fracture surface, void of dimples and other features associated with ductile fractures. The absence of plastic flow in the material is a result of the interaction between the liquid and solid metal and the failure is classified as liquid metal embrittlement (LME).

The effects of LME have been well observed in both research and practical settings. Failures have ranged from chemical plants to aircraft components. In 1987, an ethylene plant experienced a failure in an aluminum pipe weld due to exposure to liquid mercury (English and Korbin, 1989). It was noted that mercury does not wet aluminum well as a result of oxide formation, Fig. 2.10, but in the event of corrosion, fatigue and other events, wetting can occur. Once it does, this wetting forms amalgams in the grain boundaries, thus reducing the load carrying capability of the material.

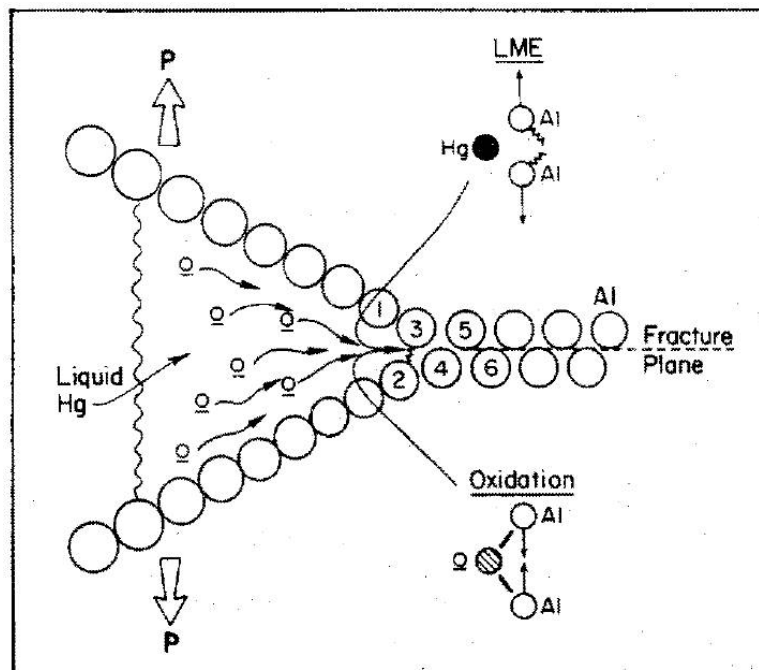
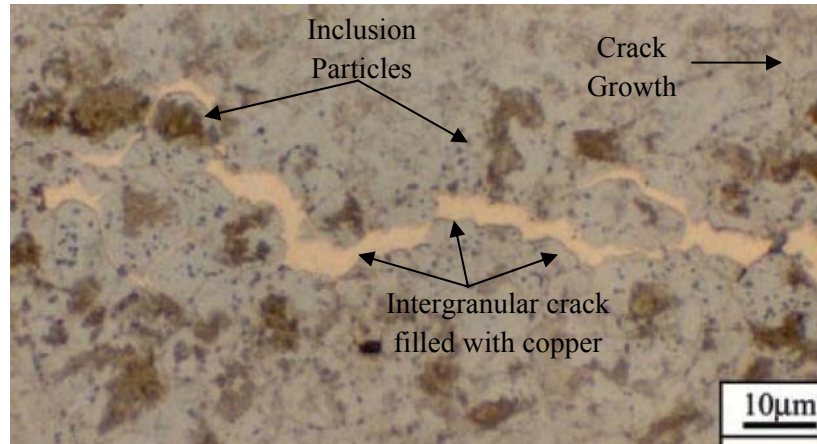


Figure 2.10: Competition between oxidation and LME (Wheeler et al., 1989).



**Figure 2.11:** Image of failed rotor surface revealing copper-filled cracks (Lynch, 2003).

Another failure, that of an aircraft brake rotor, was classified as a liquid metal induced failure (Lynch, 2003). Although there was no surrounding liquid metal, copper that was used as a plating material on the rotor was heated past the melting point during excessive braking. The result was such that the steel rotor absorbed the liquid copper, resulting in a loss of strength and, ultimately, failure of the brake rotor. Evidence of this was shown in subsequent SEM/EDS analyses (Fig. 2.11).

Attention to liquid metal induced failures is necessary even if liquid environments are not present or are in trace concentrations. As seen in the failure of the brake rotor, not properly accounting for the full operating range of temperatures can result in LME failures. Not only are these failures unexpected, they can occur rapidly. When experimenting with LME crack tip velocities, it was observed that the velocity can be on the order  $10^{-3}$  m/s ( $3.93 \cdot 10^{-2}$  in/s) when the SIF is merely 10% of  $K_{Ic}$ , for a variety of solid-liquid couples (Lynch, 1994). Compared with the crack tip velocities previously shown (Figs. 2.5, 2.9), this is a significant increase.

Understanding the microstructural mechanisms behind LME has been the focus of several researchers. Currently, there is no single mechanism that has been identified and widely

accepted by the research community. Instead, several variations on the microstructural mechanism have been proposed, with four models gaining the most recognition.

#### 2.4.1 Microstructural-based Models

Throughout the 1900s, several researchers developed theories on the failure mechanism that drives LME. Of particular interest are four key models that were developed: Decohesion Model (Stoloff and Johnston, 1963 and Westwood and Kamdar, 1963), Stress Assisted Dissolution Model (Robertson, 1966), Grain Boundary Diffusion Model (Krishtal et al., 1973) and the Adsorption Induced Dislocation Emission Model (Lynch, 1977). Each model details the microstructural process at work and how failures can be analyzed.

Of the most widely accepted is the Decohesion Model that was proposed by both Stoloff and Johnston (1963) and Westwood and Kamdar (1963). Additionally, these two research groups were influenced by their previous works and the work of Nichols and Rostoker (1961). In dealing with the surface energy of the liquid-solid couple, the embrittling liquid would ultimately lower the cohesive strength of the solid metal, allowing for failure at a lower tensile stress, Fig. 2.12.

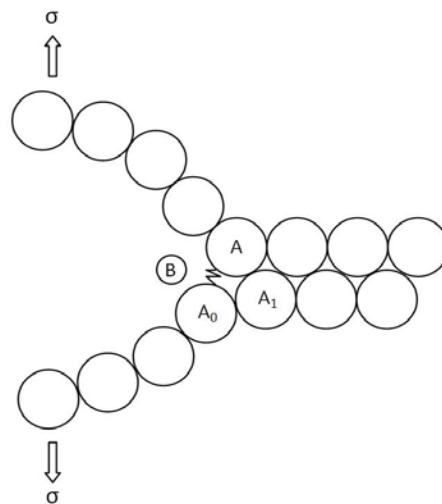


**Figure 2.12:** Embrittler atom, B, attacking the bond A-A<sub>0</sub> and lowering the cohesive strength.

A major component behind this mechanism is the free energy relationship that was originally developed by Griffith. The externally applied stress required to extend a crack in an elastic material can be written as

$$\sigma_f = \frac{E_0 \lambda_0}{4\pi a_0} \sqrt{\frac{a_0}{c}}, \quad (2.6)$$

where  $E_0$  is the elastic modulus,  $\lambda_0$  is a parameter to describe the force interaction between A-A<sub>i</sub>,  $a_0$  is the equilibrium distance between atomic planes A, and  $c$  is the crack length. This equation can then be modified to incorporate the surface energy term,  $\gamma_0$ , e.g.,

$$\sigma_f = \sqrt{\frac{E_0 \gamma_0}{2c}}. \quad (2.7)$$

Equation 2.7 incorporates the effects of the plastic deformation, which during brittle fracture is no longer valid as the crack tip will be extended past the atomic spacing,  $a_0$ . To account for this, Eq. 2.6 is modified to instead adjust the surface energy term, thus multiplying it through, i.e.,

$$\sigma_f = \sqrt{\frac{E_0 \gamma_0}{c} \cdot \frac{\rho}{a_0}}. \quad (2.8)$$

The consequence of this theory is that the shear stresses experienced are remaining unchanged, but the normal stress to cause failure is reduced. Ultimately, it was the relation between normal and shear stress,  $\sigma/\tau$ , within the body that governed the transition from ductile to brittle fracture.

A possible method to disprove this mechanism would be a detailed fractographic analysis. By comparing samples fractured in air and liquid metal environments, evidence (or lack thereof) of a complete brittle fracture would be necessary. If any appreciable amount of deformation is observed, even in localized situations as in the case of microvoid coalescence (MVC), the validity of this theory would be lessened.

Following this work was the work of Robertson, 1966, and later refined by Glickman, 1977, which proposed the Stress-Assisted Dissolution Model. Through this work, both researchers used energy terms coupled with stress calculations to determine the crack tip velocity in liquid-solid metals, i.e.,

$$v = \left( \frac{C_0 D \Omega^2 \gamma}{kT} \right) \frac{1}{r^2} \left( \frac{2L\sigma_a^2}{E\gamma} - 1 \right), \quad (2.9)$$

where  $C_0$  is the equilibrium concentration of liquid in the unstressed solid,  $D$  is the diffusion coefficient,  $\Omega$  is the atomic volume of the solid,  $\gamma$  is the solid-liquid interfacial energy,  $k$  is the Boltzmann constant,  $T$  is the temperature,  $r$  is the distance from the crack tip,  $L$  is the crack length,  $\sigma_a$  is the applied stress and  $E$  is the elastic modulus of the solid. Essentially, the role of the liquid is to dissolve the solid at the crack tip and remove material. Thus, the fluid acts as a transporter of solid atoms, leaving the solid weaker. Crack tip velocities were confirmed, including what were considered high velocities.

To prove or disprove this theory, an analysis on the embrittler should be conducted; particularly, a chemical analysis to determine the composition before and after experiments. The theory is supported by dissolution of the solid metal into the liquid metal. If there exists an appreciable amount of solid metal traces within the liquid metal, this theory is a possibility; however, if there is not, then the notion that the liquid metal is solely a transport mechanism for solid metals is invalid.

Following Robertson and Glickman, the research team led by Krishtal aimed to develop a model that dealt with the diffusion of the liquid into the solid along the grain boundaries of the solid. This model was aptly termed the Grain Boundary Diffusion Model. Essentially, the liquid would diffuse into the solid via grain boundaries, thus embrittling the solid. Loads applied would then allow for the propagation of cracks along the grain boundary until failure. Fracture

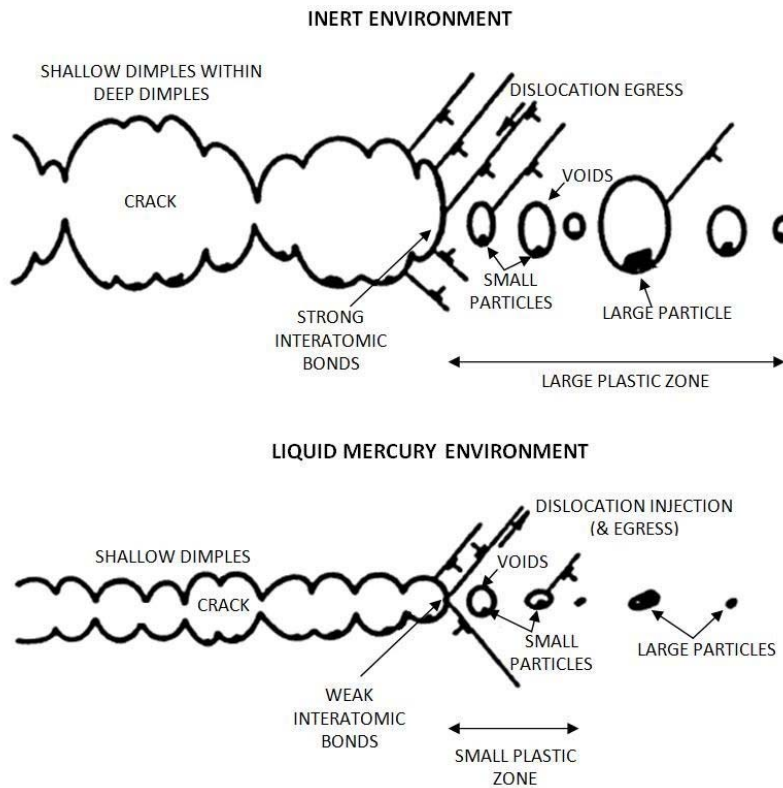


*Figure 2.13: Adsorption Induced Dislocation Emission Model, as proposed by Lynch, 1977.*

of aluminum was studied by the diffusion of impurity atoms along the grain boundaries, embrittling the solid and resulting in brittle failures. The main theory was that fracture would occur along the grain boundaries that were attacked by the impurities atoms.

Efforts to determine the validity of this theory could be made through the use of spectroscopy at all levels of magnification. Particularly, SEM images of the fracture surface could be used to determine if the crack propagated by intergranular or transgranular means. If cracking is observed throughout the grain, then the argument for this failure mechanism would be difficult to be made.

Lastly of the most generally accepted mechanisms is the mechanism proposed by Lynch, known as the Adsorption Induced Dislocation Emission Model. Working along the lines of the Decohesion model, Lynch viewed specimens under SEM and drew the conclusion that there was

some plastic flow ahead of the crack tip, albeit reduced when compared to fractures in air. Through adsorption of the liquid metal, nucleation and egression of dislocations at the surface is facilitated, microvoids in the solid would be generated and coalesce to propagate the crack, Fig. 2.13. The liquid environment would thus enable plastic flow through shearing of the atomic bonds, opposing the notion of the Decohesion Model that no plastic flow was exhibited.

The model proposed by Lynch is based on the chemisorption at the surface of the solid metal. It is stated that it can be applied to HE, but that this is a more involved case, as hydrogen can readily diffuse into materials. The absorption of liquid metals then would help to disprove the theory in regards to the actual microstructural phenomena; however, this would only disprove the transport portion of this theory. The “detailed fractographic analysis” will still stand to support the localized plastic deformation observed on fracture surfaces.

#### 2.4.2 Strengths of the Models

Each of the theories presented contain specific individual strengths. Disregarding any simplifying assumptions, each proposes a slightly different method of embrittlement which is thought to accurately portray the true failure mechanism.

The Decohesion Model, one of the first and most widely accepted theories regarding LME, presents a relationship between the normal applied stress and the shear stresses exhibited within the material; the  $\sigma/\tau$  relationship. This relationship states that under the application of an external load, the chemical bond between A-A<sub>i</sub> (Fig. 2.12) is strained to a certain extent that allows for the chemisorption of the liquid. Chemisorption within the solid, then, is strain-activated and only several atomic units deep. A sufficient supply of liquid must be present and is the controlling factor of crack tip velocity. This phenomenon can account for high crack tip velocities, as shown in the work of Nichols and Rostoker.

The Adsorption Induced Dislocation Emission Model, essentially a variation on the Decohesion Model, suggests that there is some plastic deformation that was not accounted for in the Decohesion Model. Observations under SEM revealed blunting of the crack tip, therefore microvoid coalescence (MVC) allows for shearing of the atomic bonds. This is in contrast to the Decohesion Model, as it was tensile bonds rupturing that were the root of failure; however, SEM pictographs suggests that there is plastic deformation and MVC, coupled with diffusion, shears bonds leading to failure. Adsorption at the crack tip helps to embrittle the material and provide for crack growth. This theory supports the adsorption of the liquid but provides evidence of plastic deformation; therefore, starting fracture occurs as a shear dislocation as witnessed through SEM observations.

The major strength of the Grain Boundary Diffusion Model is that failures along grain boundaries have exhibited cracks filled with liquid metal, as shown in Fig. 2.11. The liquid metal is able to diffuse until a critical depth. This theory suggests that at the critical depth, the surface energy is reduced along the grain boundaries, weakening the bond and allowing failure to occur. In the event of LME, failures are expected to occur along the grain boundaries of the solid metal.

Finally, the Stress Assisted Dissolution Model provides a model based on the diffusion of solid atoms away from the solid through the liquid metal. Most importantly, it provides a calculation for the crack tip velocity based upon the surface energies of the liquid and solid metal. The analytical model is capable of predicting large crack tip velocities, up to  $10^{-2}$  m/s, as seen in other studies.

### 2.4.3 Weaknesses of the Models

As each of the models have their own strengths, they also have their weakness. While none of the researchers suggested that the conclusions were applicable for every case, there was a level of certainty in their model. There exists a level of doubt for each proposed model of LME.

The Decohesion Model has a weakness in the interaction between the liquid and solid metal atom interaction. In the work done proposing this model, there was no information on the interaction between the atoms. Merely, the theory was that there is some interaction between the liquid atoms and the solid atoms, decreasing the bond strength and the external load required to break this bond. The strain-activated diffusion allows for crack propagation and failure under brittle conditions with limited plasticity; however, no chemical interaction was identified as the sole interaction.

A weakness to the Adsorption Induced Dislocation Emission Model is in regard to the material behavior. Particularly, the adsorption of the liquid should affect the bulk material behavior, which it is suggested that it should not (Wheeler, 1987). The crack propagation during LME can be accounted for through adsorption at the tip; however, the liquid is not absorbed through the entire solid. The unaffected material should behave in the manner consistent with tests conducted in lab air.

A major criticism with the Grain Boundary Diffusion Model regards one of the distinctions that is made to support the mechanism. This model proposes that cracking only occurs along the grain boundary of the solid metal; however, observations have shown otherwise. Particularly, under fixed displacement conditions, fracture in aluminum has shown transgranular cracking when viewing under SEM (Wanhill, 1974 and Kapp et al., 1986). The

observation of transgranular cracking is in contradiction with this model, providing support for a different theory.

Lastly, the Stress Assisted Dissolution Model is affected by the method used to explain embrittlement. It suggests that the liquid removes atoms from the solid and does not diffuse within the solid. Research conducted disproves this notion; again, as shown in Fig. 2.11, liquid metal can be seen within the grain boundaries of the solid. The liquid metal has been shown to diffuse into the solid, invalidating the failure mechanism presented by this model.

## **2.5 Previous Liquid Metal Embrittlement Research**

Several attempts have been made to distinguish the true microstructural failure mechanism of LME. Experimental routines have included tensile (Otto et al., 1962), stress-free diffusion (Sawayanagi and Hasiguti, 1978), static fracture (Wanhill et al., 1974), fatigue crack growth (Kapp et al., 1986) and delayed failure tests (Gordon and An, 1982). Much has been obtained in regards to data; however, results still lead to uncertainty in the active failure mechanism.

### 2.5.1 Tensile Tests

Initial tensile tests dealt with the tensile behavior of wrought aluminum sheets (Otto et al., 1962). Flat sheets were outfitted with drilled holes filled with either mercury or a mercury amalgam. Stresses were applied to the sheet and the degree of embrittlement was noted through the study of cracks present within the material. Experimental results revealed that the heat treatment used in the conditioning of the aluminum greatly affected the susceptibility to LME. Specifically, the higher strength alloys with an optimum heat treatment were the most severely affected grades of aluminum. Ultimately, the tensile strength of the material was significantly reduced with the appropriate wetting conditions by mercury.

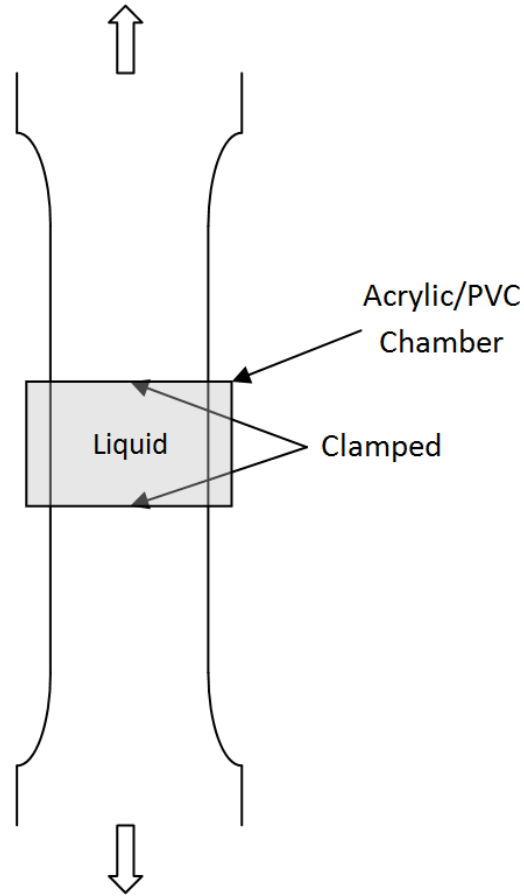


**Figure 2.14:** Example of experimental setup used in liquid metal testing, similar to Krupowicz, 1989.

In agreement that the degree of heat treatment affects the susceptibility to LME, additional tensile studies were conducted on smooth tensile specimens (Malu and Preece, 1973). Prior to loading, smooth specimens were chemically treated to remove the oxide from the surface of the aluminum to allow for the wetting by mercury. Slow strain rate tensile tests were used to test the effect that alloying Al with Mg affects the susceptibility to LME. It was found that mercury does lower the fracture stress of aluminum; however, Mg decreases flow of the material creating a more brittle fracture.

The degree of brittle fracture was studied using smooth specimens on various metals, including aluminum and steel (Krupowicz, 1989). Small environmental test cells were attached to the gage length, which allowed for the exposure of the specimen to liquid mercury, Fig 2.14.

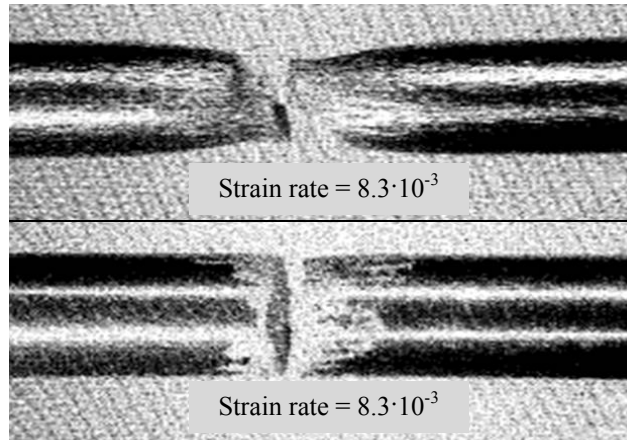


**Figure 2.15:** Slow strain rate tests on aluminum specimen in (top) air and (bottom) liquid Hg (Krupowicz, 1989).

It was seen that the degree of embrittlement was far more severe for aluminum. Secondary cracking was also seen to run along the direction of maximum grain flow, which can give way to cleavage and transgranular crack growth, Fig 2.15.

Further use of slow strain rate tests, measured via strip charts, were conducted on several smooth tensile specimens with liquid mercury contained in tubing secured to the gage length (Kane et al., 1993). It was pointed out that the severity of LME was more aggressive during the slow strain rate tests than constant load tests that were conducted. Additionally, it was noted that a clear difference in the behavior of two aluminum alloys was seen, providing evidence that the alloying materials play a role in the degree of susceptibility to LME.

### 2.5.2 Stress-Free Diffusion

Stress-free diffusion of mercury into aluminum has been studied at elevated temperatures (Sawayanagi and Hasiguti, 1978). A tracer method was used to determine the concentration of Hg in aluminum after a period of diffusion on samples at temperatures between 445°C and 589°C (883°F and 1092°F). Diffusion times varied between 5.5 hours for the highest temperature and 216 hours for the lowest temperature. A linear relationship was obtained regarding the temperature dependence of Hg diffusion, Fig. 2.16. At the lowest temperature, the

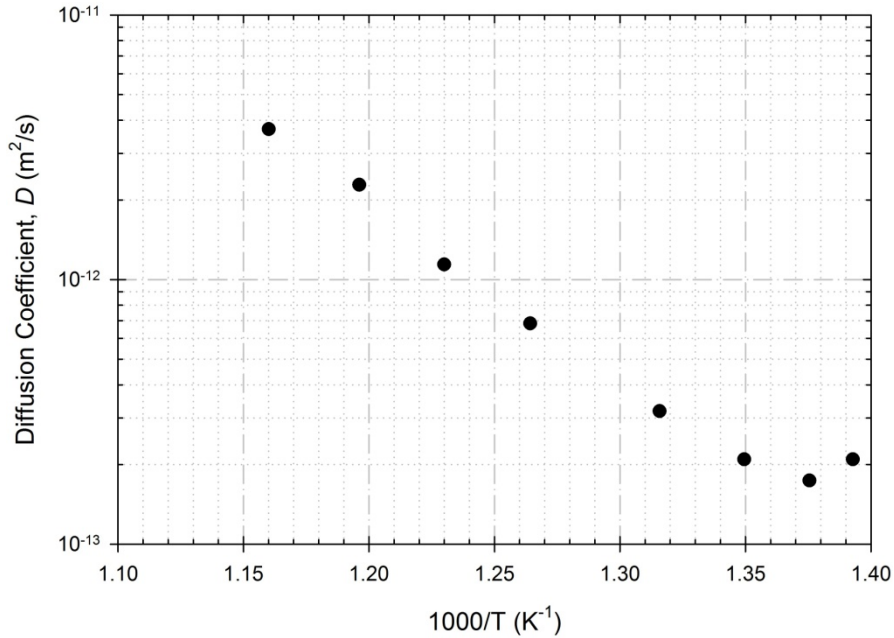


**Figure 2.16:** Temperature dependence of diffusivity of mercury in aluminum (Sawayanagi and Hasiguti, 1978).

diffusion coefficient,  $D$ , was observed to be  $2.09 \cdot 10^{-13} \text{ m}^2/\text{s}$ . Data regarding diffusion at room temperature of mercury into aluminum was not discussed, nor was it readily available in literature. Investigation in the application of this model for room temperature diffusion needs to be conducted to estimate ingress depths at ambient temperatures.

### 2.5.3 Incubation Behavior

Few researchers have addressed constant load tests in an effort to study either crack initiation or crack growth in the presence of liquid mercury. In earlier works, time-to-failure routines were used in determining the location and severity of LME cracking (Nichols and Rostoker, 1961). Results from this work suggested that time-to-failure studies were dominated by incubation time and that failure occurred quickly afterward. Other tests were used in the studying of crack propagation in addition to crack initiation (Gordon and An, 1982). These experiments confirmed the results, using both liquid and solid metals, the incubation period comprises a majority of the test time, with failure occurring almost instantaneously.

#### 2.5.4 Fracture Tests

Fracture testing has increasingly become the most common method of studying crack initiation, growth and fracture behavior. Using fracture specimens, fatigue crack growth rates and the propagation velocities are commonly used to characterize how severely the solid metal is embrittled by the liquid metal.

Bend specimens were used to study the extent of cleavage and transgranular cracking in aluminum alloys, including Al 7075-T6 (Wanhill, 1974). Fractographic analysis revealed that there was extensive transgranular cracking coupled with intergranular fracture along grain boundaries. Crystallographic planes {100}, {110}, {111} all revealed cleavage, providing data that the surface energies do not differ greatly between planes. Final observations concluded that even the smallest amounts of liquid mercury were able to create extremely high crack tip velocities (0.1 m/s) and catastrophic failure, as long as enough mercury was available at the progressing crack tip.

Utilizing compact tension, C(T), specimens, fatigue crack growth rates and thresholds have been extensively studied. Particularly, with S-L oriented specimens, research has shown low thresholds and high crack propagation rates, based on load- and displacement controlled tests. Crack velocities have been reported at a plateau of  $10^{-2}$  m/s (0.4 in/s) at SIFs of less than one (Benson and Hoagland, 1989) using gallium as the embrittler, while plateau velocities of  $10^{-1}$  m/s (4 in/s) have been observed for SIFs between 2 and 13 MPa-m<sup>1/2</sup> (1.83 and 11.9 ksi-in<sup>1/2</sup>) (DCB specimens with  $W=3.83$  cm,  $B_1=0.95$  cm and  $B_2=1.27$ cm) using liquid mercury (Kapp, 1986), Fig. 2.17.

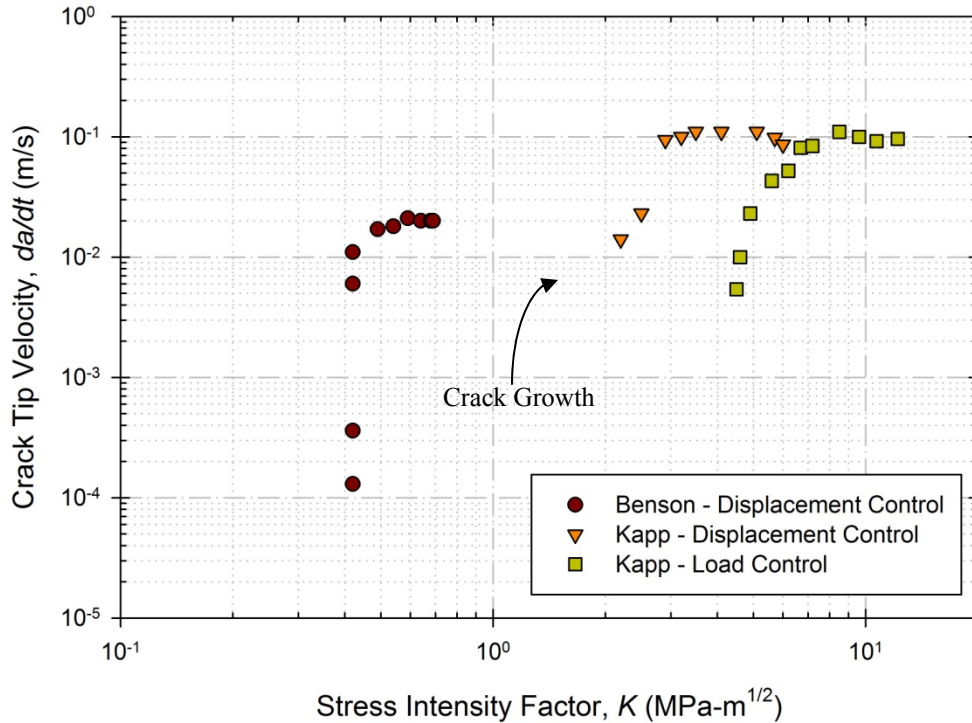


**Figure 2.17:** Crack tip velocities reported on Al 7075-T651 in the S-L orientation.

Double cantilevered beam (DCB) specimens are useful in studying the rate of propagation. Implementing specimens in the L-T and T-L orientations, crack tip velocities were studied through load-arrest tests (Liu and Hoagland, 1989 and Wheeler et al., 1989). Crack velocities were seen to plateau at varying ranges, even though experiments were conducted by the same research group. It was determined that oxide formation at the crack tip inhibited the process of LME, hence why faster velocities were not observed (Wheeler et al., 1989). Regardless, crack tip velocities are orders greater in liquid metal environments than in air or saltwater.

## 2.6 Focus of Current Research

Upon careful examination of previous research efforts, experimental routines will be developed to test the susceptibility of a high strength aluminum alloy to LME. Fracture

specimens will be utilized in SIF-based fracture experiments conducted in air and liquid mercury environments.

The material of choice will be the high strength alloy, Al 7075-T651. This particular alloy was chosen due to its wide use in engineering designs and mainly its notable susceptibility to LME. Fracture specimens will be machined, in compliance with ASTM E399 for plane-strain fracture toughness testing, out of rolled sheets. Hardness tests will be conducted to ensure similarity to the material used in the tensile test. Specimens will be oriented in the S-L orientation, as this will provide a uniform microstructure at the crack tip and is the weakest orientation in regards to fracture. The uniform microstructure is vital in the study of LME, as many of the models suggest grain boundary interaction as a possible mechanism of failure.

Fracture tests will be conducted in Hg environments to observe LME. Specimens will undergo the same soaking routines in an effort to obtain similar results. Fatigue pre-cracking will be done in both lab air and mercury environments, as will fracturing of the specimen. Results are expected to show an increase in the embrittlement of the material as a result of the exposure to a more corrosive substance.

Addressing main concerns from the works reviewed, a new method of applying the Hg will be developed. To assure that there is a significant amount of mercury available at the crack tip, an environmental chamber will be manufactured and implemented to house liquid metals. By completely immersing the specimen in mercury, the concurrent oxidation presented by Wheeler, Hoagland and Hirth (1989). can be eliminated, assuming that the mercury itself does not contain excessive amounts of oxygen. The purest, commercially available mercury will be used to ensure trace amounts of oxygen.

In addition to these tests, stress intensity factor based incubation tests will be conducted. The incubation test will consist of applying a specific SIF and holding it constant until failure occurs. These tests will be aimed to determine the effects of diffusion of Hg into the solid metal. As Wheeler, Hoagland and Hirth (1989) suggested that time could be a factor in the LME process, these incubation periods will be used to determine how much of an effect time has on LME. As before, these experiments will be conducted in different environments.

After the mechanical testing has been completed, metallurgical analyses will be conducted, including optical and scanning electron microscopy. Observing the fracture surfaces will reveal vital information towards the LME behavior of the Al-Hg couple. Information regarding fracture, either through intergranular, transgranular or a combination thereof, will provide supporting information in the confirmation, rejection or extension of current microstructural LME failure mechanisms.

## **CHAPTER 3**

### **EXPERIMENTAL METHOD**

As a part of this research, several experimental program sets were conducted. These experiments included tests involving static laboratory air, saltwater, and liquid mercury environments. All environments incorporated various loading patterns, e.g. standard fracture, fatigue pre-cracking and SIF incubation tests. Experiments were carried out in the Mechanical Properties Characterization Laboratory (MPCL) at the University of Central Florida (UCF). The metallurgical analysis was performed at the Materials Characterization Facility (MCF) located in Research Park at UCF.

#### **3.1 Mechanical Testing**

A variety of mechanical tests have been implemented in previous efforts to understand underlying mechanisms LME, which incorporated various specimen types. Tensile and delayed failure tests on smooth steel specimens were used in the study of LME by Gordon and An (1982). Later, double cantilever beam (DCB) specimens were implemented by Wheeler et al. (1989) to study stress intensity thresholds,  $K_{th}$ , and crack propagation under LME conditions. Following this work, both smooth tensile and fracture specimens were analyzed by Kane et al. (1993) in an effort to validate slow strain rate (SSR) routines. Each of these works involved various levels of sophistication; each with respective problems during experimentation.

One trend common in all of the previously mentioned works involved the proper wetting of the crack tip with a liquid metal. Achieving LME conditions implies that there is a constant supply of equally-pure liquid metal at the crack tip; however, these studies were only able to wet the surface of the specimen through an acid cleaning process. This method guarantees a supply of liquid at the surface, but there is no mention of how well the liquid metal wets the newly

fractured surfaces<sup>1</sup>. This causes concern, as oxidation could inhibit LME conditions by creating a “protective” coat over the surface. For LME to exist, the liquid metal must be in intimate contact with the newly formed crack tip. As this research involves a study of cracks and the resulting crack-tip propagation, it was decided that fracture methods would be best suited during the mechanical testing process.

### 3.2 Fracture Testing

Fracture testing is a technique that is capable of reporting a variety of useful data. Information regarding crack tip propagation, crack tip velocity,  $K_{Ic}$ ,  $K_{ILME}$ , and  $K_{th}$  can all be obtained via mechanical experiments on specimens that have a pre-existing crack. With few modifications and attachments, a universal load frame is capable of conducting such tests.

#### 3.2.1 MTS Test Frames

For this research, a MTS Electromechanical Insight 5 kN and Servohydraulic 100 kN load frame were utilized, as shown in Fig 3.1. Both frames are able to conduct a variety of tests



**Figure 3.1:** MTS Insight 5 (left) and Servohydraulic (right) load frames.

<sup>1</sup>Key authors who performed the research are deceased or would not respond to several attempts at contact.

---

**Table 3.1 – MTS Load Frame Specifications**

---

<b>Insight 5 kN</b>	
<b>Column Configuration</b>	Single
<b>Force Capacity</b>	5 kN (1.125 kip)
<b>Maximum Displacement Rate</b>	500 mm/min (20 in/min)
<b>Servohydraulic 100 kN</b>	
<b>Column Configuration</b>	Single
<b>Force Capacity</b>	100 kN (22.5 kip)
<b>Maximum Cycle Frequency</b>	100 Hz

---

including tensile, compressive, peel/tear, fatigue, fracture experiments on specimen-sized samples, with each having strengths in different experimental setups.

### 3.2.2 Capabilities and Limits

The capabilities of the mechanical load frames were nearly limitless, allowing for several routines to be implemented based upon the capabilities of each frame. Selected specifications are detailed in Table 3.1. In addition to the load frames, the software for each frame allowed for the addition of external measuring devices to be attached and recognized. Several input channels were available to properly outfit the frame for fracture testing; primarily the addition of a crack tip opening displacement (CTOD) gage.

The Insight load frame utilized universal couplers with through pins while the servohydraulic frame utilized hydraulic grips. Each method of gripping specimens permitted the use of a wide variety of clamps, holders and stages necessary to accommodate various mechanical tests. As in the case of the environmental bath that was designed, further described in section 3.5, any addition can be secured into the frames with minimal effort.

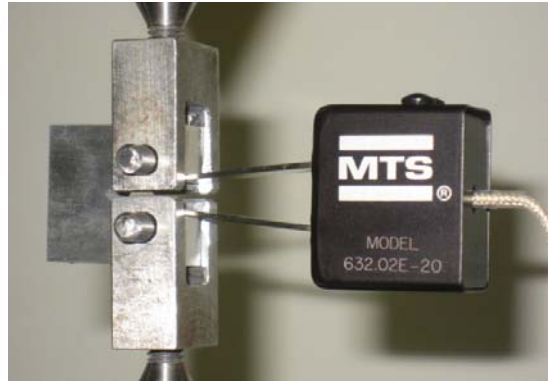


*Figure 3.2: MTS Clip-On Gage used in measuring the crack tip opening displacement of a C(T) specimen with knife edges.*

### 3.2.3 Crack Tip Opening Displacement Gage

Crack tip opening displacement (CTOD) gages make it possible to measure the displacement at the crack tip without any knowledge of the crosshead position. Specially designed specimens that incorporate knife edges can utilize these gages during the testing. Commonly referred to as clip gages, the double cantilever beam design allows for accurate measurement of the crack tip displacement, as shown in Fig. 3.2.

The CTOD gage that was used during these experiments was a MTS Clip-On gage, model 632.02E-20. Specifications on this gage are detailed in Table 3.2. A main advantage to using a CTOD gage is that crack tip displacement is not directly measured via displacement of the crosshead. As larger forces are applied, additional displacements from the through pins and frame hardware contribute to the overall crosshead displacement. Even though the stiffness on the hardware is extremely high, these small deflections (on the order of ten-thousandths of an inch) will contribute to less-accurate crack tip displacement measurements. When using a clip gage, the only displacement that is directly measured is the opening of the knife edge, resulting in the most accurate measurement possible. These knife edge displacements can be correlated with crack length. A model between crack length and cross-head displacement will be discussed in a later chapter.

---

**Table 3.2 – MTS Clip-On Gage – 632.02E-20**

---

<b>Gage Length</b>	5.08 mm (0.2 in)
<b>Travel</b>	+2.54/-12.7 mm (+0.1/-0.5 in)
<b>Non-Linearity</b>	0.15%
<b>Max Frequency</b>	50 Hz
<b>Compressed Force</b>	2500 g (5.5 lbs)
<b>Temperature Range</b>	-101°/148° C (-150°/300° F)
<b>Resolution</b>	0.0025 mm (0.0001 in)

---

All measurements made regarding the CTOD were outlined in ASTM E1290, the standard test method for Crack-Tip Opening Displacement Fracture Toughness Measurement.

Additionally, the clip gage is designed specifically to meet the ASTM Standard E399, the standard test method for Plane-Strain Fracture Toughness of Metallic Materials. Following the standards ensured accurate measurements and repeatability between specimens. Additional information regarding the specimen is detailed in Section 3.4.

#### 3.2.4 Pre-cracking Specimens

Conducting fracture experiments requires the use of fracture mechanics test specimens. An additional requirement is that the specimens are pre-cracked through mechanical cycling. Machined notches ( $K_t \approx 12.5$ ) help to define where the crack will emanate from; however, mechanical pre-cracking is necessary to generate a sharp crack tip.

As with most mechanical processes, fatigue pre-crack generation is a detailed process and a distinct routine must be followed. For these experiments, fatigue pre-cracks were generated in accordance with ASTM E647 (2000), the standard test method for measurement of fatigue crack growth rates. Pre-cracks were achieved by loading specimens with a displacement-controlled test routine through approximately 3000 cycles. The load ratio,  $R$ , implemented was 0.1, which is a ratio between the minimum load,  $P_{min}$ , and the maximum load,  $P_{max}$ . In compliance with

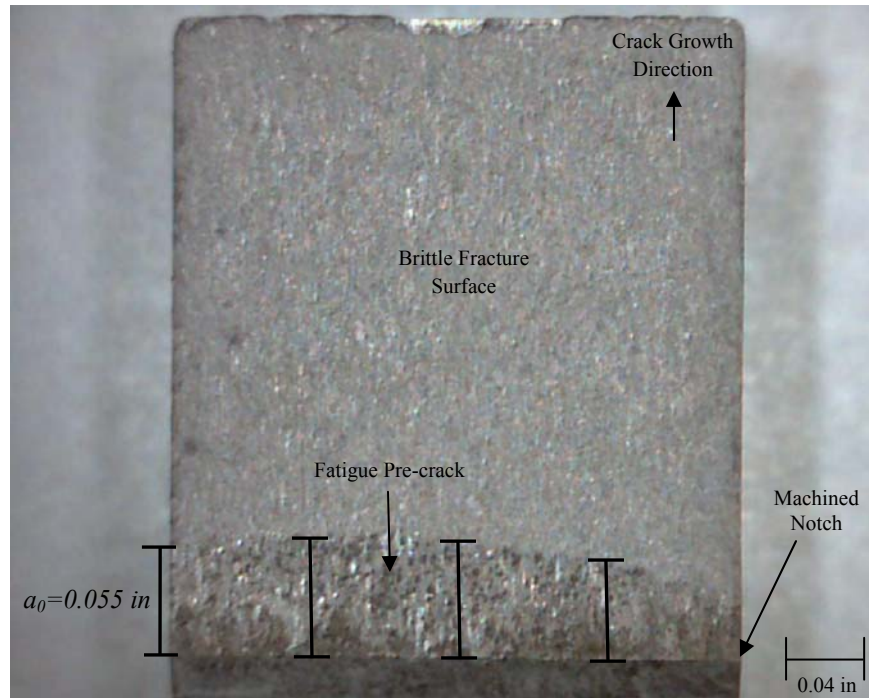


**Figure 3.3:** Top-down view of a fracture specimen (S-L-13) displaying the location of the pre-crack measurements.

E647, the loads used were  $P_{min} = 50 \text{ lbf}$  and  $P_{max} = 500 \text{ lbf}$ , with a crosshead velocity of  $0.4 \text{ in/min}$ . The resulting plastic zone near the notch is approximately  $0.005 \text{ in}$  ( $0.127 \text{ mm}$ ).

Pre-cracks were measured in accordance with ASTM E399. Once the fracture specimen had completely failed, measurements were made at three key locations: in the center of the specimen and midway between the center of the specimen and each surface. A failed specimen with the perspective from above the fracture surface is shown in Fig. 3.3. An average of these three values was used to determine the final pre-crack length which subsequently was used in calculating  $K_{Ic}$ , referred to as  $a_o$ . Resulting crack lengths are outside of the plastic zone near the notch tip.

### 3.3 Material Selection

The material used in this work was cold-rolled Al 7075-T651. This particular aluminum alloy is commonly used in high stress applications, notably in the aerospace industry. With the weight-to-strength benefits, this material is suitable for a variety of designs.

### 3.3.1 Al7075 – T651

The chemical composition of Al 7075-T651 is provided in Table 3.3, followed by the mechanical properties in Table 3.4 and 3.5. Annealing is done at 413° C (775° F) while artificial aging is used to strengthen this material, at a temperature of 121° C (250° F). A slab of the cold-rolled Al 7075-T651, along with the grain orientation, is shown in Fig 3.4.

<b>Al</b>	87.1 - 91.4	<b>Mg</b>	2.1 - 2.9	<b>Zn</b>	5.1 - 6.1
<b>Cr</b>	0.18 - 0.28	<b>Mn</b>	Max 0.3	<b>Ti</b>	Max 0.2
<b>Cu</b>	1.2 - 2	<b>Si</b>	Max 0.4	<b>Fe</b>	Max 0.5

<b>Orientation</b>	<b>S-L</b>	<b>T-L</b>	<b>L-T</b>
<b>Yield Strength, <math>\sigma_y</math> [MPa (ksi)]</b>	430 (62.5)	489 (70.9)	498 (72.3)
<b>Ultimate Strength, <math>\sigma_{uts}</math> [MPa (ksi)]</b>	462 (67.1)	540 (78.3)	563 (81.7)
<b>Rupture Strain, <math>\epsilon_f</math> [%]</b>	1.32	4.80	6.27

<b>Orientation</b>	<b>S-L</b>	<b>T-L</b>	<b>L-T</b>
<b>Fracture Toughness, <math>K_I</math> [MPa-m<sup>1/2</sup> (ksi-in<sup>1/2</sup>)]</b>	17.6 (16.0)	24.2 (22.0)	28.6 (26.0)

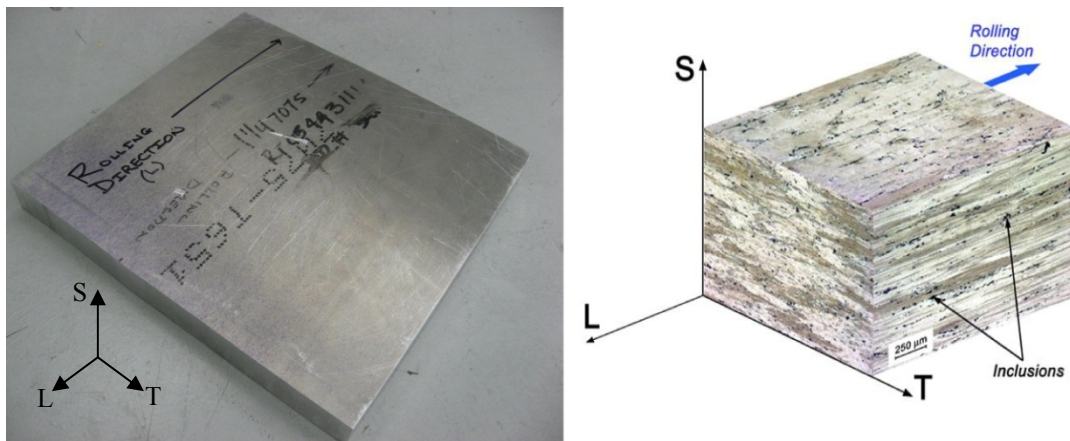


**Figure 3.4:** Cold-rolled sheet of Al 7075 – T651 used in the fracture experiments (left) with associated grain orientation (right).

The cold-rolled slab used represented commercially available product, ensuring that the fracture tests were indicative and applicable to material in service. Overall dimensions of the slab were 13 in (L) x 12.25 in (T) x 1.25 in (S). For this particular aging, grain sizes are approximately 0.0236 in (L) x 0.0059 in (T) x 0.0016 in (S) (Petit and Zeghloul, 1990). All of the fracture specimens were machined from this one slab, which allows for the assumption that all of the grain sizes were approximately identical. Additionally, the gradient in grain size and material properties in the T-direction is minimal. With the given dimensions of the slab, approximately 120 S-L C(T) oriented specimens could be produced. Dimensions, along with the orientation, of the specimen will be discussed in more detail in Section 3.4.2.

### 3.3.2 Mercury

Liquid mercury (Hg) was used as the embrittler through the course of these experiments. The mercury that was obtained was reported to be 99.99% pure at the time of purchase. As the experiments continued, it was noted that the Hg was not as pure as it was initially and additional mercury had to be purchased. The purity of the mercury will be further discussed in Section 3.7.3.



*Figure 3.5: Safety equipment in use during experimental setup.*

As Hg is a highly toxic substance, careful consideration was taken during the handling of the liquid substance. Lab coats, gloves, eye protection and mercury filtration masks were used during all experiments, as shown in Fig. 3.5. Upon completion of a test, nearly all (above 99%) of the mercury used can be recaptured and used in subsequent tests. Frequent inspections from the Environmental Health and Safety department at UCF ensured the safety throughout the entire test process.

### 3.4 Fracture Specimen Preparation

Specific requirements regarding the size, dimension and surface conditions for the fracture specimens had to be closely adhered to. Fracture specimen dimensions were vital in calculating the plane-strain fracture toughness,  $K_{Ic}$ , which can be considered a material property if all of the dimensions are correct. With a few key driving dimensions regarding specimen width,  $W$ , and pre-crack length,  $a$ , the remaining dimensions were calculated. Information regarding specimen design was contained in ASTM E399.

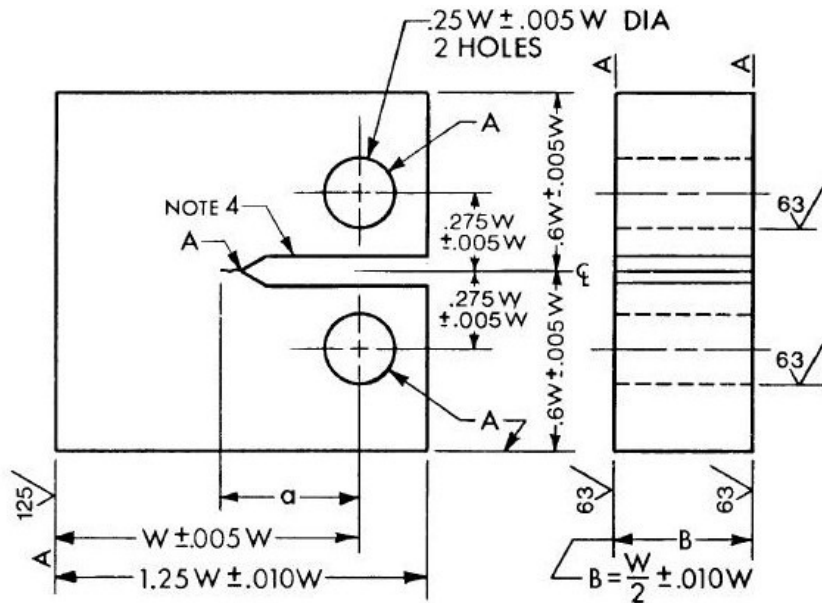


**Figure 3.6:** Specimen dimension requirements for C(T) specimen used in plane-strain fracture toughness testing, as per ASTM E399.

### 3.4.1 ASTM E399

The standard test method for plane-strain fracture toughness, ASTM E399, details the proper technique when testing metallic materials. Additionally, the requirements for specimens are fully detailed in Annex A.4 for Compact Tension, C(T), specimens, as shown in Fig. 3.6. Not only did the specimen require special design consideration, but special clevis adapters had to be machined. The clevis dimensions were dependent upon the choice of  $W$ , as shown in Fig. 3.7. All of the dimensions were driven by the choice of  $W$ , which resulted in a custom apparatus designed specifically for the C(T) specimens used during this experiment. In order to calculate a valid value of  $K_{Ic}$ , certain criteria had to be met. Particularly, two main equations had to be satisfied, both of which are dependent upon specimen dimensions and material properties, i.e.

$$a, B, W - a > 2.5 \cdot \left( \frac{K_{Ic}}{\sigma_y} \right)^2 \quad (3.1a)$$

$$0.45 < \frac{a}{W} < 0.55 \quad (3.1b)$$

Here,  $a$  is the crack length,  $B$  is the thickness of the specimen and  $W$  is the driving dimension described previously.

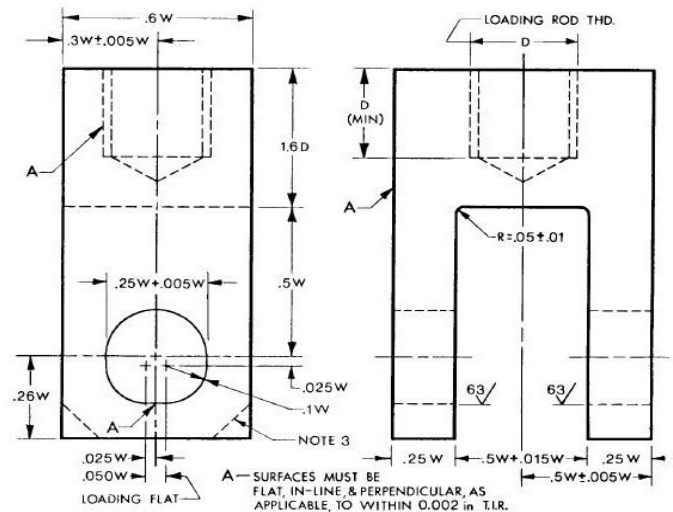


**Figure 3.7:** Clevis dimension requirements used in plane-strain fracture toughness testing of C(T) specimens, as per ASTM E399.

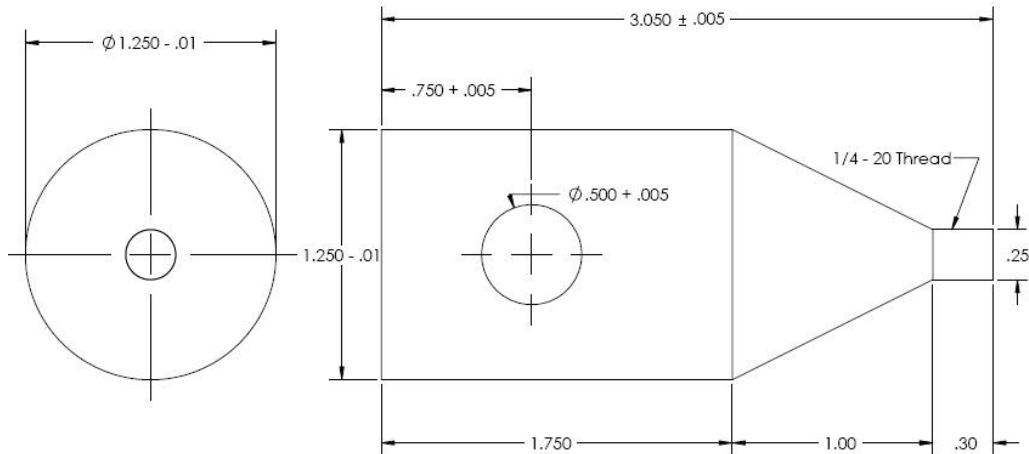


**Figure 3.8:** Adapter designed to attach the clevis to the MTS load frame during fracture testing. All units are in inches.

Utilizing the clevis and specimen required the design of another component to properly attach the clevis to the MTS frame. The clevis required a threaded connection used in fastening it to the load pin adapter. Unfortunately, the load frame only accommodated a universal adapter, which was much larger than the tensile specimen being implemented. A basic adapter was designed and machined to allow the attachment of the clevis, Fig. 3.8. Both the adapter and clevis were made of a hardened steel, AISI 1018 ( $E = 29.7\text{Msi}$ ), in order to maintain a high stiffness; implying that the crosshead displacement was only a result of the deflection within the specimen. With these additional attachments, the fracture specimen could be properly secured within the load frame.

### 3.4.2 Dimensions and Orientation

The overall goal during the experimentation was to limit the amount of liquid mercury utilized. A smaller specimen would result in a smaller volume of liquid Hg required during testing. In accordance with ASTM E399.A.4, the specimen was designed with the width dimension  $W = 0.75$  in (19.05 mm). This value depicted all of the remaining dimensions, including the machined crack. It was projected that these dimensions would satisfy Eq. 3.1a.

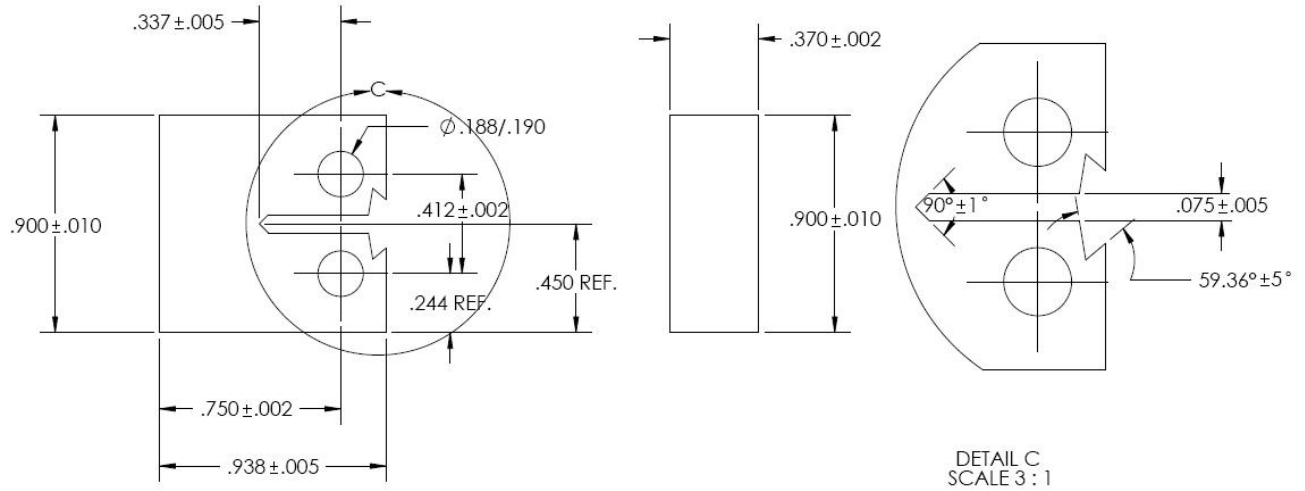


**Figure 3.9:** *C(T)* specimen dimensions used in the fracture toughness testing. All units are in inches.

Specimens were additionally designed with knife edges to accommodate the CTOD gage used during testing, as shown in Fig. 3.9.

Another key distinction in the specimens utilized is the orientation in regards to the rolling direction of the slab. The chosen orientation was that of the S-L direction (Fig. 3.10). The first letter in the orientation denotes the direction perpendicular to the crack while the second indicates the direction of expected crack growth. A unique property of the S-L direction is that the crack grows in the longitudinal direction, with has a uniform microstructure at the

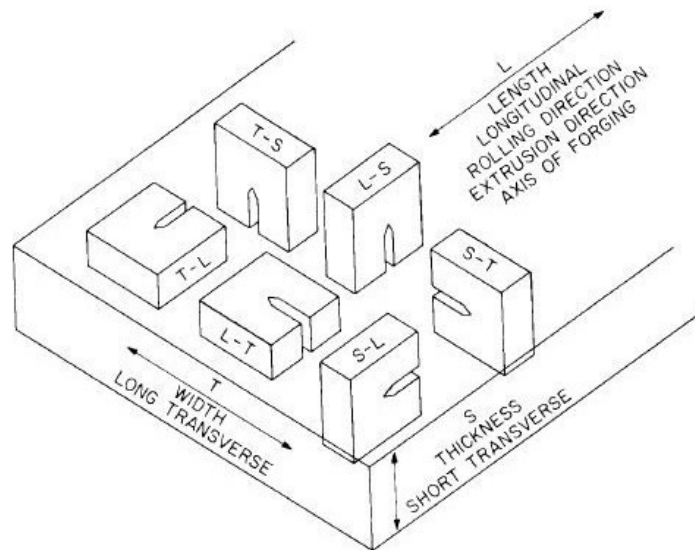


**Figure 3.10:** Crack plane orientation code for Rectangular Sections, as per ASTM E399.

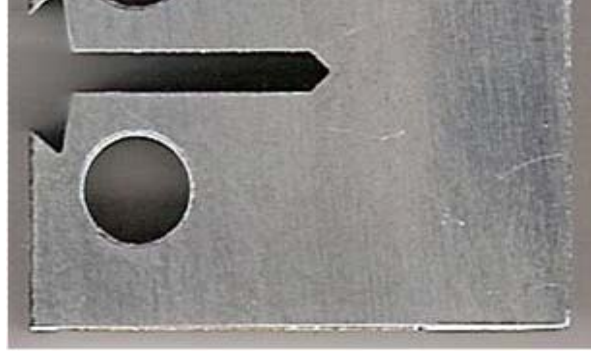
crack tip. Additionally, this direction has the maximum grain flow of grain boundaries (ASTM E399). With a uniform microstructure, the crack is able to grow in a fashion that favors grain boundary dislocation and maximum diffusion of the liquid embrittler is expected.

Fracture data is more readily available for T-L and L-T orientations, as these orientations provide the highest mechanical strength, as shown in previously in Table 3.4. Additionally, fixturing during machining is easiest with the sheet flat on a CNC table, lending to components being machined with these directions. Naturally, the grain boundaries are different along the T-S plane, as cold working crushes boundaries at the surfaces. With the grain boundary a function of depth, when using T-L or L-T orientations, cracks can propagate in a direction that is unfavorable during testing. This is the inherent advantage of S-L specimens, as the grain boundaries will be uniform throughout the projected crack path. Coupled with the limited amount of data for S-L orientations, this was the major motive for selecting this particular orientation.

### 3.4.3 Surface Condition

Crack propagation is not only dependent upon the grain boundary orientation, but also the surface condition of the specimen. Pits and tooling marks can significantly affect the crack propagation path, diverting the crack tip propagation from its natural course. As the natural path of the crack was desired, specific machining requirements, followed by a polishing process was followed.

Initial specimens were obtained from Metcut Research, Inc. (Cincinnati, OH, USA), a leader in specimen preparation and mechanical testing. Surface roughness is a measurement of the average of absolute peaks and valleys on the surface of a specimen, i.e.,



(3.2)

*Figure 3.11: Fracture specimen surface as obtained after machining, with a surface roughness of  $<64Ra$ .*

where  $n$  is the number of measurements and  $z$  is the height of a measurement relative a selected zero plane on the surface of the specimen. Specimens were obtained with a surface roughness of 64 Ra or less. The surfaces on the specimen were free of any defect and displayed no tooling marks, as shown in Fig. 3.11. Even with the relative smoothness of the surface, a further polishing process was administered.

Subsequent specimens were obtained from a local machine shop, with the same tolerances as those from Metcut. Trial specimens were first machined out of Al 6061 sheet in the T-L direction to verify that specimen tolerances could be achieved. After approval of the dimensions, all orders for new test specimens were placed at the local shop. Similar methods, e.g. wire EDM, were used in the preparation, resulting in identical samples from the two suppliers.

Specimen polishing was a five step process that involved wet sanding and micron polishing powder. The surface preparation procedure for each surface involved:

1. Wet sand with 240 grit paper for 1 minute.
2. Rotate specimen  $90^\circ$  and wet sand with 320 grit paper for 1 minute.
3. Rotate specimen  $90^\circ$  and wet sand with 400 grit paper for 1 minute.
4. Rotate specimen  $90^\circ$  and wet sand with 600 grit paper for 1 minute.
5. Wet polish with Alpha C 1  $\mu\text{m}$  alumina polishing mixture for 1 minute.



*Figure 3.12: Specimen surface after sanding and polishing with 1  $\mu\text{m}$  alumina powder.*

The resulting finish on the surface was mirror-like with no visible imperfections, as shown in Fig. 3.12. The finish on the sample ensured that the crack was free to propagate without any influence from surface marks.

### **3.5 Environmental Bath**

Liquid Metal Embrittlement testing required that a sufficient amount of the liquid embrittler was available at the crack tip. If there was not enough Hg at the crack tip, oxidation could occur on the newly formed surface and halt LME conditions. Previous researchers, Gordon and An (1982) and Wheeler et al. (1989), only “wetted” the surface with a few drops of liquid metal. With this method, it was unclear if the entire crack surface was subjected to LME conditions or not. Initial tests suggested that the entire crack might not have been in constant contact with the liquid embrittler through this method. In an effort to eliminate this uncertainty, an environmental bath was developed capable of immersing the machined notch and the projected path for crack propagation.

#### **3.5.1 Design**

The environmental bath was designed with the goal of reducing the amount of liquid Hg that was needed for each test. The bath had to be properly affixed to the load frame and was not

to interfere with any safety equipment incorporated into the frame. Additionally, no load was to be imposed on the bath during testing. The chamber needed to house the specimen, along with all of the associated adapting hardware. Most importantly, this chamber had to be sealed off so that no liquid would escape during testing.

A two-piece design was proposed that mounted securely to the surface of the clevis adapter shown in Fig. 3.8. A cutaway model of this is shown in Fig. 3.13. Here, a cutaway of the experimental setup is shown assembled in the CAD software. The chamber included a top, which was to prevent any liquid mercury from possibly escaping if there was any splashing during the tests. As seen, each piece was specifically designed to work with the others, which ensured that a tight seal was achieved and that all of the mercury could be recovered.

Initially, grooves were machined into the base of the top and bottom pieces. Two silicone o-rings were to be placed within these grooves, providing a tight seal for the bottom half. After careful consideration, the location of the o-rings was moved to a position between the clevis and the bottom chamber. The compression fit that resulted from securing the clevis to the

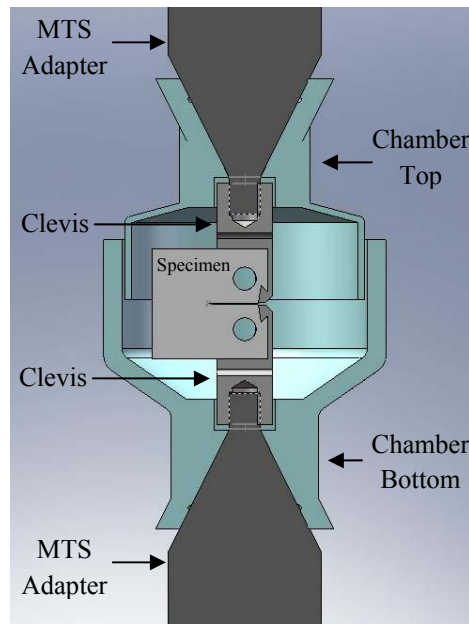


*Figure 3.13: Cutaway view of the assembled fracture chamber with specimen.*

adapter provided a much more suitable location for the o-rings. As a result, a more desirable seal was achieved with even more stability of the mating parts.

### 3.5.2 Manufacturing

The manufacturing of the environmental bath involved submitting the 3-D CAD model to a review conducted by First Cut Prototype (Maple Plain, MN, USA). During this process, a suggestion was made to eliminate excessive machining and cost by leaving the base of the bottom and top un-notched. Aside from this minor suggestion, no other changes were needed and the model was ready for manufacturing.

To allow for observations to be made during testing, a translucent polycarbonate was used as the working material, as it is not reactive with liquid mercury. The main reason was to observe the fluid level within the chamber and to know whether or not the crack tip was fully submerged in the fluid. Upon receiving the prototypes, the level of clarity was not as expected; however, a reasonable estimate could be made as to whether or not the crack tip was completely below the liquid level. A cutaway view of the fully assembled chamber loaded into the load frame is shown in Fig. 3.14. Additional information regarding a new chamber design will be presented in later chapters.

### 3.5.3 Assembly/Disassembly

To assemble, the fracture specimen is secured in the top and bottom clevis. The bottom MTS adapter is then fitted with the bottom chamber and the bottom clevis is fastened onto the adapter, seating the o-rings in the process. With the bottom assembled, the mercury is then poured carefully to the fluid level line. The top of the chamber is then attached with the top MTS adapter. Finally, the bottom MTS adapter is secured into the load frame and the crosshead is lowered, completing the assembly process.

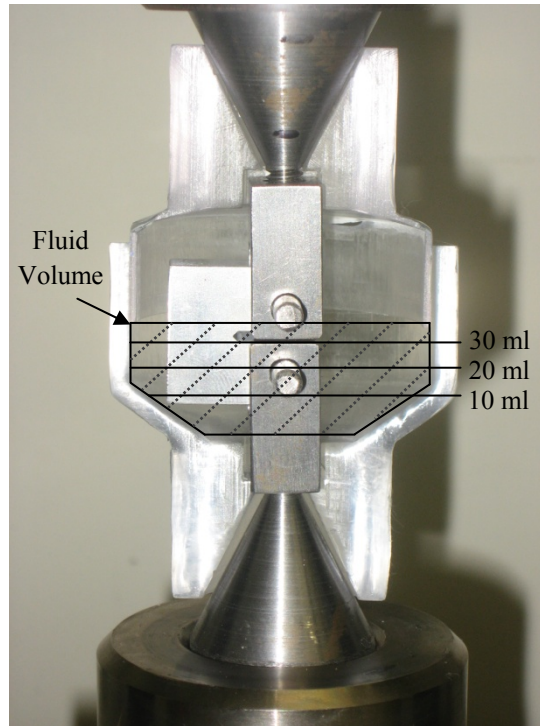


*Figure 3.14: Cutaway view of the assembled fracture chamber with specimen secured in load frame.*

Upon fracture, the crosshead is raised to provide clearance for removing the bottom MTS adapter. Removal of the upper MTS adapter precedes removal of the lower, allowing for any mercury collected on the upper half of the specimen to be contained in the cup. The lower half is then removed with the mercury, which is then poured back into its sealed container. The specimens are removed from the clevis and placed into sealed bags for safe handling. All adapters and mercury containers were stored in air-tight containers, which ensured that all elements exposed to mercury were contained and stored safely.

### **3.6 Routines and Methods**

Prior to the incubation testing conducted in liquid Hg, several validation cases were run. These routines involved testing samples in air and in saltwater before any mercury was used. With all types of mechanical testing, trial runs are used to eliminate any flaws and understand how the software will control the hardware and the impact on the sample. Care was taken to

fully understand how the software implemented routines and what safety features were embedded within to prevent damage to specimens by the load frame.

### 3.6.1 Lab Air Testing

Several different routines were developed particularly for the testing of fracture specimens. Utilizing MTS software, TestWorks 4, different displacement- and load-controlled routines were used to achieve the desired results. Particularly, the main test routines involved fatigue pre-cracking (load-controlled), constant load (load-controlled) and tensile fracture (displacement-controlled) regimes. Each program required several different inputs, including crosshead displacement rates, minimum and maximum extensions and several safety checks. An additional routine, constant stress intensity factor (load- and displacement-controlled) will be discussed in more detail in Chapter 7.

Dummy specimens were machined by Metalmaster Manufacturing, Inc. (Orlando, FL, USA) and were employed during all validation tests (Fig. 3.15). Low-cost alternatives to the precision specimens, these samples allowed for the three routines to be calibrated. The dummy specimens allowed for an understanding of the software/hardware interaction, how different inputs affected test performance and for fine-tuning of the methods. Approximately five dummy specimens were used, including an additional ten dummy specimens that were used as demonstration specimens for fracture experiments in material laboratories.



**Figure 3.15:** *Inexpensive dummy specimen used in validation testing.*

In addition to the dummy specimens, precision specimens were used in establishing the  $K_{Ic}$  of Al 7075-T651. These values were recorded in the form of Load-Displacement ( $P-\delta$ ) curves. Maximum loads from each test were utilized in the calculation of  $K_{Ic}$ , as defined by ASTM E399. Results were saved for later comparison with those obtained from tests conducted in Hg.

### 3.6.2 Saltwater Testing

Saltwater was used as the working fluid during testing of the environmental bath. As LME is a branch of SCC, saltwater was chosen as higher strength aluminum alloys have shown susceptibility of SCC. A widely publicized event involving SCC of aluminum was the failure of Aloha Airlines Flight 243, as previously discussed. A salt-rich environment was to blame, in addition to repeated loading and unloading of the cabin, which resulted in crack propagation and eventually catastrophic failure. With the known susceptibility of Al 7075-T651 to SCC, the main purpose of testing in saltwater was to verify the mechanical testing technique. Once results were obtained that agreed with existing Al-SCC data, the technique was considered finalized.

The environmental bath testing began with soaking routines in saltwater, according to ASTM G44 and G47, standard test methods for Exposure of Metals and Alloys by Alternate Immersion in Neutral 3.5% Sodium Chloride Solution and Determining Susceptibility to Stress-

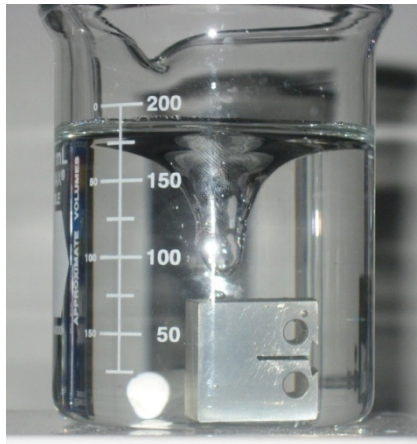


*Figure 3.16: Specimen subjected to pre-soaking routine.*

Corrosion Cracking of 2XXX and 7XXX Aluminum Alloy Products, respectively. Saltwater was mixed and stirred in room temperature using a Fisher Scientific Isotemp Stirring Hot Plate (Fig. 3.16). Upon completion of the pre-soaking routines, specimens were removed and allowed to dry overnight.

With a dry specimen, the environmental chamber was assembled on the load frame adapter and the clevis was fastened. Graduated cylinders were then used to measure the amount of fluid that would adequately submerge the crack tip. This volume would later be used in determining the proper amount of mercury used in filling the bath. Once an acceptable fluid level had been achieved, the top adapter was fastened into the setup and the crosshead was lowered into position. With the upper adapter secured in place in the load frame, Fig. 3.17, validation of the methods with the environmental chamber began.

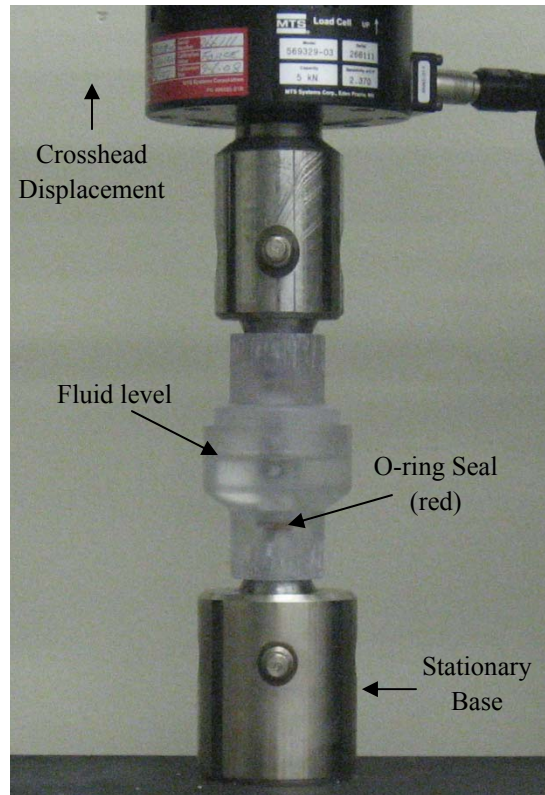


*Figure 3.17: Environmental chamber secured in load frame during saltwater testing.*

All of the experimental routines that were described previously were again tested. Every aspect of each routine was tested, including crosshead displacements, absolute positioning and o-ring seals. Utmost care was taken during this process to ensure that the same method could be used while handling the mercury during testing. After all of the routines were verified to work correctly, the specimen was fractured, the assembly was broken down and the fluid level was re-measured. After nearly all of the fluid (>99%) was recaptured in a beaker, without any spills, tests in mercury were able to be performed.

### 3.6.3 Mercury Testing

The amount of time spent conducting trial experiments previously mentioned significantly reduced the “guess work” involved with tests involving mercury. The method of



**Figure 3.18:** Pre-soaking of specimen in Hg prior to pre-cracking routines.

pouring mercury into the cup was the only human factor and was conducted very slowly within containers (Fig. 3.5); in the event of a spill, all mercury would be captured by the container.

Implementing the outlined procedures, fatigue pre-cracking, constant load/incubation and tensile fracture programs were conducted with the specimen immersed in liquid Hg. A variety of methods were employed regarding the pre-soaking of specimens. Some routines involved soaking a specimen in Hg prior to pre-cracking or allowing the pre-cracked specimen to remain submerged prior to incubating or fracturing and combinations thereof. An example of pre-soaking in liquid Hg is shown (Fig. 3.18) demonstrating the process used to expose specimens to a corrosive material. Weights were used to keep the crack tip under the fluid level, as aluminum is less dense than mercury,  $2.8 \text{ g/cm}^3$  to  $13.54 \text{ g/cm}^3$ , respectively.

Establishing the  $K_{ILMEC}$ , critical stress intensity factor under LME conditions, in mercury was the first objective. It was imperative that these results confirmed that LME conditions were present through a decrease in the critical stress intensity factor. Several routines involving pre-cracking and fracturing in Hg were conducted facilitating a comparison of the statistical averages

of  $K_{Ic}$  for tests conducted in air and liquid Hg. With confirmation that LME conditions existed, further methods were explored.

Incubation experiments were implemented in an effort to reveal that the phenomena of LME is both load- and time-dependent. This test routine was implemented after the pre-cracking of specimens had finished and any additional soak period had been completed. Using the values of  $K_{ILMEc}$  obtained during fracture tests, loads were applied in the incubation routine that would result in a predicted stress intensity factor. Specifically, the goal was to achieve loads that would result in decreasing values of  $K_{ILME}$ , specifically 95%, 90%, 85%, etc. of  $K_{ILMEc}$ . The time-to-failure for each of these experiments and the crack growth history determined from crosshead displacement provided key data regarding the time dependency that the stress intensity factor has on LME.

### 3.7 Modifications

Throughout the course of the mechanical testing, several modifications had to be made. Modifications made were entirely limited to the specimen and its design and the liquid mercury; the test method and routines implemented were deemed sufficient from their inception. The modifications made included slightly altering the specimen around the knife edges, coatings used

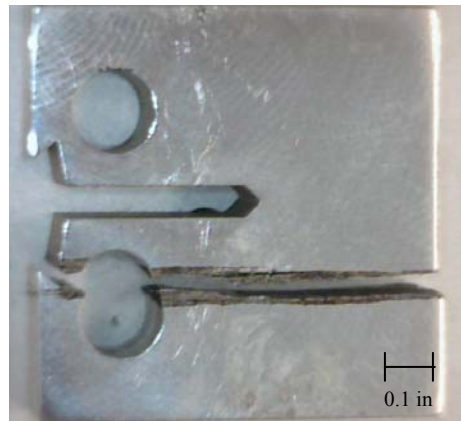


**Figure 3.19:** Failed specimen where crack propagated through knifed-edge.

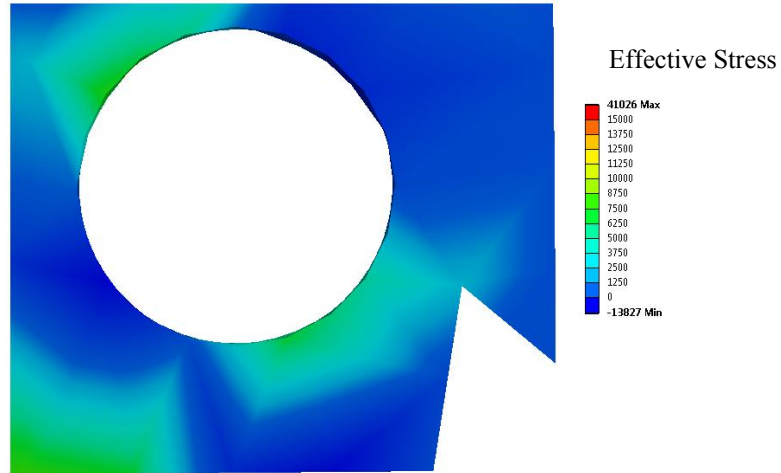


**Figure 3.20:** Close-up image of knifed-edge revealing an increase in stresses.

to protect key features and implementing new mercury. Each modification provided a more accurate test method, ultimately increasing the accuracy results.

### 3.7.1 Knife Edge Specimen Design

An unexpected error that occurred during tests in liquid mercury involved samples failing at locations near the knife edges, Fig. 3.19. The stress concentration at this location was initially disregarded, as it was believed that there was not a significant amount of stress present. After conducting a static finite element analysis, it was concluded that there was enough stress at this

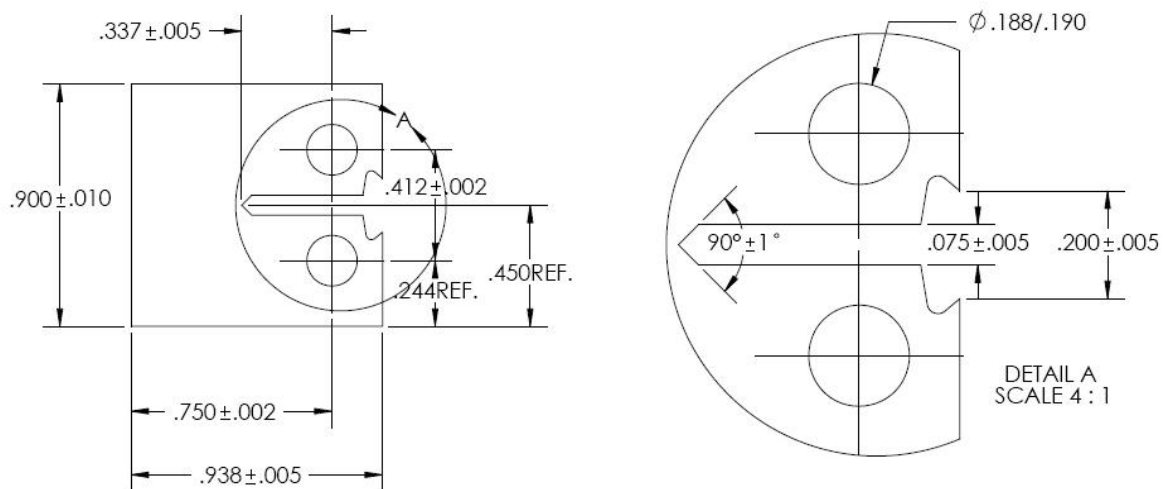


**Figure 3.21:** Modified specimen with rounded valley in knifed-edge.

location to serve as competition for crack initiation and propagation, Fig 3.20. More detail with regard to the finite element modeling will be discussed in Chapter 5.

After close inspection, it was decided that the specimen be redesigned at the knife edges. Specifically, the inner valley of the knife edge was to be rounded, thus reducing the stress concentration, Fig. 3.21. By rounding out the valley, the load, coupled with the attack presented by the Al-Hg couple, would not be significant enough to cause an undesired failure. Although it was perceived that this task would help reduce the occurrence of undesired failures, unexpected failures continued to occur.

### 3.7.2 Synthetic Rubberized Coatings

Further investigation through FEA revealed that although the stress concentration at the knife edge had been addressed, there existed an increase in stress around the load pin hole, as shown in Fig. 3.22. Failures continued to occur at any location throughout the load pin hole (Fig. 3.23). Methods of coating the specimen with PlastiDip synthetic rubber were proposed, in an effort to protect aluminum that was not in the vicinity of the crack tip. The rubberized coating was chosen for use, as the finish is impervious to corrosion, providing the necessary protection without adding any additional stiffness to the specimen.

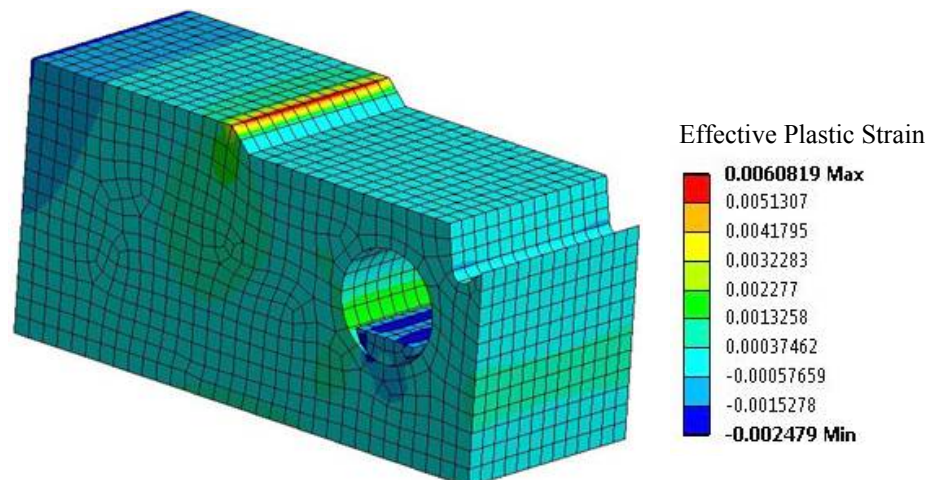


*Figure 3.22: FEA results from static analysis around pin hole.*



**Figure 3.23:** Failure of specimen through load pin hole.

### 3.7.2.1 Dipped

Utilizing a dipped method, PlastiDip was applied to the lower half of the C(T) specimen through a series of dips (Fig. 3.24). The result was a protective surface that shielded the base material from any attack by liquid mercury. After the drying period, the coating thickness was measured to be 0.025 in (0.635 mm). Due to constraints imposed by the clevis mouth opening, this fix resulted in a specimen thickness that was too large.

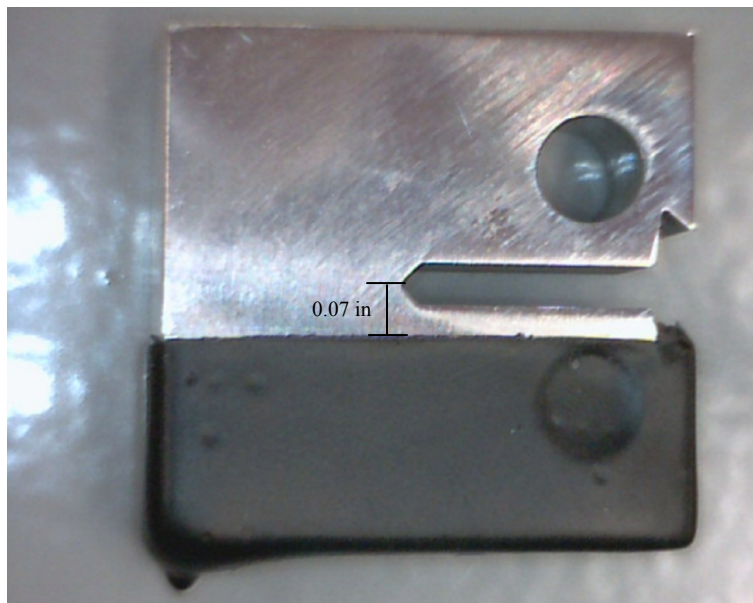


**Figure 3.24:** Specimen dipped in PlastiDip, covering load pin hole.

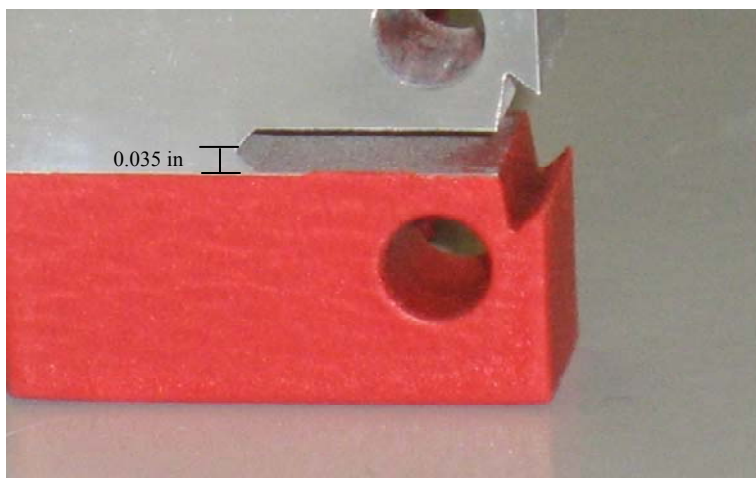


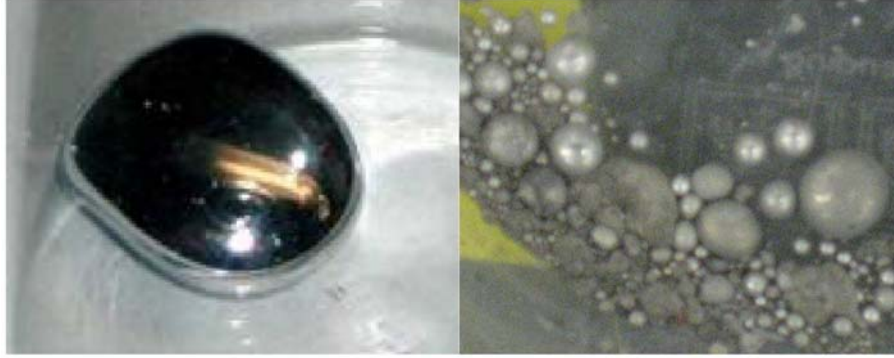
*Figure 3.25: Specimen sprayed with PlastiDip, within clevis tolerance.*

### 3.7.2.2 Sprayed

In an effort to reduce coat thickness, PlastiDip spray was utilized. Three coats were applied to the specimen, fully covering the lower half of the sample (Fig. 3.25). Painters tape was used to cover the tip, which prevented the coating from covering the projected crack path. Specimen surfaces were subsequently cleaned to remove any residue from the tape. Additionally, the coats were applied within the load pin hole, providing complete coverage of all aluminum from Hg attack. After the drying period, the coating thickness was measured to be 0.005 in (0.127 mm). With this thickness, the existing clevises could be utilized, allowing for no additional modifications to be made.

### 3.7.3 Pure Mercury

Additional mercury was purchased during the experimental process, as it was determined the existing mercury was too contaminated. Initial testing with the high purity mercury resulted in accurate LME conditions. The mercury was uncontaminated through the first several trials; however, as testing continued, the level of purity decreased due to chemical reactions between the Al and Hg. A comparison between the two stages of the mercury, from commercially-obtained 99.99% pure Hg to contaminated Hg after approximately 10 samples, is presented in



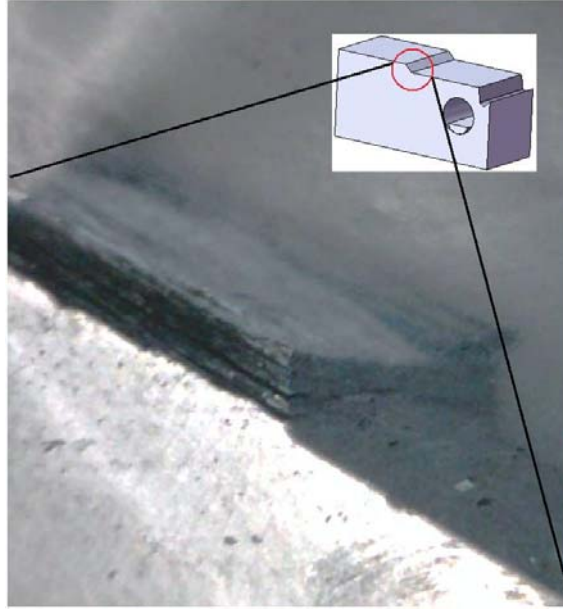
*Figure 3.26: Pure mercury (left) compared with Al contaminated mercury (right).*

Fig. 3.26. Pure Hg will tend to coalesce and form a pool, while the mercury contaminated with Al does not coalesce and remains in individual beads.

With the contaminated mercury, it was suspected that both oxidation and Al contamination prevented LME conditions from occurring, as seen by the discoloration. Wheeler et al. (1989) proposed that concurrent oxidation at the crack tip prevented LME, stating that any oxide film over the surface would inhibit the mercury from attacking the host metal. Results from tests conducted in mercury became increasingly similar to tests conducted in air, providing evidence that mercury contamination inhibits LME. Subsequent tests were conducted in the new mercury, re-establishing LME conditions at the crack tip.

### **3.8 Metallurgical Analysis**

Vital to all failure analyses, visual inspection of the failed surfaces provides significant qualitative data not obtained via qualitative analyses. A variety of tools, from visual and digital photography to scanning electron microscopy (SEM) were utilized. Overall details were provided by digital photography while fine details, such as fatigue striations, were observed with the SEM. Optical analyses were conducted in the MPC Laboratory and the MCF at UCF.



**Figure 3.27:** Digital microscope image of several cracks emanating from notch.

### 3.8.1 Digital Photography

Digital photography was used to capture basic pictures of the experimental setup, specimens and their coatings. Failed surfaces were hard to image with this method, as lighting conditions are not optimal. Particularly, digital photography was used in the preparation of the images presented in this chapter. A broad picture of the fracture surface is obtained, but further information requires higher magnification.

### 3.8.2 Optical Microscopy

Optical microscopy furnished several, high-quality images of the fracture surface. Key information, such as the pre-crack length measurements, was obtained using optical microscopy. Utilizing a digital microscope, a Dino-Lite AM211, macroscopic details, e.g. cracks along machined notch, were observed. An example of the detail obtained is shown in Fig. 3.27, where cracks are observed in more detail than the naked eye can view.

### 3.8.3 Scanning Electron Microscopy

Scanning electron microscopy provided images on the scale of a few micrometers. Employing a Hitachi 3500N with an accelerating voltage of 20kV and various working distances and magnifications, specimens were observed side-by-side for comparison of hypo-atomic features. This form of microscopy, which uses an electron beam to produce images via backscattered electrons, provides useful images of identifying features, such as fatigue fractures, cleavage marks and ductile dimples. Coupled with the energy dispersive x-ray analysis (EDS or EDX) software incorporated into the SEM setup, specimen failures are able to be specified as LME or non-LME failures. Specimens were placed in a vacuum chamber under the electron beam. Using a backscattered detector, electrons that are reflected off the surface are collected and a signal is generated by the software. The signal creates an image of the surface being viewed, down to 300,000x magnification. An example of an image obtained from this analysis is shown in Fig. 3.28, which clearly shows the fatigue striations that resulted from the pre-cracking of the specimen.

To verify that mercury was present at the crack tip and at additional locations on the fracture surface, EDX software was used. The specimen is impacted with electrons which react with the electrons in the specimen. X-rays are released, as a result of their interaction. The intensity of these x-rays is analyzed by the computer software, which correspond to the material that is under observation. Depending upon the material present at the surface, several peaks will be created on a graph, which detail the material present, as shown in Fig. 3.29. With this information, LME conditions were verified over the entire fracture surface, allowing for the results to be interpreted and compared with existing LME results.

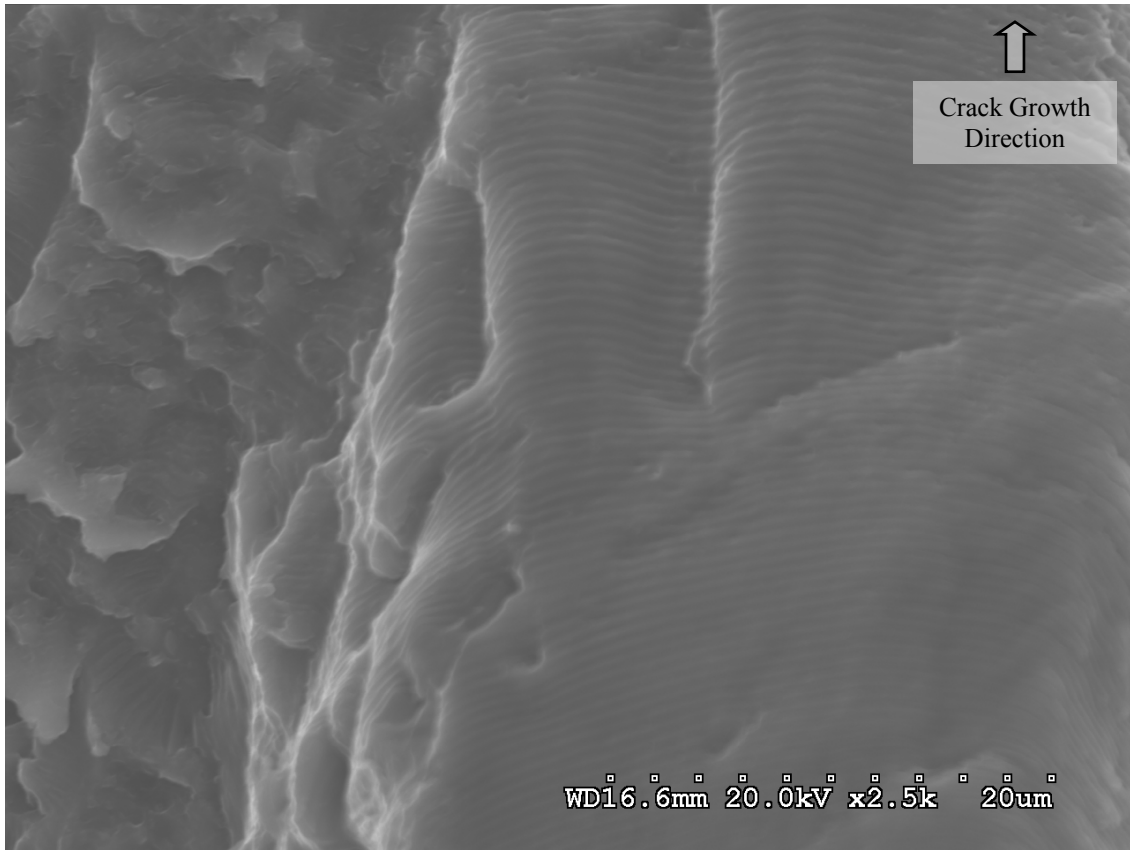


*Figure 3.28: Fatigue striations, shown at 2500x magnification, are a result of cyclic loading (S-L-23).*

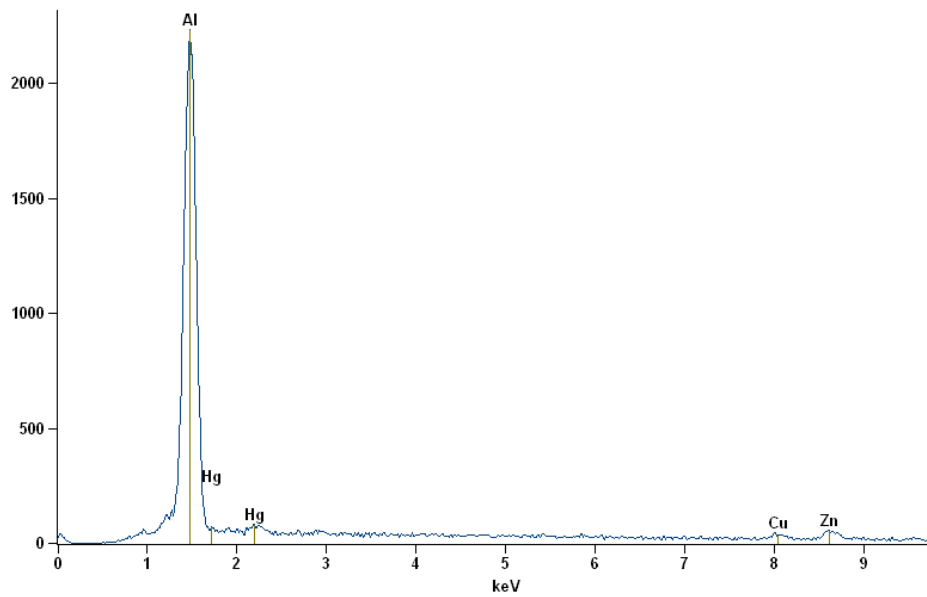


*Figure 3.29: EDX graph which details the materials present on the fracture surface of a specimen (S-L-11).*

## **CHAPTER 4 EXPERIMENTAL RESULTS**

A variety of experimental routines were implemented, as detailed in Chapter 3. Mechanical tests were conducted at the Mechanical Properties Characterization Laboratory (MPCL) at the University of Central Florida. The metallurgical analysis, primarily SEM imagery, was performed at the Materials Characterization Facility (MCF) located in Research Park at UCF. Calibration of the hardware utilized during the experiments is detailed, in an effort to be thorough and display the level of accuracy obtained through measurements. Discussion of the results is provided in Chapter 5. Experiments can be classified based upon the environment in which specimens were fractured in and by the routine used during the fracture process.

### **4.1 Crack Mouth Opening Displacement**

Compact tension,  $C(T)$ , specimens are designed in a manner that the crack mouth opening displacement,  $CMOD$ , can be easily related to the crack length,  $a$ . Specifically, through the use of a clip gage and data acquisition system, real-time crack lengths can be approximated during testing, as outlined by ASTM standards E399 and E1290. At the time of experimentation, clip gages were not able to be attached during experimentation in liquid environments; however, correlations between crosshead displacement, load and  $CMOD$  could be made.

#### 4.1.1 Crosshead Calibration

Correlation between  $CMOD$  and crosshead displacement was done in ambient laboratory air on a standard  $C(T)$  specimen. The specimen was cycled through approximately 40,000 cycles at various load ranges until complete failure. Maximum displacements for both the crosshead and the clip gage were extrapolated from the data, allowing for a comparison during the maximum load for each cycle, Fig 4.1. Linear regression analysis provided a fit with an  $R^2$  value

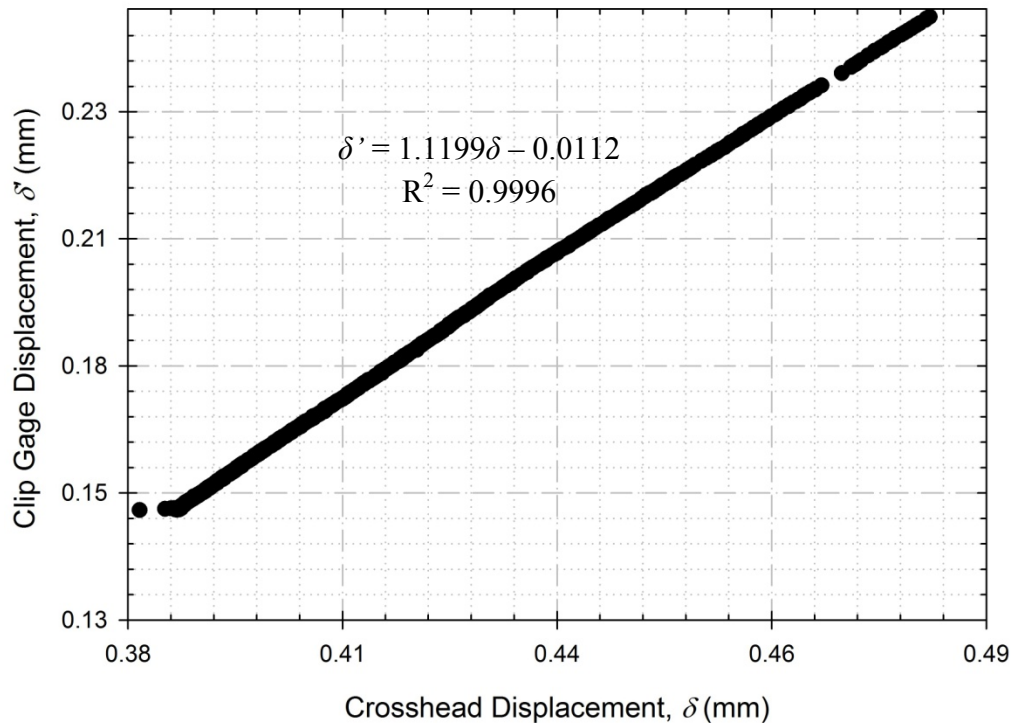


**Figure 4.1:** Relationship between crosshead and clip gage displacement readings.

of 0.9996, which translated to closely linear relationship. Utilizing the generated linear regression equation, i.e.,

$$\delta' = 1.1199\delta - 0.0112. \quad (4.1)$$

As such, CMOD can be accurately estimated through the crosshead displacement in the event that a clip gage cannot be used.

#### 4.1.2 Crack Length Measurements

Through the compliance technique outlined in ASTM E399 specifically for the  $C(T)$  specimen with integral knife edges,  $CMOD$  and crack length measurements can be calculated to within  $\pm 1\%$ . By measuring the load and the  $CMOD$ , or using the relationship between  $CMOD$  and crosshead displacement in the case where clip gages cannot be used, accurate predictions can be made regarding the size of the crack generated, i.e.,

$$a = W \left[ 1.000 - 4.500U + 13.157U^2 - 172.551U^3 + 879.944U^4 - 1514.671U^5 \right] \quad (4.2)$$

where

$$U = 1 / \left[ 1 + \left( EB V_m / (1 - \nu^2) P \right)^{\frac{1}{2}} \right]. \quad (4.3)$$

Using this method, real-time approximations of the SIF can be made, along with estimates at the crack length,  $a$ , Fig. 4.2.

Crack length-to-Width ratios,  $a/W$ , must lie between 0.2 and 0.8 to ensure that accuracy is within  $\pm 1\%$ . Given the specimen dimensions,  $a/W$  was satisfied immediately upon testing, as the EDM starter notch provided for a valid ratio. Only when fast fracture occurred was the ratio not satisfied.

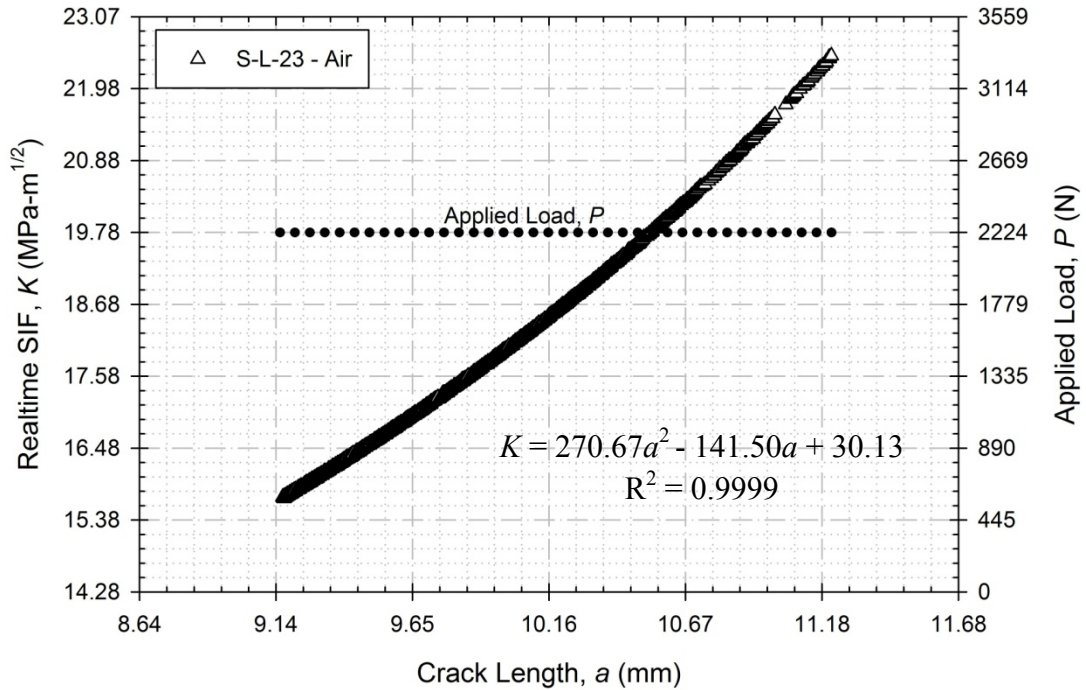


**Figure 4.2:** Relationship between SIF and crack length as measured during experimentation.

## 4.2 Fracture Toughness Testing in Air

Initial tests were conducted in static laboratory air to provide comparison values to those obtained in liquid environments. Two different load frames were utilized, as detailed in Section 3.2.1. Identical experimental setups were implemented on both frames in an effort to keep the results unified and comparable.

### 4.2.1 Plane Strain Fracture Toughness

Initial plane-strain fracture toughness values were obtained on the MTS Insight and the Teststar IIs, Table 4.1. Both values of  $K_{Ic}$  provide valid conditions set forth by Eq. 3.1a. Fatigue pre-cracks were generated under load control programs, cycling between 222.4 N (50 lbf) and 2224 N (500 lbf), resulting in a tension-tension fatigue routine with a load ratio,  $R_l$ , of 0.1. The Insight frame utilized a displacement rate to achieve the load control, at a displacement of 10.2 mm/min (0.4 in/min) while the Teststar IIs employed a load-control sine waveform at a frequency of 1 Hz. Typical values for the number of cycles required to generate a suitable fatigue pre-crack is detailed in Table 4.1.

**Table 4.1 – Plane Strain Fracture Toughness Values,  $K_{Ic}$ , in Air**

	$K_{Ic}$ [MPa-m <sup>1/2</sup> (ksi-in <sup>1/2</sup> )]	$a$ [mm (in)]	Cycles
<b>Insight - 5 kN</b>	25.6 (23.5)	10.1 (0.397)	≈3000
<b>Servohydraulic - 100 kN</b>	21.6 (19.8)	9.82 (0.387)	≈2000

### 4.2.2 Optical Microscopy of Fracture Specimens

Fracture surfaces of specimens fractured in air were observed under various magnifications through a digital microscope. Common features to fracture surfaces were observed, including the fatigue pre-crack region and shear lips, Fig. 4.3. Noticeable plastic deformation was seen (shear lips) while the fracture surface appeared relatively flat. Fatigue pre-cracks exhibited shiny, reflective portions (shown in Fig. 4.3 as dark spots), while the fast

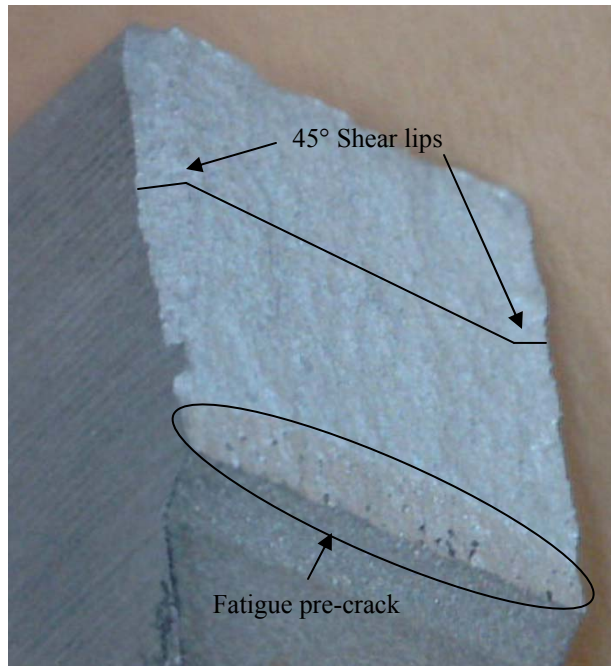


**Figure 4.3:** Fracture specimen fractured in air (S-L-16).

fracture surface was dull without many reflective particles. Clear distinctions between fatigue pre-cracks and fast fracture surfaces were observed.

#### 4.2.3 Scanning Electron Microscopy of Fracture Specimens

Fracture surfaces of fractured specimens fractured in air were subsequently viewed under a SEM, as detailed in Section 3.8.3. Fracture surfaces for specimens fractured in air all exhibited similar features in terms of fatigue pre-cracking and fast fracture portions. The overall fracture surface is shown in Fig. 4.4. Fatigue striations, with a spacing of approximately  $0.5 \mu\text{m}$  ( $19 \mu\text{in}$ ) between each striation, were observed as a result of the fatigue pre-cracking routine, Fig 4.5. A zoomed in portion in the fast fracture portion reveals finer details, including intergranular fracture and transgranular fracture of the inclusion particles, Fig. 4.6.

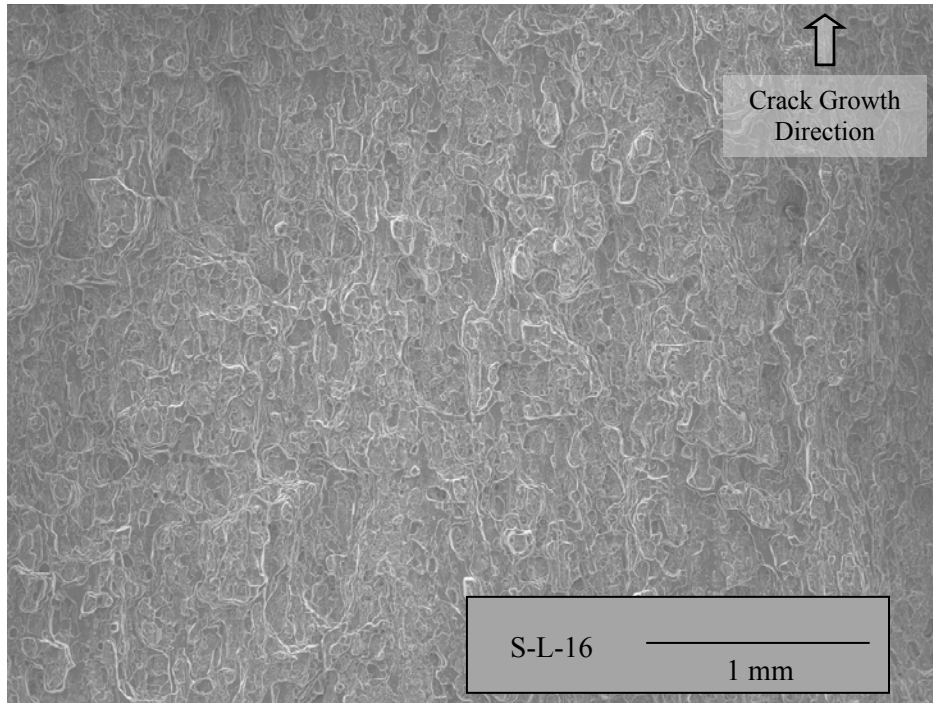


**Figure 4.4:** Low magnification view of fast fracture surface of specimen fractured in air (S-L-16).

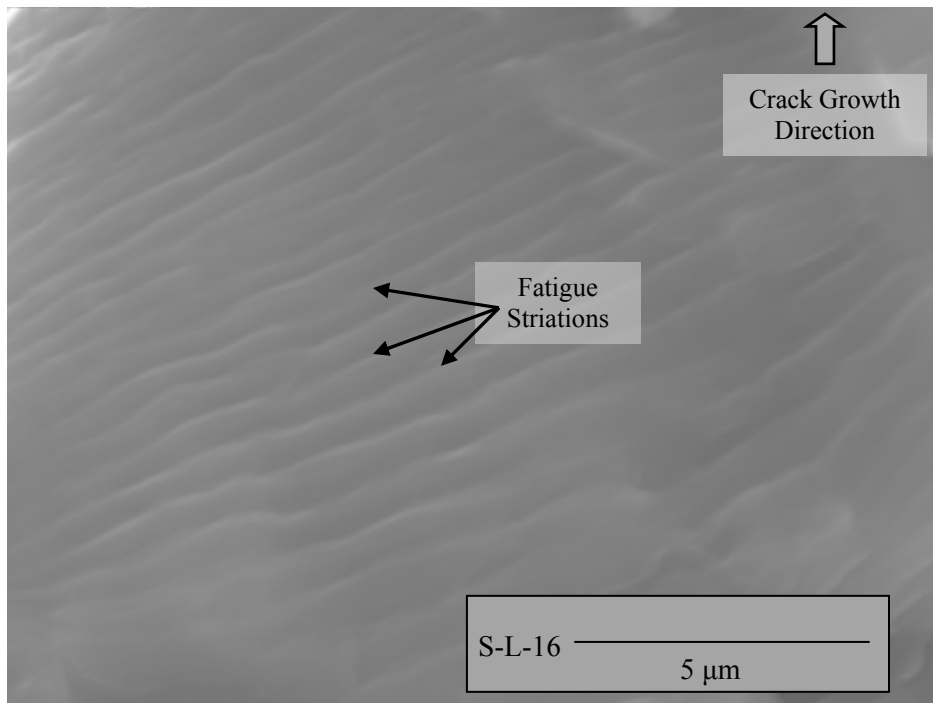


**Figure 4.5:** High magnification view of fatigue pre-crack region on specimen fractured in air (S-L-16).

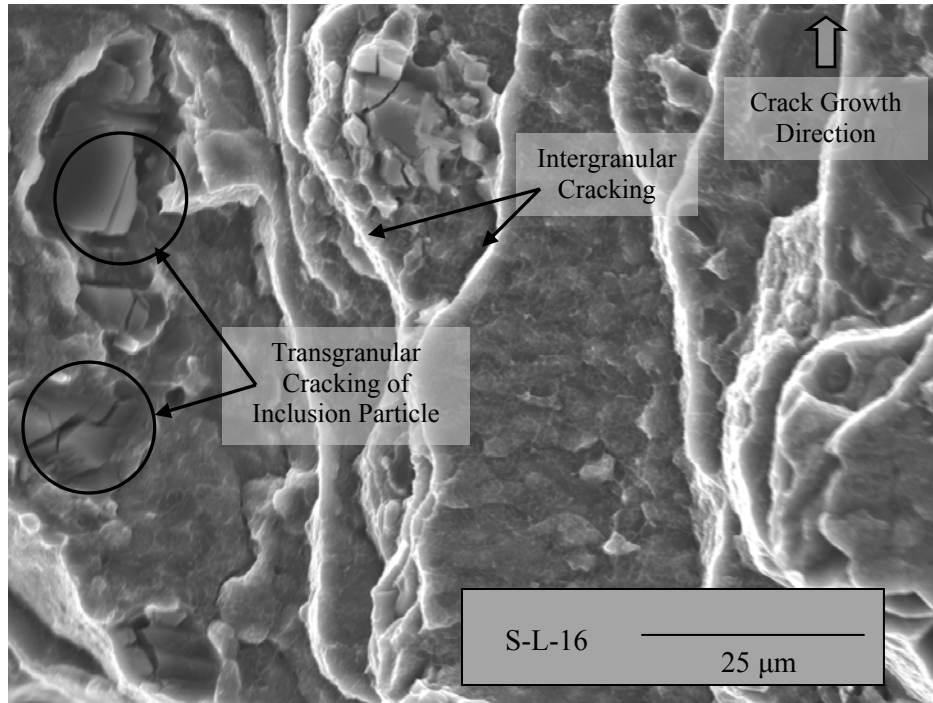


**Figure 4.6:** Close up view of fast fracture surface, displaying intergranular and transgranular cracking of grains and inclusions, respectively (S-L-16).

### 4.3 Fracture Toughness Testing in Saltwater

As previously discussed, testing in saltwater (3.5% NaCl) was done primarily to perfect the experimental routine. Saltwater, instead of tap water, was chosen for several reasons: it is a harmless liquid that can be easily cleaned up, it has a documented effect on the fracture strength of Al 7075 and results could be compared with other studies. Noticeable effects were observed; however, the implications of these results are not the focus of the current study.

#### 4.3.1 Plane Strain Fracture Toughness

The plane-strain fracture toughness of specimens fractured in 3.5% NaCl exhibited a decrease in fracture toughness. Depending on the pre-soak, pre-crack and fracture environment, the SIF was seen to fluctuate, Table 4.2. It can be seen that by altering the environment, there is an effect on the fracture toughness value.

**Table 4.2 – Plane Strain Fracture Toughness Values,  $K_{Ic}$ , in 3.5% NaCl**

Insight	Pre-Soak	Pre-Cracking	Fracture	$K_{Ic}$ [MPa-m <sup>1/2</sup> (ksi-in <sup>1/2</sup> )]
S-L-13	3.5% NaCl	3.5% NaCl	3.5% NaCl	23.1 (21.2)
S-L-14	3.5% NaCl	3.5% NaCl	Air	24.2 (22.2)
S-L-15*	Air	3.5% NaCl	3.5% NaCl	21.3 (19.5)

\*Allowed to incubate at load before conducting plane-strain fracture toughness tests.

Particularly, specimen S-L-15 displayed a reduction in the fracture toughness and can be attributed to the testing that it endured. This specimen was pre-cracked in 3.5% NaCl then loaded to 2201 N (495 lbf) and remained until fracture. The specimen sat at this load for 246,276 s (68.4 hours), in which no fracture occurred. In this study, this type of experiment is referred to as an incubation experiment in which delayed failure can be studied. Approximately 2.5 days after the initial load was applied, no change in deflection was observed, therefore it was determined that the specimen would not fail. It was then unloaded and a plane-strain fracture toughness test was conducted in the liquid. The value obtained is less than that of the other specimens and can possibly be attributed to the incubation period.

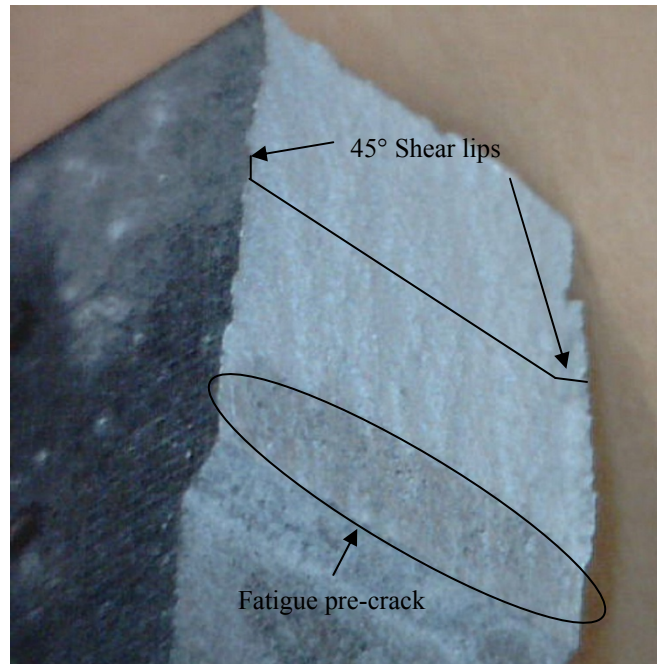


**Figure 4.7:** Fracture specimen fractured in 3.5% NaCl (S-L-14).

### 4.3.2 Optical Microscopy of Fracture Specimens

Fracture surfaces of specimens fractured in 3.5% NaCl displayed a similar surface as that of specimens fractured in air. Fatigue pre-cracks were more noticeable, as the surface is much darker than the fast fracture surface, Fig. 4.7. Shiny, reflective particles are still prominent within the fatigue pre-crack region, while the fast fracture surface is dull. Plastic deformation is present and is easily observed in the form of shear lips. The fast fracture surface is relatively smooth and followed the expected path for fracture.

### 4.3.3 Scanning Electron Microscopy of Fracture Specimens

Fracture surfaces of fractured specimens fractured in 3.5% NaCl were subsequently viewed under a SEM, as detailed in Section 3.8.3. Fracture surfaces for specimens fractured in 3.5% NaCl all exhibited similar features in terms of fatigue pre-cracking and fast fracture portions. The overall fracture surface is shown in Fig. 4.8. The fast fracture region is nearly

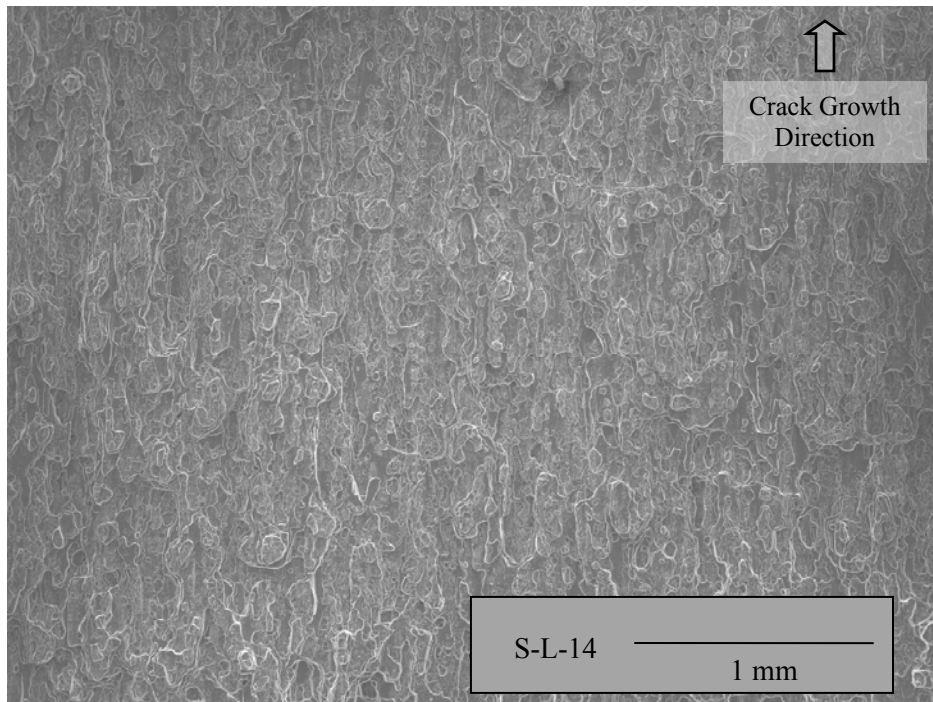


**Figure 4.8:** Low magnification view of fast fracture surface of specimen fractured in 3.5% NaCl (S-L-14).

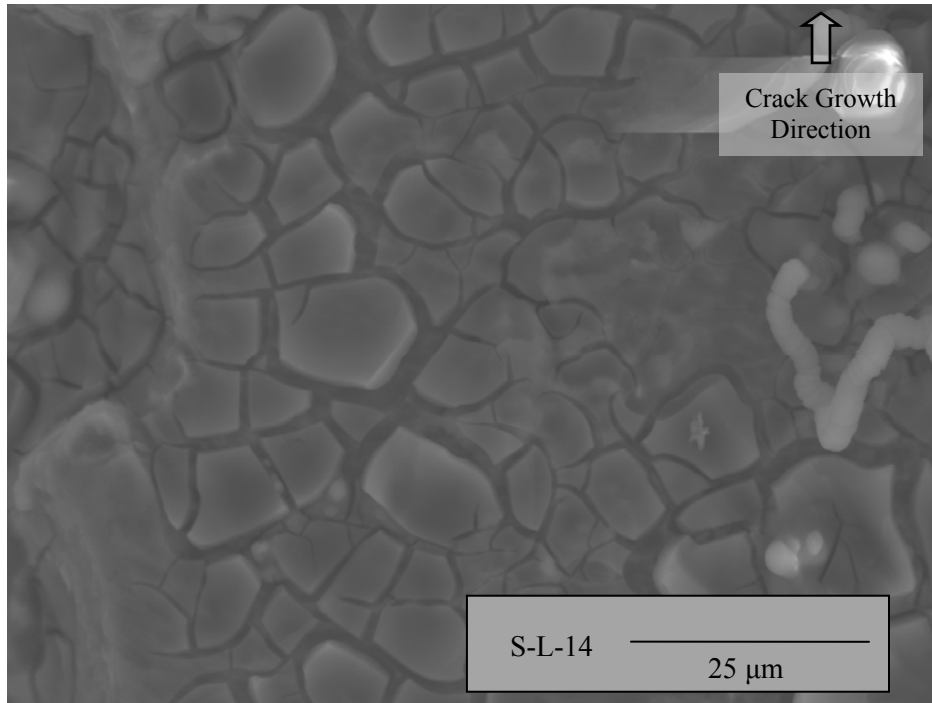


**Figure 4.9:** Magnified view of fast fracture surface of specimen fractured in 3.5% NaCl with salt residue remaining on fracture surface (S-L-14).

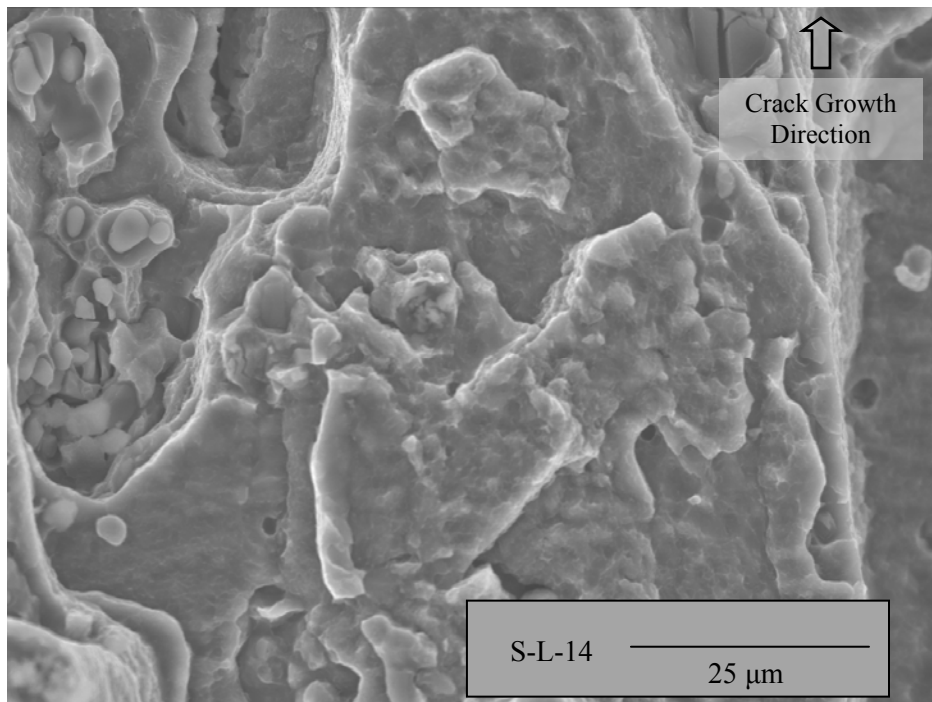


**Figure 4.10:** Magnified view of fast fracture surface, displaying intergranular and transgranular cracking of grains and inclusions, respectively, in 3.5% NaCl (S-L-14).

identical to the specimen fractured in a saltwater environment shown in Fig. 4.4. The fatigue pre-crack portion displays remnants of salt and some small fatigue striations, Fig 4.9. Peaks and valleys on the specimen surface have approximate lengths and widths of 0.5 mm (0.019 in) and 0.33 mm (0.013 in), respectively. These dimensions correspond to the approximate length and twice the width of a typical grain within the material.

A zoomed in portion in the fast fracture portion reveals finer details, including intergranular fracture and transgranular fracture of the inclusion particles, Fig. 4.10. Ultimately, the microscopic results are similar to those of specimens fractured in air.

#### 4.4 Fracture Toughness Testing in Liquid Mercury

Standard plane-strain testing was conducted in liquid mercury to establish the SIF without any incubation period. Standard plane-strain fracture toughness tests were implemented for this routine.

##### 4.4.1 Plane Strain Fracture Toughness

Submersing the fracture specimen in liquid mercury was done by housing both the specimen and liquid in the environmental bath outlined in Section 3.5. Pre-soak, pre-cracking and fracture environments were varied, similar to the method for specimens in 3.5% NaCl. Additionally, varying the environment led to a varying fracture toughness of the specimen, shown in Table 4.3.

**Table 4.3 – Plane Strain Fracture Toughness Values,  $K_{Ic}$ , in Liquid Hg**

<b>Insight</b>	<b>Pre-Soak</b>	<b>Pre-Cracking</b>	<b>Fracture</b>	$K_{Ic}$ [MPa-m <sup>1/2</sup> (ksi-in <sup>1/2</sup> )]
S-L-5	Hg	Air	Air	22.3 (20.8)
S-L-11	Hg	Hg	Hg	26.7 (24.5)
S-L-18*	Air	Hg	Hg	27.0 (24.8)
<b>Servo-hydraulic</b>	<b>Pre-Soak</b>	<b>Pre-Cracking</b>	<b>Fracture</b>	$K_{Ic}$ [MPa-m <sup>1/2</sup> (ksi-in <sup>1/2</sup> )]
S-L-17*	Air	Hg	Hg	24.9 (22.7)

\*Comparison between these and other fracture toughness values will be carried out in Chapter 5.

Fatigue pre-cracks were generated under load control programs, cycling between 222.4 N (50 lbf) and 2224 N (500 lbf), resulting in a tension-tension fatigue routine with a load ratio,  $R_L$ , of 0.1. The Insight frame utilized a displacement rate to achieve the load control, at a displacement of 10.2 mm/min (0.4 in/min) while the Teststar IIs employed a load-control sine waveform at a frequency of 1 Hz. Fracture testing was conducted at a displacement rate of 7.6 mm/min (0.3 in/min) on the Insight and at a load rate of 89 N/s (20 lbf/s) on the Teststar IIs.

#### 4.4.2 Optical Microscopy of Fracture Specimens

Fracture surfaces of standard plane-strain were observed through a digital microscope, which were significantly different than those of specimens fractured in air or saltwater. Plastic deformation was no longer present, as the fracture surface was multi-layered and multi-colored, Fig. 4.11. Crack initiation sites were observed on several layers, at approximately the height of the grain boundary, suggesting that each crack initiated at a grain boundary, Fig 4.12. The specimen appears to have failed by a “delamination-like” failure, where failure initiated along grain boundaries at the starter notch. The layers were also significantly discolored, suggesting that some type of corrosion had occurred.

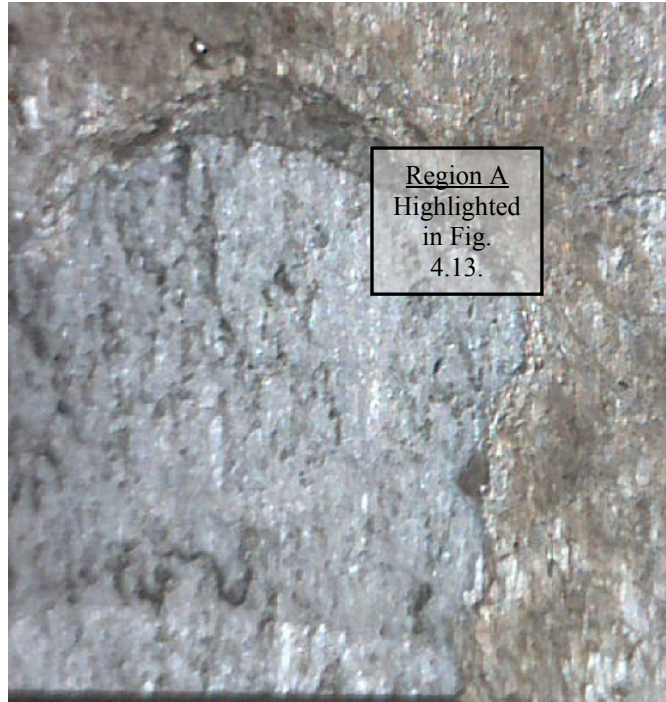


**Figure 4.11:** Specimen fractured in a liquid Hg environment (S-L-11).

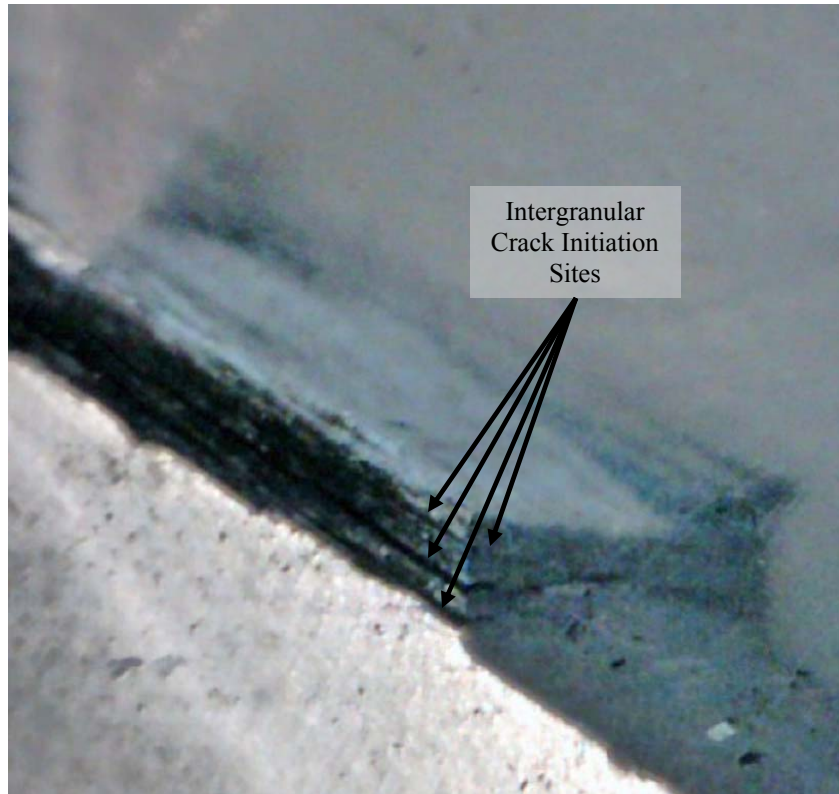


**Figure 4.12:** Multiple crack initiation sites along EDM starter notch (S-L-11).

#### 4.4.3 Scanning Electron Microscopy of Fracture Specimens

Fracture surfaces observed under SEM were notably different than those fractured in air and saltwater. When viewed at low magnification, portions of the fracture surface exhibited a failure mode similar to that of specimens fractured in air and a failure mode that was previously unseen. Specifically, Region A, from Fig. 4.11, was observed to distinguish the two failure modes, Fig. 4.13. The lower left portion is similar in appearance to specimens fractured in air or saltwater, while the upper right has transgranular-like fracture features.

Fatigue pre-cracking was successfully done in liquid Hg. Fatigue pre-cracks exhibited striations to that of specimens fractured in air and saltwater; however, large transgranular cracks are present, Fig. 4.14. The main transgranular crack shown in Fig. 4.14 extends in the direction of crack growth; this large crack could be the result of secondary cracking.

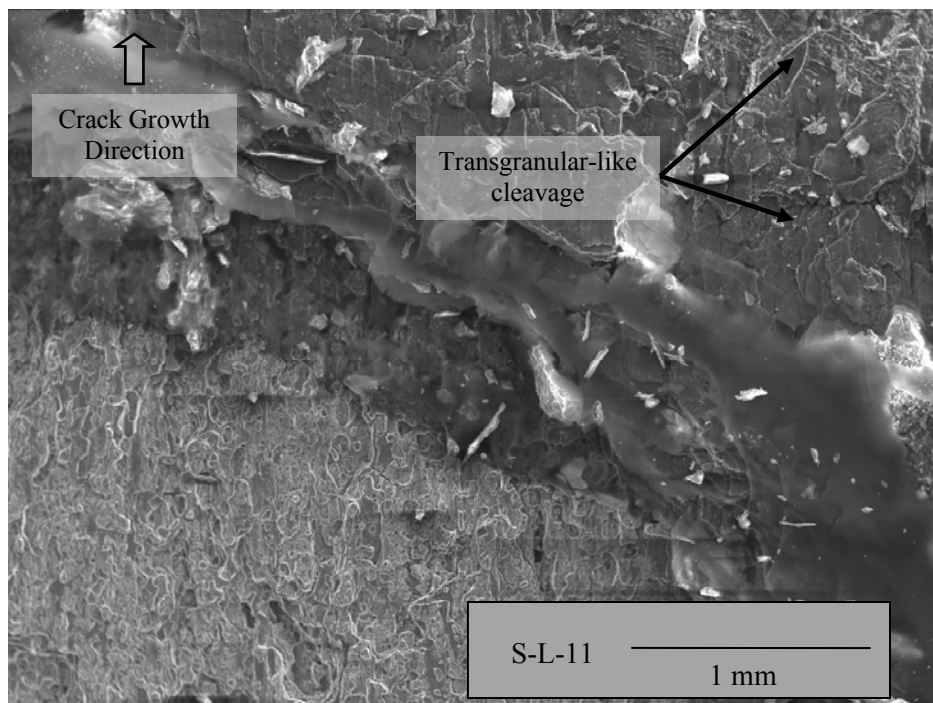


**Figure 4.13:** Region A, from Fig. 4.11, magnified to show transition between failure modes (S-L-11).

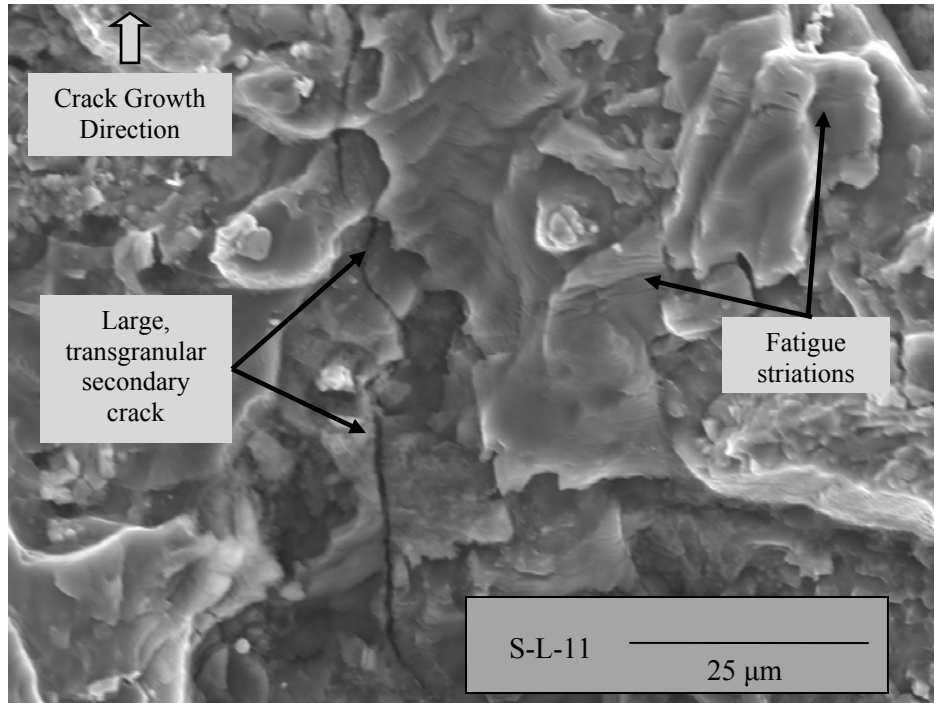


**Figure 4.14:** Fatigue pre-crack region of a specimen tested in liquid Hg, with large transgranular crack (S-L-11).

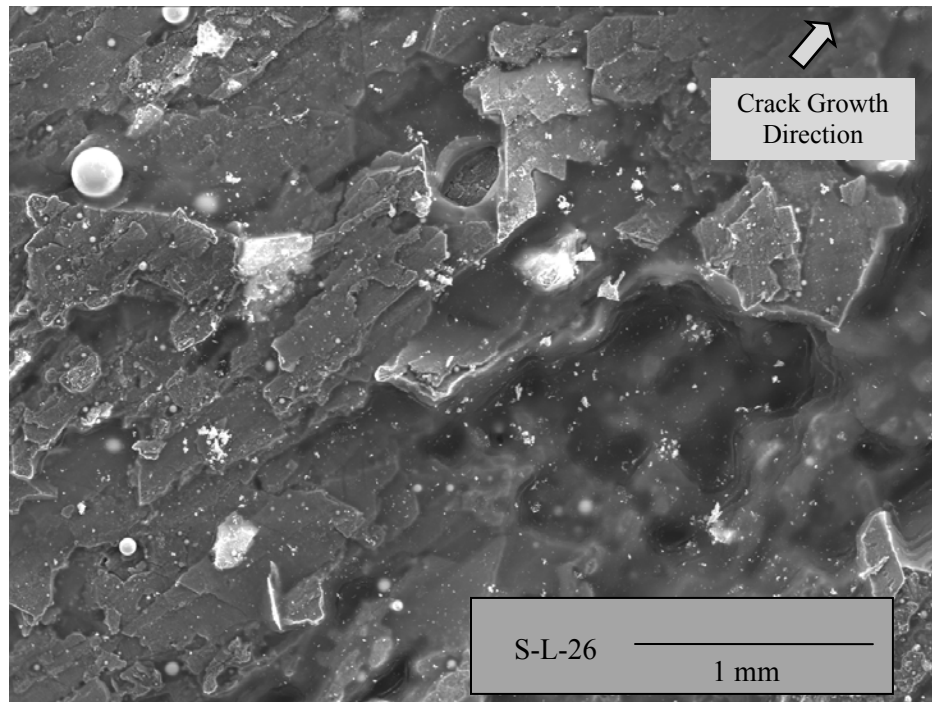


**Figure 4.15:** Fast fracture surface of a specimen fractured in liquid Hg (S-L-26).

Using a similar scale as the other environmental cases, the fast fracture surface is considerably different, Fig. 4.15. The fast fracture surface in mercury displays less granular steps, as the surface is relatively smoother. Only a small amount of transgranular fractured inclusions are seen.

#### **4.5 Stress Intensity Factor Incubation**

The main goal of this research was to establish a relationship between the SIF and the time to failure of aluminum specimens in a liquid metal environment. The process of pre-cracking, fracturing and incubating was detailed in Section 3.6.3. Specimens were pre-cracked within the liquid environment, unloaded, then loaded to an initial SIF; some percentage of the plane-strain fracture toughness that was found through previous experiments. It must be noted that SIF values could only be determined after the test was performed.

##### **4.5.1 SIF in Saltwater**

An incubation experiment was conducted in saltwater for the sole purpose of exposing any leaks that might develop while the specimen was under load. A specimen (S-L-15) was pre-cracked, unloaded and loaded to an estimated level of 80% of the plane-strain fracture toughness ( $16.9 \text{ MPa}\cdot\text{m}^{1/2}$  [ $15.5 \text{ ksi}\cdot\text{in}^{1/2}$ ]) that was observed during tests in saltwater. After approximately 2.5 days, no leaks were observed nor had the specimen failed. The specimen was then unloaded and a standard plane-strain fracture toughness test was conducted, as detailed previously in Table 4.2. Based on the findings from this test, liquid mercury could be used as the liquid environment for future testing.

##### **4.5.2 SIF in Liquid Mercury**

Incubation experiments were conducted in liquid mercury on the servohydraulic MTS load frame. This frame was chosen as the PID controls were tuned to able to maintain load

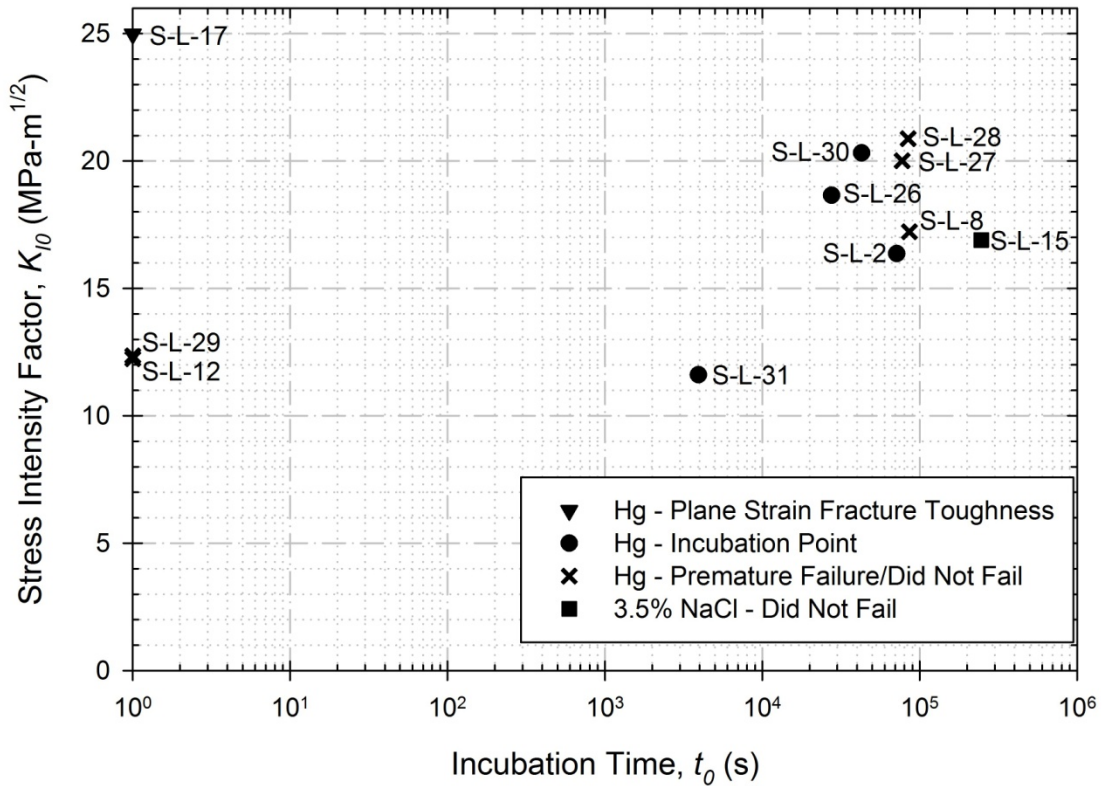


**Figure 4.16:** Time required for complete failure of a specimen based on an initial SIF value.

within  $\pm 0.3\%$  of the required to achieve the desired SIF. The results from several incubations are shown in Fig. 4.16.

Several specimens failed prior to incubation times, as noted as a dot on y-axis at  $t_0 = 10^0$ . Specimens typically failed during the pre-cracking routine; all of which failed at the EDM starter notch, as the PlastiDip solution was successful. Several other specimens lasted the full pre-cracking regime and were allowed to incubate until failure. Displacements and loads remained constant up until complete fracture of the specimen occurred, which occurred in less than 0.1 s. Crack growth data was not able to be extrapolated, as the sampling frequency was 10 Hz. The crack was able to extend through the width of the specimen before a subsequent data point was captured.

### 4.5.3 Optical Microscopy of Fracture Specimens

Fracture surfaces of specimens fractured during SIF incubation experiments displayed a similar failure mode as the plane-strain fracture toughness specimens submerged in liquid Hg. A view of the side of a specimen displays the severity of cracking and the lack of plastic deformation when submerged in a liquid metal, Fig. 4.17. Cracks were initiated in several locations and the “delamination flakes” were observed; however, the flakes were severed from the specimen, Fig. 4.18. The flakes exhibited similar fracture surfaces as the rest of the specimens, including dark regions that signify corrosion.

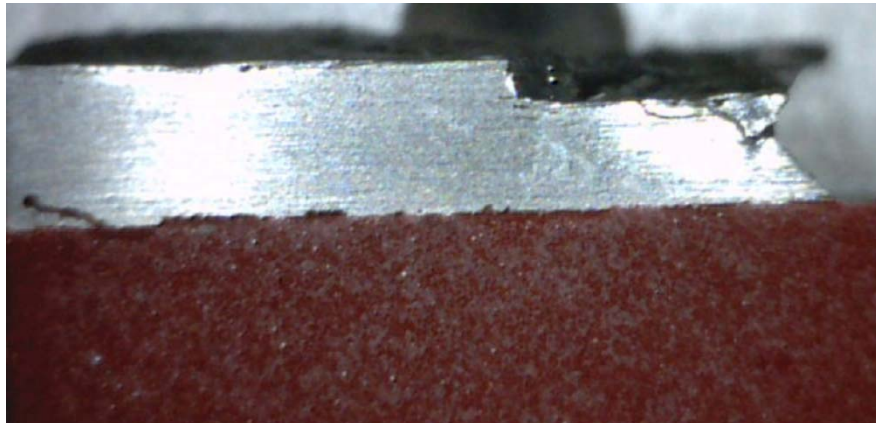


*Figure 4.17: Side view of a specimen incubated in liquid Hg (S-L-30).*



*Figure 4.18: Intergranular flake from specimen incubated in liquid Hg (S-L-30).*

#### 4.5.4 Scanning Electron Microscopy of Fracture Specimens

The fracture surfaces of specimens that incubated in liquid Hg displayed similar features as specimens that underwent plane strain fracture tests. A zoomed out picture of the fast fracture surface is shown. The surface slightly resembles that of experiments conducted in air, but with small portions of flatter areas, as highlighted in Fig. 4.19. These flatter areas were not observed on specimens fracture in air, Fig. 4.4, or saltwater, Fig. 4.8. The surface of these fracture regions are magnified in Fig. 4.20. A more generic example of a fast fracture surface generated in the presence of liquid mercury during an incubation experiment is shown in Fig. 4.22. Cleavage-like fracture is far more dominant, suggesting an extremely brittle fracture occurred. Ultimately, the fracture surfaces of specimens incubated resembled the surfaces of plane strain fracture surfaces.

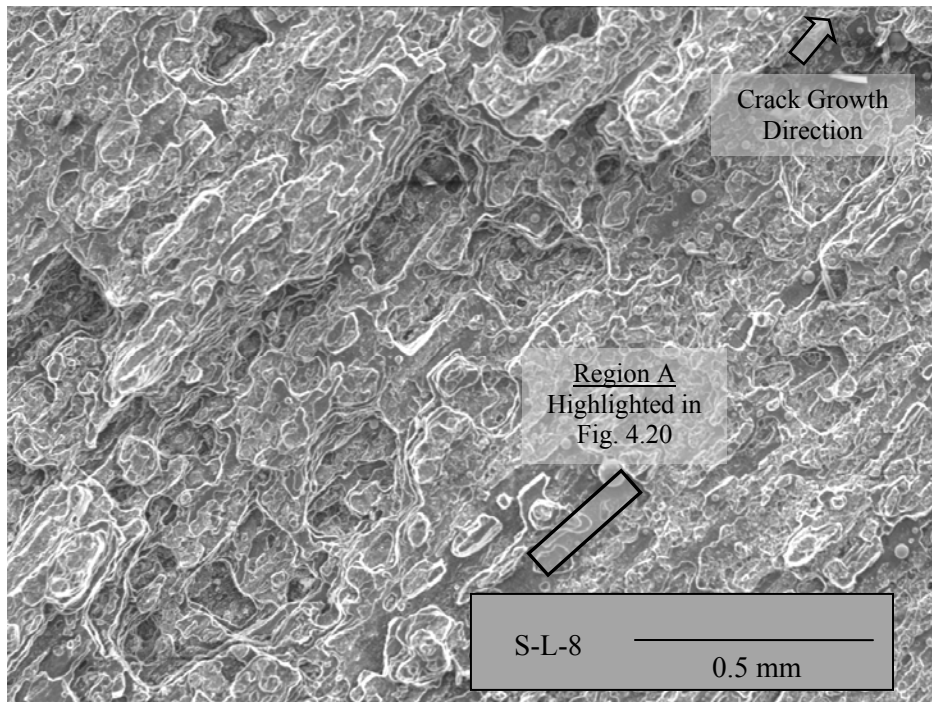


**Figure 4.19:** Fast fracture surface of an incubated specimen in liquid Hg (S-L-26).

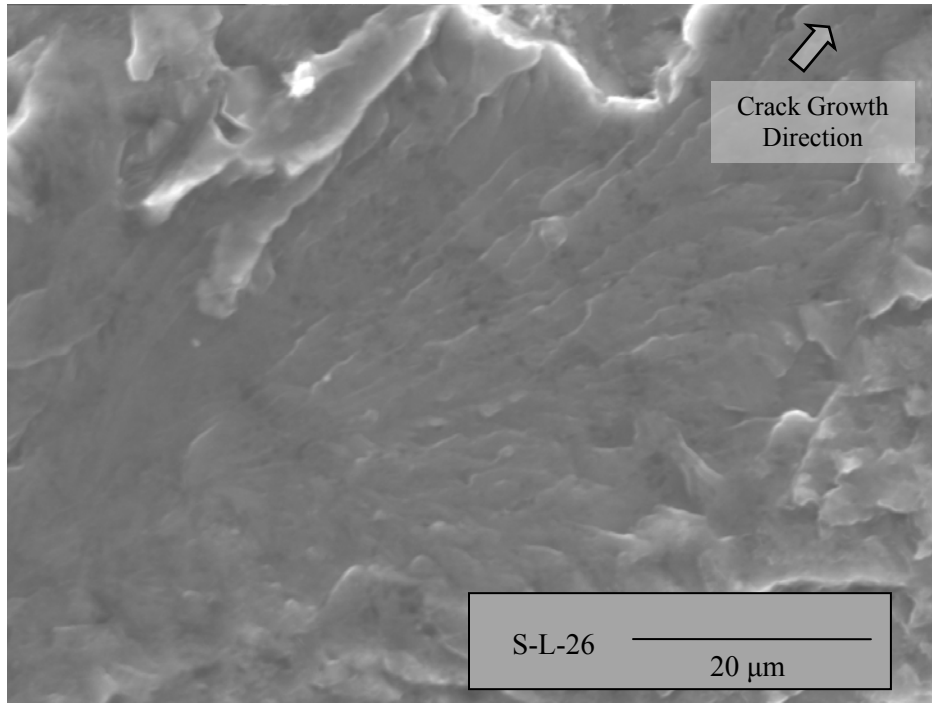


**Figure 4.20:** Detailed view of Region A from Fig. 4.19, displaying transgranular-like cleavage fracture (S-L-26).

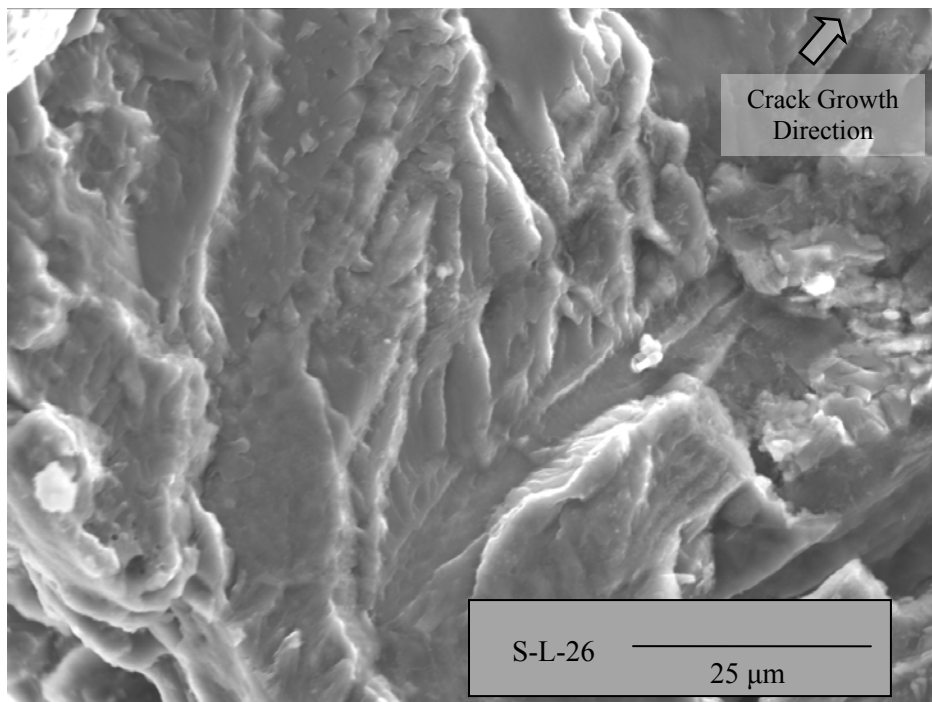


**Figure 4.21:** Fast fracture surface of an incubated specimen in liquid Hg (S-L-26).

## CHAPTER 5 DISCUSSION

The experimental results provided for several topics of discussion. Implications of the results from the work in the previous chapters are further developed here.

### 5.1 Crack Mouth Opening Displacement

Calibration of the clip gage, or *CTOD* gage, on the MTS load frames was relatively straightforward. The gage has a universal MTS adapter, therefore it was able to be installed on any of the software packages produced by MTS. Initial calibration of the device was done by an MTS service representative, which ensured the accuracy of the measurements.

Due to the restrictive nature of the environmental bath, the clip gage could not be utilized during experiments that were submersed in a fluid. In order to achieve approximations of the crack length, correlations between the displacement reported by the load frame and by the clip gage were made. As shown, the relationship between crosshead displacement and clip gage displacement was highly linear, with an  $R^2$  value of 0.9996.

The ability of being able to approximate the *CMOD* through load frame displacement allowed for the use of compliance methods, detailed in Section 4.1, to be used to calculate the crack length. This proved to be extremely useful when specimens were submersed in a liquid because cracks were neither visible nor accessible as they were when testing in air. Once a suitable crack length approximate was made, the pre-cracking cycles were stopped and further tests could be conducted on the specimen.

Since many cases studied lacked subcritical crack growth, knowing the actual crack length was not needed. Fluctuation in the load and displacement sufficed for crack length approximations in many instances.

## 5.2 Fracture Toughness in Air

Fracture testing in a laboratory environment was carried out with relative ease and simplicity. Specimens were able to be fatigue pre-cracked, unloaded and loaded through a plane-strain fracture toughness test. The results obtained differed slightly between the two load frames and served as a baseline value of  $K_{Ic}$  for subsequent tests on the respective load frame.

### 5.2.1 Fatigue Pre-cracking

Fatigue pre-cracks were generated in a similar fashion for both load frames. The Insight frame utilized a triangular waveform with a crosshead displacement rate of 10.1 mm/min (0.40 in/min) while the servohydraulic frame utilized a sine waveform with a loading frequency of 1 Hz, Fig. 5.1. Fatigue pre-cracks generated on the Insight took between 2-3 hours to achieve a suitable length and 0.5 hours on the servohydraulic frame. The discrepancy between the two is the control type, as the Insight is not as capable as the servohydraulic frame in terms of loading rates. The maximum loading rate while achieving accurate maximum and minimum loads was approximately 0.2 Hz. The servohydraulic frame was much better suited for the cyclic loading.

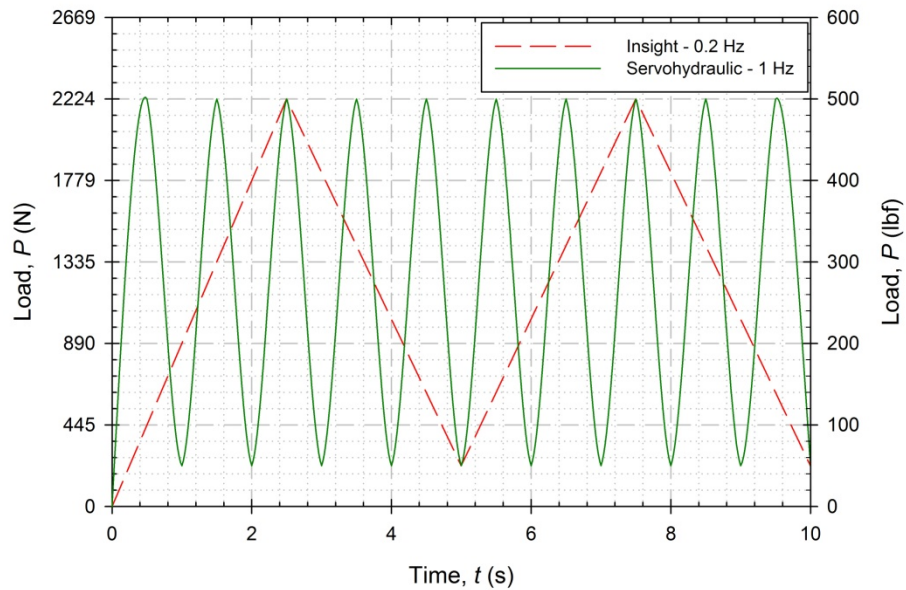


*Figure 5.1: Comparison of loading rates during fatigue pre-cracking of specimens.*

The fatigue pre-cracks that were generated on both frames were within the limits of ASTM E399. Fatigue pre-cracks generated on the Insight grew at a rate,  $da/dN$ , of  $3.93 \cdot 10^{-3}$  mm/cycle ( $0.155 \cdot 10^{-3}$  in/cycle) and  $3.76 \cdot 10^{-3}$  mm/cycle ( $0.148 \cdot 10^{-3}$  in/cycle) on the servohydraulic frame. The discrepancy between the two rates is less than 5%, but contributed to the variance in  $K_{Ic}$  of the material. During the fatigue pre-cracking, longer cracks were generated on the Insight, resulting in a higher value of  $K_I$  applied during subsequent cycles. The larger value of the stress intensity applied resulted in a larger plastic zone size ahead of the crack tip, resulting in a higher value of  $K_{Ic}$  for specimens tested on the Insight, as depicted by the results.

Upon rupture, striations were observed under SEM. Pre-cracks were generally uniform across the entire specimen thickness. Surfaces were slightly darker than the fast fracture area and included some reflective particles. Overall, the pre-cracking of specimens in air went smoothly without any issues.

### 5.2.2 Plane Strain Fracture Toughness

Fracture tests in air were conducted on both load frames with values of the  $K_{Ic}$  varying based on the frame used. The load pattern varied for each, as the Insight used a displacement rate and the servohydraulic frame used a load rate. Ideally, both frames would have utilized a load rate instead of a displacement rate in an effort to keep test methods uniform, regardless of the frame used. To ensure that tests in air and liquid environments were similar, loading rates were slightly lower than the recommended rate of 0.34 kN/s (4500 lbf/min). The slightly lower rate was thought to promote proper wetting and interactions between the solid and liquid metal for tests conducted in liquid environments.

Plane-strain fracture toughness values were 15-20% higher on the Insight than on the servohydraulic frame. Both of the values obtained,  $25.6 \text{ MPa}\cdot\text{m}^{1/2}$  ( $23.5 \text{ ksi}\cdot\text{in}^{1/2}$ ) on the Insight

and  $21.6 \text{ MPa}\cdot\text{m}^{1/2}$  ( $19.8 \text{ ksi}\cdot\text{in}^{1/2}$ ) on the servohydraulic are greater than published values of the  $K_{Ic}$  of S-L oriented AL 7075-T-651 specimens by 29.1% and 8.8%, respectively. As discussed previously, this discrepancy is attributed to the plastic zone size ahead of the crack tip. Fatigue pre-cracks were longer in specimens tested on the Insight, resulting in a larger  $\Delta K$  applied during the pre-cracking routine. This larger  $\Delta K$  work hardened a small portion of material ahead of the crack tip, resulting in a larger value of  $K_{Ic}$ . Although each frame provided different values of the  $K_{Ic}$ , the values obtained on each were grouped within 10% of each other. Results were higher than expected; however, they were precise in regards to other, similar tests on the respective load frame.

### 5.2.3 Microscopy of Fracture Specimens

Fracture specimens were observed under digital and scanning electron microscopes. Both levels of magnification provided valuable information. These observations provided base qualitative data to be compared with future experiments conducted in liquid environments.

Under the digital microscope, a relatively smooth fracture surface was observed. Plastic deformation, in the forms of shear lips, was exhibited on both sides. The shear lips were formed at  $45^\circ$  angles relative to the fracture surface. Shear lips are a result of plane-stress conditions near the surface of the specimen. Specimens are designed in a fashion to exhibit plane-strain conditions to provide a material property and avoid thickness affects. By comparing the width of the shear lips, typically  $0.356 \text{ mm}$  ( $0.014 \text{ in}$ ) in samples tested in air, with the size of the fast fracture surface, these effects at the edge can be considered negligible. Fast fracture surfaces varied in color from the pre-crack, as they were lighter in appearance and lacked many of the reflective particles that existed in the pre-crack region. Fast fracture regions appeared smooth and appeared as expected.

Fracture surfaces of specimens fractured in static laboratory air were observed under SEM. Surfaces were relatively smooth with small peaks and valleys. Fatigue striations were observed in the pre-crack portion. Spacing of the striations, approximately  $0.50\ \mu\text{m}$  ( $19.7\ \mu\text{in}$ ), was consistent with expected values for the loading rate and load ratio,  $R_I$ , used during the pre-crack routine.

At higher magnifications under the SEM, the fracture appeared to occur in an intergranular fashion. Grains within the aluminum appeared to be intact and cracks were not observed within; however, inclusion particles were observed to have failed in a transgranular fashion. Large, prominent cracks were observed in many of the particles that existed in the grain boundaries. The overall fracture surface appeared to have failed in an intergranular manner, while the inclusion particles failed in a transgranular manner.

### **5.3 Fracture in Saltwater**

Fracture specimens fractured in 3.5% NaCl were subjected to both plane-strain fracture and incubation experiments. As stated previously, the purpose of these experiments were to provide verification that the environmental bath was suitable for testing and to ensure that all test material could be recovered. An additional benefit to testing in saltwater was the known susceptibility of Al 7075 to stress corrosion cracking. The results that were obtained could be compared with existing results and determine any correlations between test methods.

Fatigue pre-cracking, fracture toughness and incubation experiments were conducted in the saltwater without any issue. Specimens required similar amounts of cycles to generate an acceptable pre-crack length. Pre-cracks were more discolored than those of specimens fractured in air. Pre-cracks contained a similar amount of reflective particles as specimens fractured in air.

Fracture toughness values were observed to decrease, approximately a 10% reduction, as a result of testing in the liquid. The fast fracture area was similar to that of the fast fracture surfaces of specimens tested in air; the surface was relatively flat and specimens exhibited plastic deformation in the form of shear lips. Once again, the shear lips were at a 45° angle to the surface of the specimen and accounted for approximately 4% of the fast fracture surface. The overall surface was flat and lighter in appearance than the pre-crack portion.

An incubation test conducted on a specimen in saltwater was done so with an initial anticipated  $K_{I0}$  of 19.8 MPa-m<sup>1/2</sup> (18.0 ksi-in<sup>1/2</sup>) and was measured to have incubated at 17.0 MPa-m<sup>1/2</sup> (15.5ksi-in<sup>1/2</sup>). After the specimen failed to rupture after 2.5 days, the load was removed and a plane-strain fracture toughness test was conducted. The result was a  $K_{Ic}$  of 21.3 MPa-m<sup>1/2</sup> (19.5 ksi-in<sup>1/2</sup>); approximately 8.5% lower than other values obtained in saltwater. The reduction is attributed to the time the specimen spent incubating.

Fracture surfaces were observed under assorted magnifications. Under the digital microscope, the shear lips, reflective particles and a relatively smooth fracture surface was observed. Under the SEM, similar features were observed in terms of intergranular cracking of aluminum and transgranular cracking of inclusion particles. No extreme differences between specimens fractured in air were observed.

The ultimate goal of testing in saltwater, to prove the environmental bath worked properly, was achieved. The bath was able to contain the liquid for extended periods of time and the fluid was able to be recaptured upon completion of the tests. The chamber functioned properly and was suitable for future tests involving various liquid-solid metal combinations.

## 5.4 Fracture in Liquid Mercury

Liquid metal embrittlement experiments were conducted in the environmental chamber at room temperature. Specimens were able to be pre-cracked, loaded and held under load for extended periods of time in liquid mercury. Several observations were made during the course of the experiments.

### 5.4.1 Fatigue Pre-cracking

Fatigue pre-cracks were generated in a liquid metal, similar to saltwater. The routines were similar to that of tests in saltwater, with the only differences coming from the load frame used. Crack growth rates, on a per cycle basis, were similar to specimens pre-cracked in air.

#### 5.4.1.1 *Insight Load Frame*

The Insight load frame generated pre-cracks in 2700-3000 cycles, typically between 2-3 hours. The crack lengths were comparable to those generated on specimens in air and saltwater. The cracks were generated while submersed in liquid mercury, eliminating any possible competition between oxidation and LME effects. As the pre-cracks grew in length, the only medium available to the newly created surfaces was liquid mercury.

#### 5.4.1.2 *Servohydraulic Load Frame*

Generating pre-cracks on the servohydraulic load frame was much faster at about 1900 cycles, averaging approximately 30 minutes to achieve a suitable crack length. The cracks were slightly shorter than those generated on the Insight, approximately 0.50 mm (0.02 in) shorter, but still suitable for fracture toughness tests. As with specimens pre-cracked on the Insight, the only medium exposed to the newly created surfaces was liquid mercury.

#### 5.4.1.3 *Issues with Pre-cracking*

Several issues arose during the course of pre-cracking on both load frames. Most issues were observed on the Insight, as testing was initially conducted on this frame. The main issue was specimens had a tendency to crack and rupture in locations other than the starter notch.

During the pre-cracking, some specimens fractured through regions around the load pin hole. Specimens were rupturing at various locations throughout the knife edge valley. It was initially thought that the geometry of the specimens resulted in a stress concentration at the knife edge valley. This stress concentration was thought to be generating a critical stress that could rival the stress experienced at the starter notch. Finite element analyses revealed that there was a buildup of stress at this location, but not greater than that at the starter notch. Specimens were redesigned that eliminated the stress concentration by adding a fillet to the knife edge valley.

Another possibility of the premature rupture of specimens could be contributed to the microstructural orientation within the aluminum. As specimens are machined in the S-L orientation, cracks are expected to propagate in the L direction, perpendicular to the S direction. This direction provides for the most grain boundaries available at the surface as measured in a perpendicular direction; namely the S direction. At these locations, abnormally large amounts of alloying elements could be present, which could facilitate fracture at a low stress. As several alloying elements were seen to fail in a transgranular fashion through SEM observations, a large concentration of alloying elements could result in a lower resistance to fracture.

Upon implementing the newly redesigned specimens, unexpected ruptures continued to occur at locations near the load pin hole. Even with the rounded knife edge valley, crack initiation and propagation continued to occur. The alignment of the Insight load frame was verified, eliminating any issues with load eccentricity. The cause was determined to be crack initiation at random locations where a critical stress or favorable microstructural orientation

existed, coupled with the corrosive nature of the liquid metal, promoted wetting and the propagation of a crack.

To prevent attack by liquid mercury at locations other than the starter notch, rubberized coatings were applied to the lower half of specimens. This coating allowed for the specimen to be completely protected from the liquid below the starter notch. After filling the cup with liquid, a 1.78 mm (0.07 in) strip of aluminum around the starter notch was exposed, forcing crack initiation to occur at the notch. This approach proved to be a successful modification, as crack initiation and propagation started at positions along the starter notch in all subsequent tests.

Pre-cracking conducted in the servohydraulic load frame did not exhibit any errant crack initiation or propagation; however, some specimens failed abruptly during the pre-crack regime. Specimens S-L-12 and S-L-19 failed at the second and 1083 cycle, respectively. Cracks were initiated at the starter notch and fracture surfaces appeared similar to that of specimens that failed at the desired location. Both specimens failed to generate a pre-crack, given the small amount of cycles that each endured, and the calculated  $K_{Ic}$  was 12.24 MPa-m<sup>1/2</sup> (11.14 ksi-in<sup>1/2</sup>) for S-L-12 and 12.35 MPa-m<sup>1/2</sup> (11.24 ksi-in<sup>1/2</sup>) for S-L-29. The lack of a pre-crack is suspicious and reiterates the point that a critical stress, as a result of an applied stress or a stress concentration, is a primary concern in LME characterization.

#### 5.4.2 Plane Strain Fracture Toughness

Fracture specimens that survived the full pre-cracking routine were then subjected to plane-strain fracture toughness tests. Tests were initially conducted on the Insight load frame, followed by experiments on the servohydraulic frame.

#### 5.4.2.1 *Insight Load Frame*

Plane-strain fracture toughness tests conducted on the Insight resulted in an increase of the  $K_{Ic}$  of aluminum. Specimen S-L-11, which was pre-cracked and fractured in liquid mercury, had a calculated  $K_{Ic}$  of 26.7 MPa-m<sup>1/2</sup> (24.5 ksi-in<sup>1/2</sup>). Additional specimens, e.g. S-L-18 and S-L-20, had significantly larger values; 27.3 MPa-m<sup>1/2</sup> (24.8 ksi-in<sup>1/2</sup>) and 27.8 MPa-m<sup>1/2</sup> (25.3 ksi-in<sup>1/2</sup>).

The initial test on S-L-5 was done using 99.999% pure mercury. As the tests continued, the mercury became a darker gray color, indicative of contamination. Subsequent tests that were conducted in the re-used mercury appeared to behave more like specimens fractured in air. There were no burn marks, dark regions or any significant evidence that the mercury had an effect on the aluminum. Possible contamination occurred from mercury oxidation, interactions with previous specimens and the tension testing clevises. New mercury was implemented in following experiments, in an effort to eliminate contamination during testing.

Coating the tension clevis in the rubberized coating assisted in preventing contamination from outside sources. The mercury no longer reacted with the steel, reducing the likelihood of contamination as a result of the contact between steel and mercury. With these components coated, the newly acquired mercury did not change colors as readily as before, enabling more experiments to be conducted.

#### 5.4.2.2 *Servo-hydraulic Load Frame*

Plane-strain fracture toughness tests conducted on the servo-hydraulic frame were conducted with unused mercury. The result was an increase in the  $K_{Ic}$  when compared to the fracture toughness in air; 24.9 MPa-m<sup>1/2</sup> (22.7 ksi-in<sup>1/2</sup>) to 21.6 MPa-m<sup>1/2</sup> (19.8 ksi-in<sup>1/2</sup>), or a

14.6% increase. When compared to the values obtained by the Insight, a 3.5% decrease in the critical SIF was observed.

The unused mercury attacked the specimen as planned and there were no errant crack initiations/propagations on any specimen conducted on the servohydraulic frame. The rubberized coatings continued to provide protection to critically stressed regions of the specimen, allowing for crack growth to occur at the desired location. The coatings also helped to keep the liquid mercury from becoming contaminated. Subsequent tests were conducted in the reused mercury; however, there was little-to-no discoloration of the reused mercury.

The difference between the values obtained in mercury on both frames, when compared to values obtained in air or saltwater, speaks to the highly volatile interaction between aluminum and mercury. To accurately predict crack initiation and propagation, several tasks had to be completed prior to testing, including the coating of specimens. Without preparatory steps, specimen rupture could occur at any location, invalidating the test, potentially contaminating the mercury and only providing useful qualitative data. This proved to be one of the major difficulties during experimentation.

Analyzing the FEA study done prior to the coating of the specimens and comparing it to the experimental results revealed that stress within a body was just as important, if not more, to the fracture of specimens. Surfaces on the specimen that had a stress higher than the nominal stress experienced could provide favorable conditions for crack initiation. It is also suggested that the orientation of the specimens is favorable to crack initiation, as the number of grain boundaries in the direction perpendicular to crack growth is greater than any other orientation. All other orientations, e.g. S-T, L-T, T-L, etc., provide less grain boundaries available at the crack tip, therefore lowering the susceptibility. That is not to say that these orientations make Al

7075-T651 less susceptible to LME, just that the S-L orientation provides for a significantly lower resistance to fracture in the presence of liquid metals than the other orientations. Together, the aggressive attack by mercury, the favorable grain orientation and any increase in stress above the nominal stress provides substantial requirements for LME conditions to prevail and result in specimen failure.

#### 5.4.3 Microscopy of Fracture Specimens

Fracture surfaces of specimens fractured in liquid mercury displayed a much different failure mode than those fractured in air or saltwater. Significant features included burn markings, multiple layers of cracking and transgranular-like cleavage. Unlike previous specimens fractured in air or saltwater, no macroscopic plastic deformation in the form of shear lips was observed. This particular alloy exhibits about 11% elongation in uniaxial tension tests, signifying that the mercury had a significant effect on the ductility. Completely brittle-like failures were common throughout all specimens tested in liquid mercury, regardless of the load frame used.

Upon removing ruptured specimens from the environmental bath, several dark spots were noticed on the sides and fracture surfaces of samples. Specimen S-L-11 exhibited severe burn marks along the multiple crack initiation sites, as did others. The fracture surface itself included several dark regions, anywhere from 30-90% of the total surface of specimens fractured in liquid mercury. The discoloration is attributed the attack by liquid mercury by means of corrosion. Darker areas were observed to have several crack initiation sites, while areas of lighter or no discoloration appeared to behave normally.

Macroscopic cracks were visible along the starter notch and many existed throughout the thickness of the specimen. Some cracks were able to propagate through the width of the

specimen, resulting in aluminum flakes that were completely separated from the two severed halves, as in the case of S-L-11 and others. The flakes suffered the same discoloration as the rest of the fracture surface. Additionally, several specimens had cracks that originated along the starter notch that did not propagate through; however, some have fallen off the surface as a result of handling and placement in specimen bags.

Cracks were observed to occur at various locations along the starter notch. Provided the specimen orientation, approximately 45 grain boundaries were available in the S direction along the starter notch. No specific trends were observed in specimens that had crack initiation in locations other than the vertex of the starter notch. With this high concentration of grain boundaries along the notch, it provides evidence that LME could potentially be grain boundary-dependent and the orientation provides for multiple locations that provide favorable crack initiation conditions.

Fracture surfaces viewed under the digital microscope appeared to be far more damaged than those of specimens fractured in air or saltwater. Instead of having one flat plane of fracture, several plateaus and valleys were observed on surfaces of specimens fractured in liquid mercury. Particularly on S-L-30, a step of approximately 0.455 mm ( $17.5 \cdot 10^{-3}$  in) was observed along the side of the specimen. Shear lips were nonexistent, as these were replaced with decohesion of layers of aluminum.

Within each step, the surface appeared smoother but with much more jagged peaks and valleys than air and saltwater surfaces, as on S-L-26. Large transgranular cracks were observed on some specimens, like the one shown on S-L-11 in Fig. 4.14. Cleavage-like river markings were observed on mercury affected surfaces under the SEM. At the same scale as images taken on specimens fracture in air and saltwater, the surface appears to be mostly smooth, without the

peaks and valleys. Differentiation between the aluminum and any inclusion particles was difficult to establish, as the surface appeared uniform. Generally, there was a vast difference between the failure modes of specimens fractured in air, saltwater and liquid mercury.

### **5.5 Incubation Experiments in Liquid Mercury**

The majority of fracture experiments conducted in liquid mercury were incubation experiments. All of the incubation points were acquired using the servohydraulic load frame, readily allowing for comparison between data points. The results were grouped in either two groups and correlations between load and incubation time depended on a variety of factors.

#### 5.5.1 Incubation Loads

Specimens subjected to incubation experiments were pre-cracked in liquid mercury, unloaded then loaded to a predetermined load that would achieve an estimated initial stress intensity factor,  $K_{I0}$ . The load was held until the specimen ruptured or a preset time had elapsed, in which if failure did not occur, the specimen would then undergo a fracture test. The goal of these experiments was to provide a dependence of time to failure based on a given stress intensity factor.

Several initial  $K_{I0}$  values were chosen based upon the plane-strain fracture toughness value obtained in liquid mercury. Specimens were observed to fail immediately or after an extended period of time, without any failures in between the two groupings. Ultimately, a limit at which no fracture occurred in the presence of liquid mercury was sought after. This limit, the proposed LME Incubation Limit, was to be similar to the endurance limit of a material subjected to fatigue routines; however, the data did not readily support this theory, as more data at lower values  $K_{I0}$  is necessary.

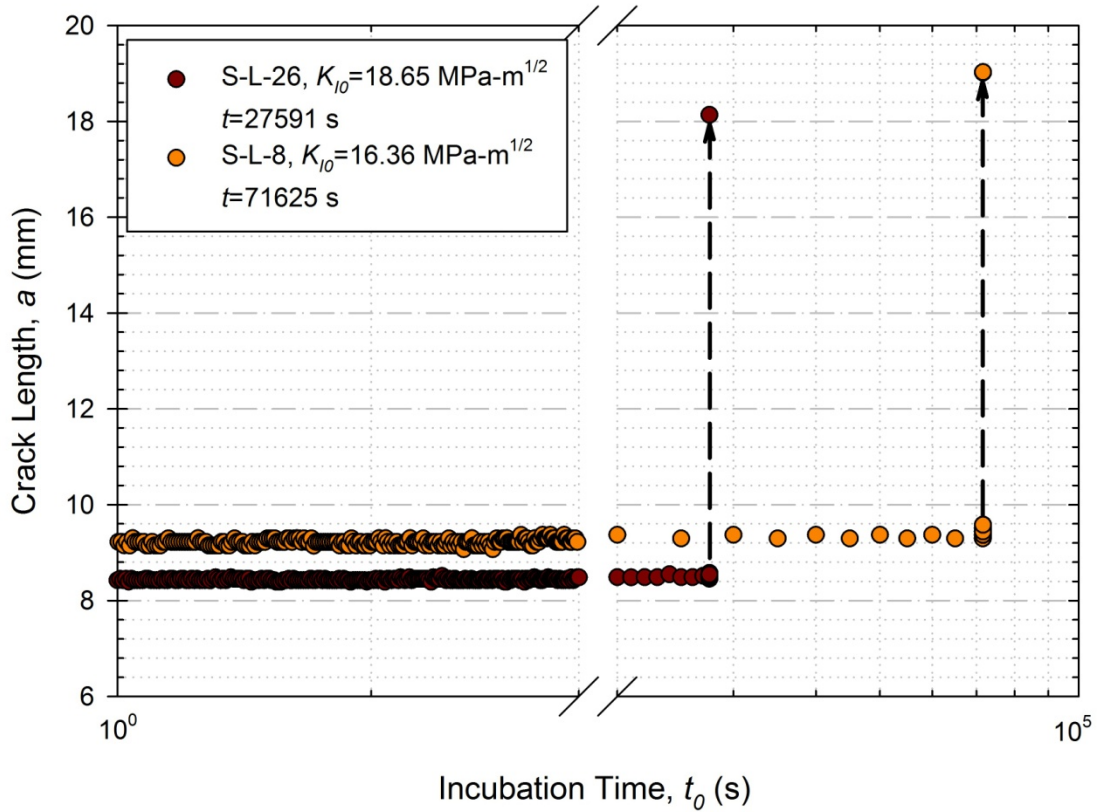


*Figure 5.2: Representative comparison between crack lengths when failure occurs.*

Specimen rupture was observed to be a random event that occurred rapidly. Stable crack growth was not observed, as specimens ruptured in less than 0.1 seconds, Fig. 5.2. Shown are two crack lengths as a function of time for two specimens, but all specimens fit this trend. Crack growth was unable to be captured, as it was out of the acquisition rate of the software (10 Hz). Essentially, crack initiation occurred at a favorable location within the specimen and crack propagation occurred rapidly.

As previously mentioned, the data lends to a different dependency than initially thought. The focus was to establish a dependency on the applied SIF; however, it appears that a critical stress, microstructural orientation or a combination of the two is the more dominant factor in regards to crack initiation and propagation. If proper wetting occurs at the surface of a stressed region, this region can generate a crack that is free to propagate. This was the case of S-L-12,

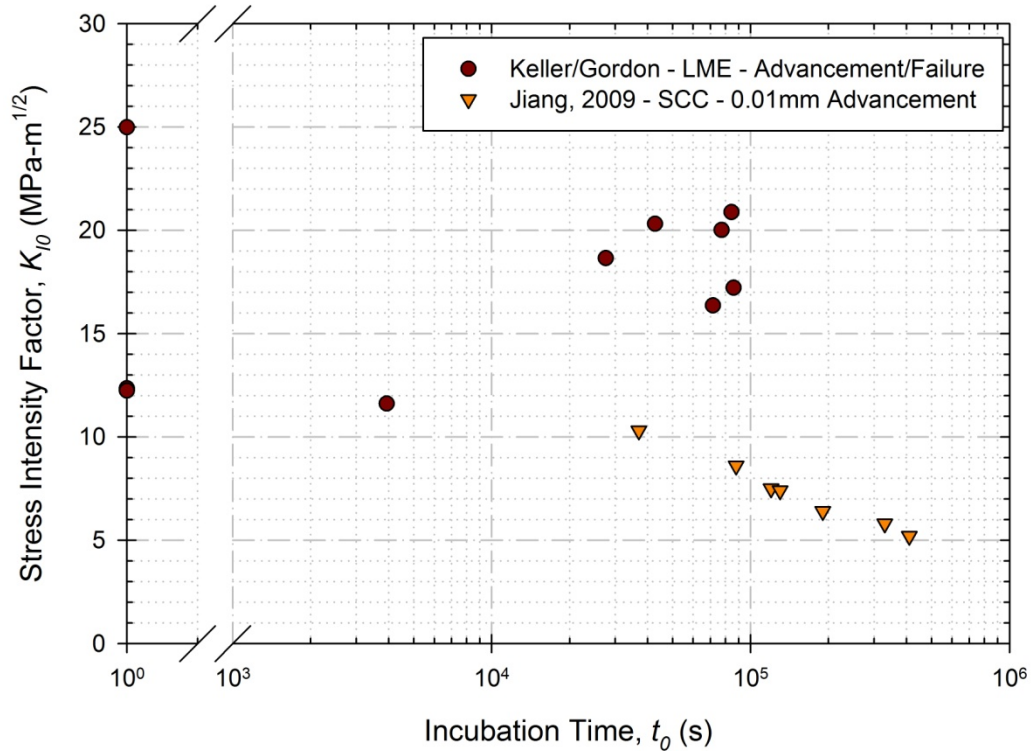


**Figure 5.3:** Comparison of incubation times for S-L Al 7075-T651 specimens in liquid environments.

which failed at a load of 1.92 kN (433 lbf) on the second cycle during pre-cracking. Crack initiation and propagation occurred at the desired location of the starter notch; however, it occurred extremely pre-mature when compared to other data points. A crack was not present at this location, but there was a critical stress present and favorable LME conditions were present.

The pre-mature rupture of S-L-12 and S-L-29, along with the failures through the load pin hole and knife edge valley further support the claim that a critical stress is more dominant in the determination of failure location. If a critical stress is achieved, and liquid metal is readily available to wet any newly created surfaces, rupture can occur. Coupled with the extremely high crack tip velocities observed in this study and literature, any highly stressed region exposed to liquid mercury could be a potential location of catastrophic failure. In the event that wetting occurs, rupture can be expected to occur and for the failure to be almost instantaneous.

Comparisons between SCC and LME for S-L oriented specimens of Al 7075-T651 can be made, Fig. 5.3. The data for experiments conducted in 3.5% NaCl were on plane-stress specimens and the time noted is for 0.01 mm ( $3.9 \cdot 10^{-4}$  in) crack advancement. Compared to the data from this study, a much more consistent relationship between incubation time and  $K_{I0}$  is observed for submersion in saltwater. For crack lengths to propagate to the length of those conducted in liquid mercury, approximately one order of magnitude more time was required to pass.

Through the incubation experiments, it was observed that a critical stress, as opposed to a critical stress intensity factor may be more of an influence on crack initiation and propagation. Instead of a LME Incubation Limit based on initially applied  $K_I$  values, it would be more appropriate to determine a critical stress at which crack initiation occurs. Additionally, by implementing various orientations of the test specimen, e.g. S-T, T-L, L-T, etc., a grain boundary-dependence on crack initiation could be investigated. Critically stressed regions with favorable grain boundary orientations could be observed through FEA and components could be redesigned to dramatically reduce any areas of concentrated stresses. It was observed that regardless if a crack was present or not, a region with concentrated stress, and possibly a critical orientation of the microstructure could have a more influence on specimen rupture.

### 5.5.2 Microscopy of Fracture Specimens

Both digital and scanning electron microscopy was conducted on specimens incubated in liquid mercury. Results were similar to that of specimens that underwent plane-strain fracture toughness tests in liquid mercury.

Specimens exhibited similar burn markings to the specimens used in the plane-strain fracture toughness tests. Dark regions with several crack initiation sites were present, which

denoted a strong reaction between the aluminum and mercury. All experiments displayed these burn marks, as the time the aluminum was exposed to the mercury was significant in comparison to fracture toughness test specimens. A comparison between fracture surfaces, at the macroscopic level, is given in Fig. 5.4.

The specimens fractured in static laboratory air and 3.5% NaCl displayed similar fracture surfaces. Overall, the appearances of the two were very similar, with the only difference being the corrosion due to immersion in saltwater. The fast fracture surface of the two specimens were relatively flat, contained only one plane and exhibited shear lips. Environmental effects were not as apparent on the fracture surface as compared to tests conducted in liquid mercury.

The remaining seven specimens all fractured in a liquid mercury environment. Plane-strain fracture tests were attempted on S-L-11, S-L-6, S-L-19 and S-L-21, resulting in three invalid tests. Specimen S-L-11 fractured in the desired manner while the others premature ruptured during the pre-cracking routine. The fracture surface of S-L-11 is multi-planar, with several crack initiation sites along the starter notch. Fracture surfaces of S-L-6, S-L-19 and S-L-21 are mostly a single plane, with limited decohesion of layers at the crack initiation location.

Crack initiation sites are typically the most discolored portion of the fracture surface. Specimens exhibit burn marks burn marks and decohesion down the width of the specimen. Several planes are seen to be delaminated with the thickness of these planes the approximate thickness of a grain within the aluminum. With several of these separations occurring along the crack initiation site, there is strong evidence that a favorable grain boundary orientation will provide for a crack initiation site.

Fracture specimens subjected to incubation experiments exhibited a similar behavior to S-L-11. Several steps and planes were observed in the fast fracture portion of the specimen.

Burn markings were present, as well as several crack initiation sites. Surfaces were 30-90% discolored, providing evidence for a strong chemical reaction. Overall, the fracture surfaces were extremely volatile and the fractures occurred rapidly and violently.

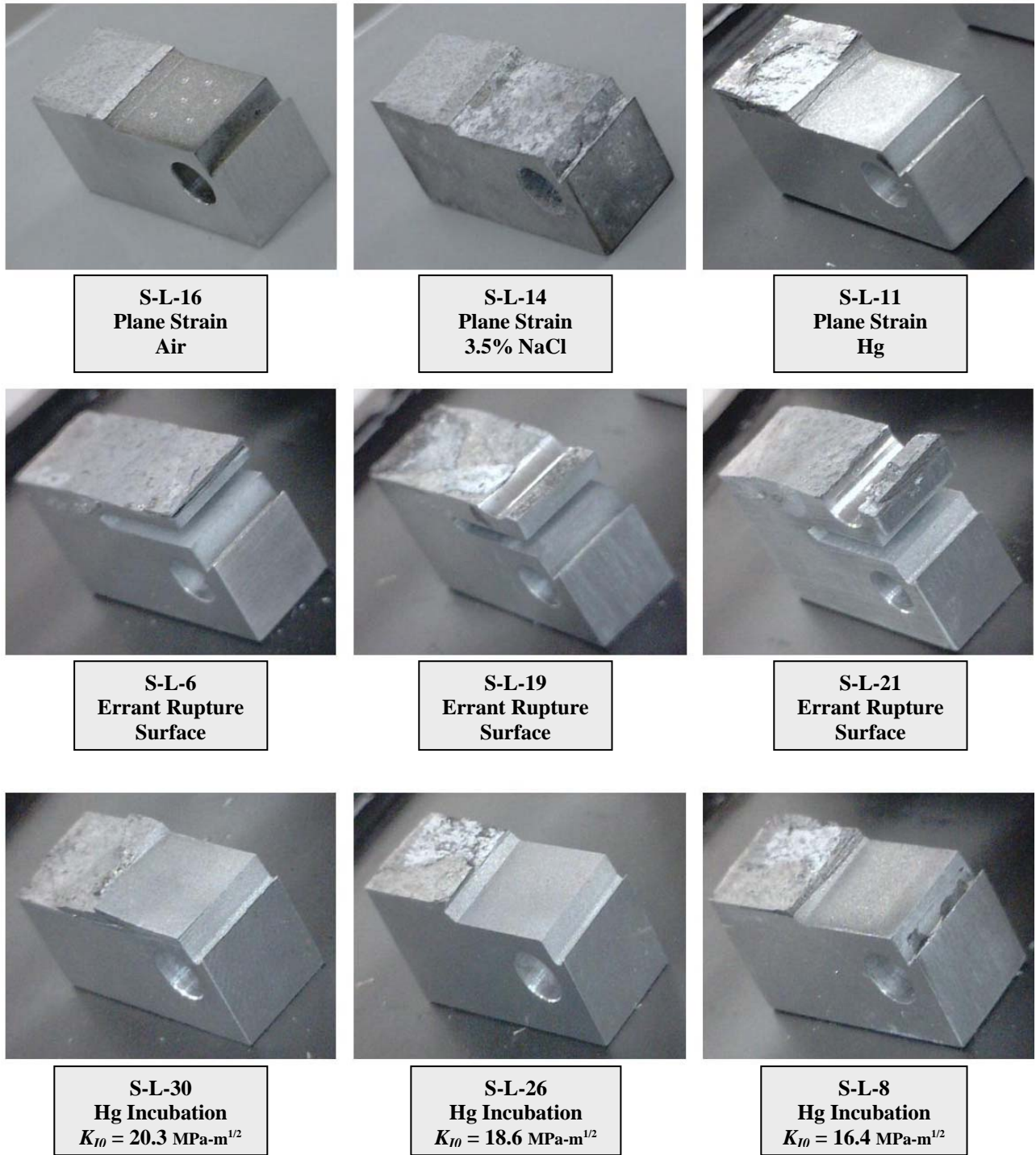


*Figure 5.4: Overview of fracture surfaces at the macroscopic level.*

Scanning electron imagery provided similar results to specimens fractured in plane-strain routines. Relatively flat portions were observed, with cleavage-like river markings. The surfaces were much darker than those of surfaces of specimens fracture in air and saltwater. Essentially, all specimens fractured in liquid mercury resembled all other specimens fracture in liquid mercury, regardless of test routine or incubation stress intensity.

Finally, EDX was utilized in analyzing the surface of fracture specimens in air and liquid mercury. The goal of this analysis was to determine the effect that alloying components had on the fracture of specimens. Comparing the full scale counts on specimens S-L-16 (fracture in air) and S-L-11 (fracture in mercury), nearly identical peaks were observed, with the exception of the peak for mercury in S-L-11, Fig. 5.5 and 5.6. Trace amounts, in the form of small peaks, of Tantalum and Titanium are observed in S-L-16, while they are nonexistent or were not detected on S-L-11. Through this observation, it could be that these alloying elements are active in the fracture of a specimen in air, but does not aide in resisting fracture in liquid metal environments.

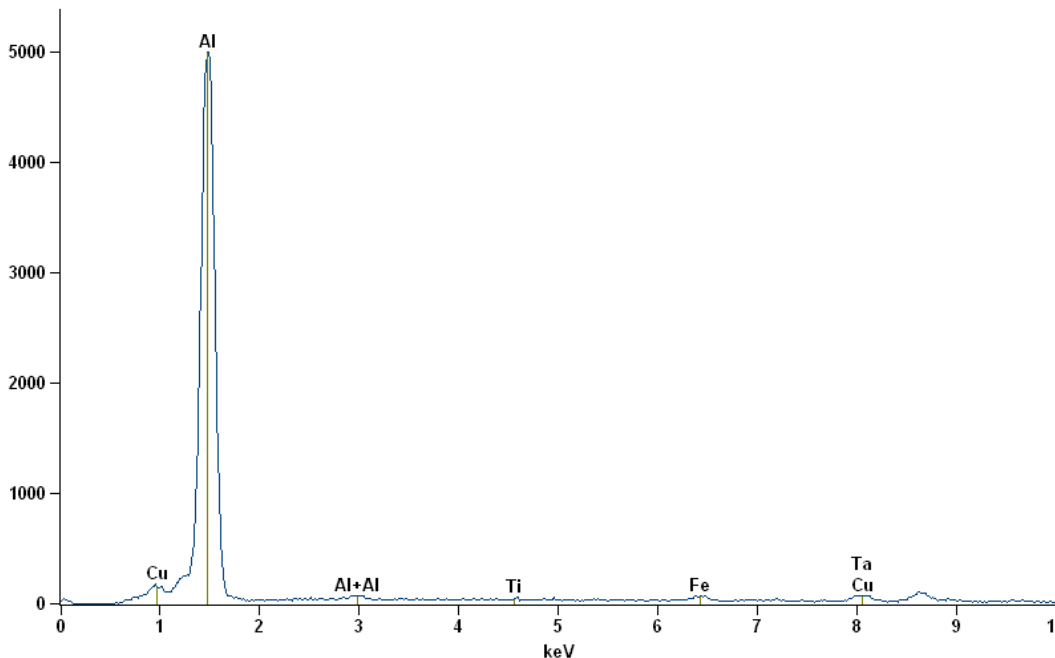


*Figure 5.5: Full scale count graph from EDX analysis on a fracture specimen fractured in air (S-L-16).*

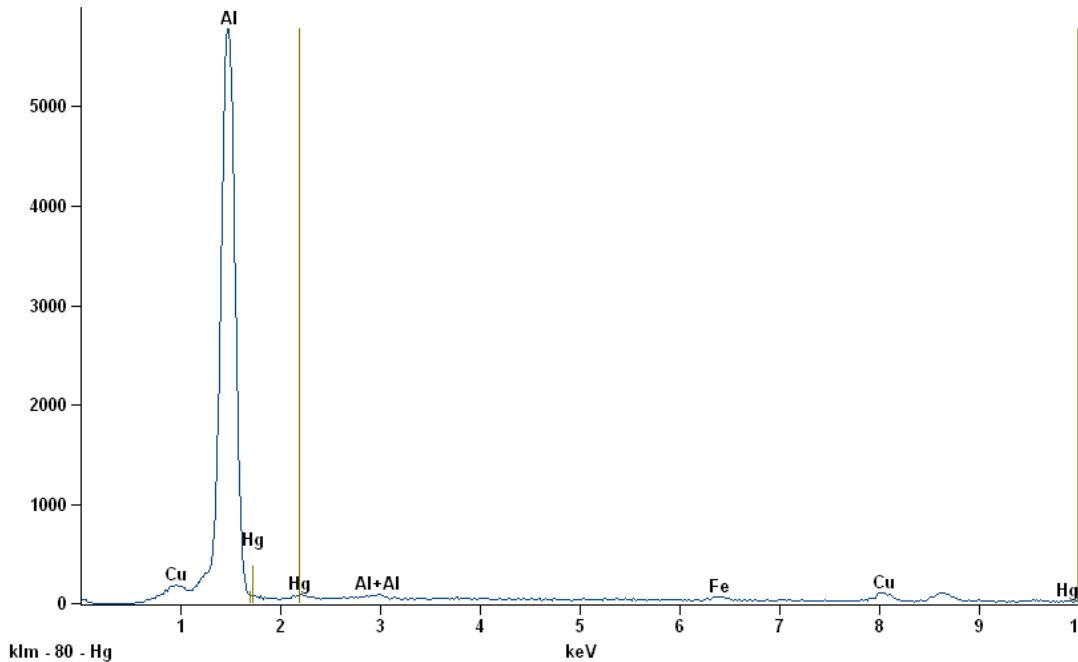


**Figure 5.6:** Full scale count graph from EDX analysis on a fracture specimen fractured in liquid mercury (S-L-11).

The results from this study have particular implications in regards to the microstructural failure mechanisms discussed in Section 2.4.1. It was observed that the failure of specimens, whether during the fatigue pre-cracking routine or after an extended period of time incubating, was dependent on a variety of factors. Ultimately, the rupture of specimens was both load- and microstructural orientation-based. A critical stress coupled with a favorable microstructural orientation can provide the necessary conditions for crack initiation and propagation. None of the theories account for this dependency.

Both the Stress Assisted Dissolution Model (Robertson, 1966 and Glickman, 1977) and the Grain Boundary Diffusion Model (Krishtal, et al. 1973) were not observed to contribute to the results obtained in this study. The Stress Assisted Dissolution Model, which states that the liquid is merely a transport for the solid metal atoms, was not applicable for this couple, as the solubility of the aluminum in liquid mercury is negligible. The Grain Boundary Diffusion Model, where the fracture of specimens occurs along grain boundaries, is not valid as both

previous and current research provides evidence of transgranular fracture. Significant intergranular fracture was observed in specimens fractured in liquid Hg; however, on several surfaces river marks, which are a form of cleavage and transgranular fracture, were observed. For the Al-Hg couple, these two theories do not lend much support to the failure of specimens submerged in a liquid metal.

The remaining two theories, the Decohesion Model (Stoloff and Johnston, 1963 and Westwood and Kamdar, 1963) and the Adsorption Induced Dislocation Emission Model (Lynch, 1977), seem to account for failures observed in the Al-Hg couple. On the fast fracture surface of S-L-11, regions of localized plastic deformation (in favor of the AIDE Model) and regions of no ductile failure (in favor of the Decohesion Model) were observed. Both of the theories applied to different portions of the fast fracture surface and a combination of the two could be attributed to a dependency that was not included in either model.

The dependency on load and the microstructural orientation could provide for this combination of failures. Provided a favorable microstructural orientation, cracks could initiate and propagate in a manner that favors microvoid coalescence and localized regions of plasticity. Likewise, if a different orientation is provided, possibly in which several inclusion particles are located, very brittle fractures could be observed without any significant flow of material. Inclusion particles were observed to fail in a transgranular fashion; therefore, if an abundance of these inclusions are concentrated at the surface, it is likely that cracks could initiate and propagate with no plastic deformation would occur. Coupled with a critical stress, a combination of the two theories could be applicable.

Crack initiation is the major component missing from the failure theories provided. All of the theories study the effect of liquid metals on the propagation of existing cracks. It can be

argued that the more important aspect to this research is in the study of a critical stress and a critical and/or favorable microstructural orientation. Understanding why a crack will initiate in the presence of liquid metal will provide engineers valuable information when designing components to resist EAC. In the presence of liquid metals, crack velocities are known to be extremely high, on the order of centimeters per second and higher; therefore, failure can be expected once a crack is initiated. It is the suggestion that more information regarding a critical stress and microstructural orientation favoring crack initiation be investigated to further extend the microstructural failure mechanisms of LME.

## CHAPTER 6 CONCLUSIONS

Environmentally-assisted cracking has long been a negative phenomena in the realm of engineering components used in corrosive environments. Stress corrosion cracking (SCC), corrosion fatigue (CF) and liquid metal embrittlement (LME) have all been deemed the root of a catastrophic failure of components in service. The effects are devastating, with the loss of life a very real possibility. Understanding the underlying microstructural failure mechanisms will allow for designers and engineers to properly account for environmental effects. Components capable of resisting environmentally-assisted cracking will result in safer working conditions and extended service lives.

The high strength aluminum alloy, Al 7075-T651, has shown its susceptibility to both SCC and LME. In particular, crack growth rates in aluminum intimately exposed to a liquid metal environment have been shown to have crack velocities on the order of centimeters per second. The transferability of LME, namely when mercury is the liquid metal, can be extended to hydrogen embrittlement (HE); a very real concern in all materials and materials processes. Methods have been developed to study the effects of LME and HE, but recent interest in both have generated the need for new methods to be developed.

As a result of the observations made during the course of this thesis, several achievements have been made:

- A novel method of subjecting fracture mechanics specimens to liquid environments has been developed. An environmental chamber capable of housing both liquids at room temperature and fracture specimens was utilized in a variety of experiments in an effort to characterize the effects of LME on a high strength aluminum alloy. The chamber

provided the necessary requirements to continually supply a liquid to newly created fracture surfaces without interference from the surrounding environment. By doing so, this method eliminated competition between oxidation and LME at the crack tip; however, any oxides contained within the mercury were not accounted for. Future studies can be conducted utilizing the current experimental configuration that makes use of solid-liquid metal couples that do not readily oxidize to further investigations in SCC and LME.

- Experimental routines were developed and implemented in determining the reliance of stress intensity factors on the time to failure of a test specimen. Fatigue pre-crack routines were successfully conducted in liquid metal environments, providing for an initial stress intensity factor to be applied to the specimen. Either plane-strain fracture toughness or incubation experiments were then conducted. To achieve an incubation experiment, a constant load was applied that resulted in a known  $K_{I0}$  to the specimens submerged in liquid environments. Additionally, these delayed failure tests were able to be conducted without extensometers, which can allow for the testing of a variety of solid-liquid couples.
- Mechanisms leading to failure were observed to be a result of an externally applied load and favorable microstructural orientation. Once a critical stress was achieved at a location with a potentially critical microstructural orientation, cracks can be expected to initiate and propagate. Failures were more dependent on crack initiation, as no significant amount of subcritical crack growth was observed. Specimens failed immediately at the onset of propagation, therefore the initiation conditions are more dominant in the role of rupture of specimens in liquid metal.

- Suggestions regarding the current microstructural failure mechanisms have been made; primarily that there exists a load dependence on the effects of liquid metal embrittlement. None of the proposed theories of liquid metal embrittlement account for a load or microstructure affect. It was observed that under the presence of a critical stress at a location of favorable crack initiation, rupture of specimens would occur. Given this information, theories need to be amended to include:
  - A Critical Stress – a critical stress at a location can lead to crack initiation and propagation. This was observed through multiple crack initiation locations along the highly stressed starter notch; therefore, some information regarding a critical stress is necessary.
  - A Critical/Non-Critical Microstructural Orientation – ruptures occurred at various locations on the specimen, which leads to a microstructural orientation-based dependency. If the grains within a material are aligned in a critical/non-critical fashion, the resistance to crack initiation and fast fracture could be approximated. Even if the affect of the orientation is that designs should avoid using components machined in particular orientations, it is a worthwhile observation.

## **CHAPTER 7 FUTURE WORK**

Identifying the underlying microstructural failure mechanism(s) of a structural solid metal in the presence of LME conditions cannot be limited to one solid-liquid couple nor to one type of mechanical test configuration. Varying service and exposure conditions require different experimental configurations (e.g. test type, specimen type) in order to isolate different mechanisms. As shown, several different experimental techniques have been implemented to study the effects of LME on several metal couples. Presented in this thesis is just one technique utilizing one particular solid-liquid couple. It is the recommendation of the author that additional experiments be conducted.

### **7.1 Motivation**

The motivation behind continuing this research, in terms of additional material choices and experimental routines, is to isolate other factors influencing in incubation and failure times. The research provided has shown that a dependence on load does exist. When a crack is present in a mechanically loaded member that is in intimate contact with a liquid metal, the crack can propagate freely at a very high rate. If two or more cracks are present, any of them are free to propagate if the conditions for LME are satisfied. This rupture event has been shown to be somewhat sporadic; therefore, making predictions of failure locations, based upon cracks and SIFs, difficult.

With the knowledge that any crack within a loaded member is capable of propagating, crack initiation studies would provide useful data to the engineer. By establishing a critical stress or strain level that promotes crack initiation, catastrophic failures could be avoided by maintaining a stress or strain well below this critical threshold. Utilizing a variety of material

couples, experiments can be developed that impose a known stress or strain on a smooth surface (such as a polished notch in a specimen). Implementing such a routine at various stress or strain values can help to establish a critical stress or strain level where crack initiation can be expected to occur, signaling to the engineer that repair or replacement of that member must occur. It is suggested that this method would be more beneficial and practical for components in service.

## **7.2 Additional Solid-Liquid Couples**

The solid-liquid couple utilized as a part of this study was chosen because of the properties of the liquid metal, Hg, and widespread use of the solid metal as a structural member, Al 7075-T651. Mercury is liquid at room temperature, allowing for tests to be conducted at room temperature and eliminates any temperature effects associated with using a metal that requires heat to become liquid. Additionally, liquid Hg does not oxide as quickly as other liquid metals at room temperature. The behavior of this couple may not be identical to other couples and other low eutectic alloys can be utilized.

Gallium and Indium are both low melting point metals that require a relatively low temperature environment to become liquid. Gallium has a melting point of approximately 29.7°C (85.6°F) and is commonly a liquid in laboratories. Indium requires a higher temperature, approximately 157°C (314°F), in order to become a liquid. Gallium is known to readily diffuse into grain boundaries without stress applied (Benson and Hoagland, 1989). The stress-free diffusion could potentially affect the embrittlement and susceptibility of aluminum to LME.

Other eutectics that melt at relatively low temperatures, 70.0° C (158° F) or below, can be used that do not readily penetrate the grain boundaries of aluminum. A Bi-Pb-In-Sn-Cd eutectic has been used and shown to have similar results to that of mercury and gallium, but without the negative associations inherent with either mercury or gallium (Lynch, 1977).

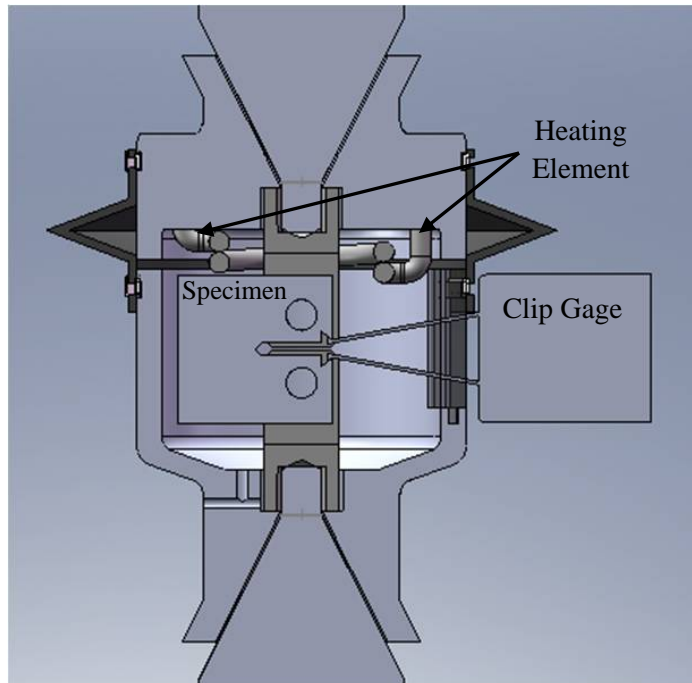


**Figure 7.1:** Modified experimental chamber with clip gage and heating element additions.

To facilitate the testing of future C(T) specimens in liquid metal environments, an updated environmental chamber has been designed and is currently in the manufacturing process, Fig. 7.1. This chamber is similar to the initial design; however, it has been modified to allow for the use of a clip gage and has incorporated a heating element to ensure that a liquid environment is present throughout the duration of experiments. With this new design, a variety of low eutectic alloys can be used as the liquid embrittler.

It is suggested that more couples be investigated to develop a more inclusive microstructural failure model that incorporates a wide variety of solid-liquid couples. Although one couple may not exhibit the same behavior as another, testing a variety of couples in a similar experimental fashion may yield more conclusive results.

### 7.3 Crack Initiation Studies

During the course of the experimental portion of this research, specimens ruptured away from the desired location. Prior to the application of rubberized coatings to specimens, cracks were observed to initiate at several locations, which resulted in total rupture of the specimen. Upon implementing the rubberized coating, premature failures continued to occur at the starter notch even in the absence of a fatigue pre-crack, as in the case of S-L-12. This leads to the belief that crack initiation is of extreme importance and that the SIF may not be as important as a critical stress or strain level.

#### 7.3.1 Stress Concentration Dependency

The development of a stress intensity factor dependence on the incubation time is important when structural members have existing cracks, but is not applicable when a crack does not exist. In the case of a C(T) specimen without a fatigue pre-crack, a stress concentration,  $K_t$ , is present. Additional locations on the C(T) specimen also provide for a stress concentration, such as load pin hole, which have the possibility of becoming a crack initiation location. A rough surface, such as the EDM surfaces, can also present a favorable site for crack initiation. With multiple locations for possible crack initiation, critical stress or strain value may have more of an active role in initiation and propagation of cracks in the presence of an embrittling substance, such as saltwater or liquid mercury.

It is suggested that a modified set of experiments be explored, including one capable of incorporating a modified specimen and environmental chamber. This setup should include proper methods of submersing the crack tip, applying a mechanical load and a method of applying an embrittler to a sole stress concentration. One method to be investigated employs the

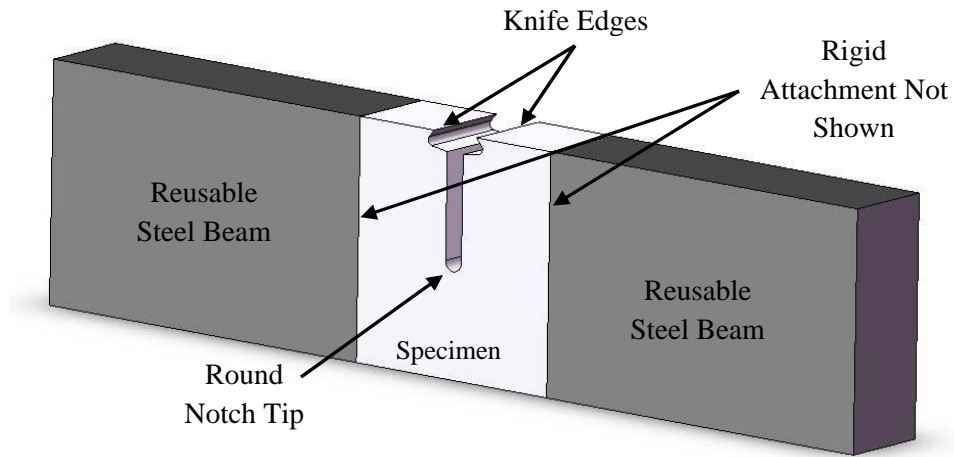


**Figure 7.2:** Sketch of modified C(T) specimen to be used in 4-pt bending experiments.

use of a 4-point bending apparatus and a modified C(T) specimen. A further explanation of the setup is provided in the following section.

### 7.3.2 Bending Experimental Setup

The stress concentration at a location within a structural member may play as an important role, or greater, as the SIF that exists within a cracked member. To investigate the level of importance of a critical stress or strain at a location, a 4-point bend setup can be utilized.

Keeping the specimen aligned in the S-L direction, new bend specimens can be machined that incorporates various round notches for varying stress concentrations. Dimensions will be somewhat identical to the C(T) specimen with the addition of a stiff material rigidly mounted to each end to allow for bending experiments and a round notch to provide a pre-determined stress concentration, Fig. 7.2. The advantage of adding material to the top and bottom of the C(T) specimen is that it will ensure that the specimen remains oriented in the S-L orientation and does not waste material by having to machine specimens out of a thick plate with an approximate thickness greater than 15 cm (6 in). Cracks will be able to propagate freely, with the desired crack plane similar to the plane observed in C(T) specimens.

An environmental chamber to house liquid metals is currently under development to submerge the round starter notch during experimentation. The chamber will incorporate a feature, similar to the one in Fig. 7.1, to allow for the use of a clip gage during testing. Similar to the C(T) specimens, the bend specimen incorporates knife edges for the measurement of the CMOD. Ideally, this configuration will allow for less liquid to be used, but also will promote better wetting of the crack tip throughout the test.

Although the loading method has changed, a similar compliance technique can be derived for this specimen, enabling crack length approximations to be made during experimentation. The derivation will be dependent upon the radius of the round notch present in the specimen; therefore, several versions will be derived allowing for a wide range of stress concentrations to be tested.

By loading the specimen through a 4-point bend, a uniform force can be applied to the specimen. Through various machining techniques, notches within the specimen can provide diverse stress concentrations, allowing for a more accurate determination of a critical stress, Fig 7.3. By observing the time to crack initiation, or complete failure, it is planned that a more conclusive argument for the incubation dependency on an externally applied load can be developed and provide insight on the crack initiation process as well.

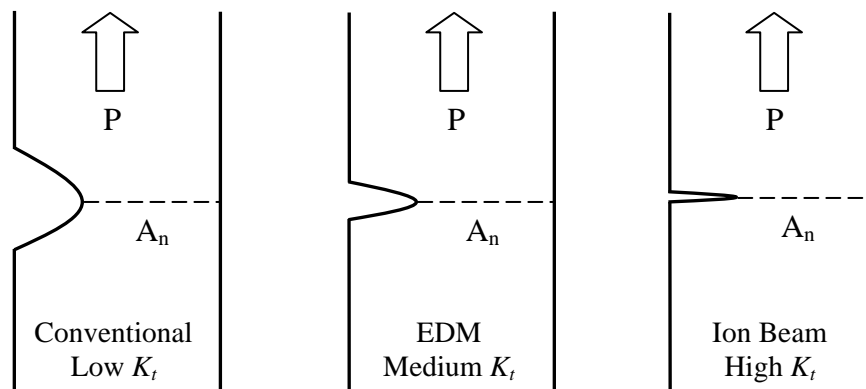
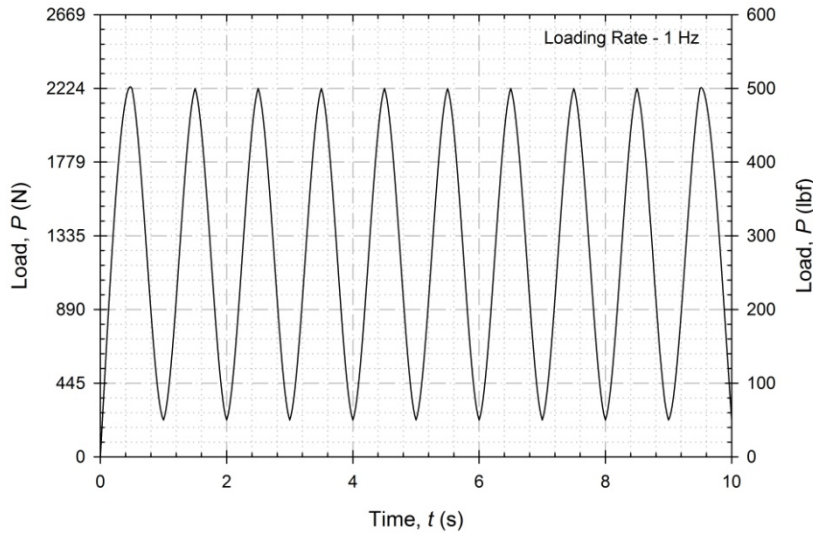


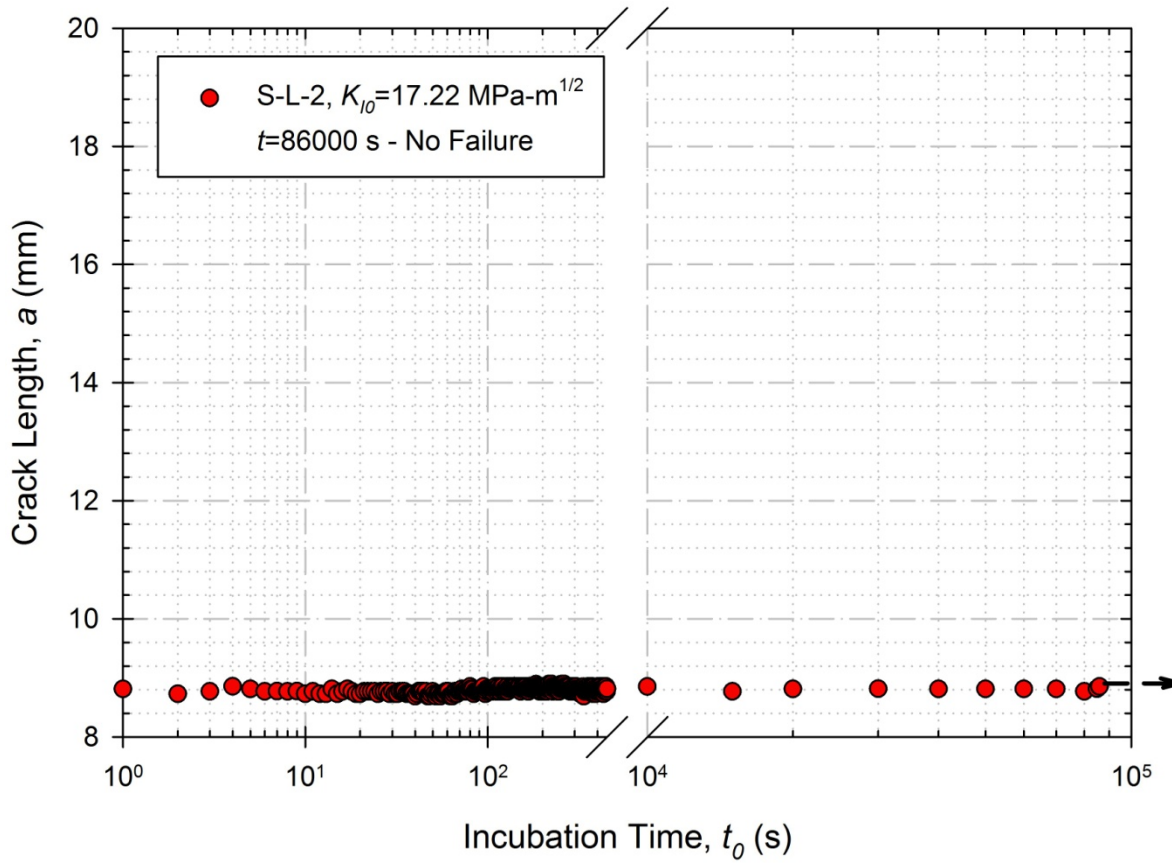
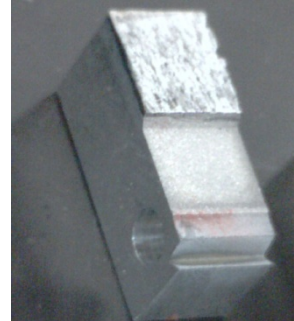
**Figure 7.3:** Machining techniques used to manufacture specimens with various notch radii and identical nominal stresses.

**APPENDIX A**  
**INCUBATION SPECIMEN DATA**

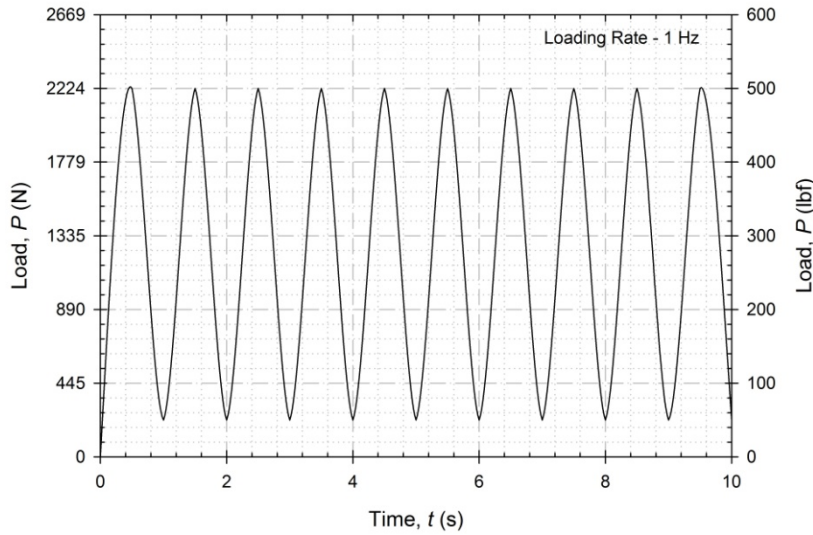
Fatigue Pre-Crack  
1800 Cycles



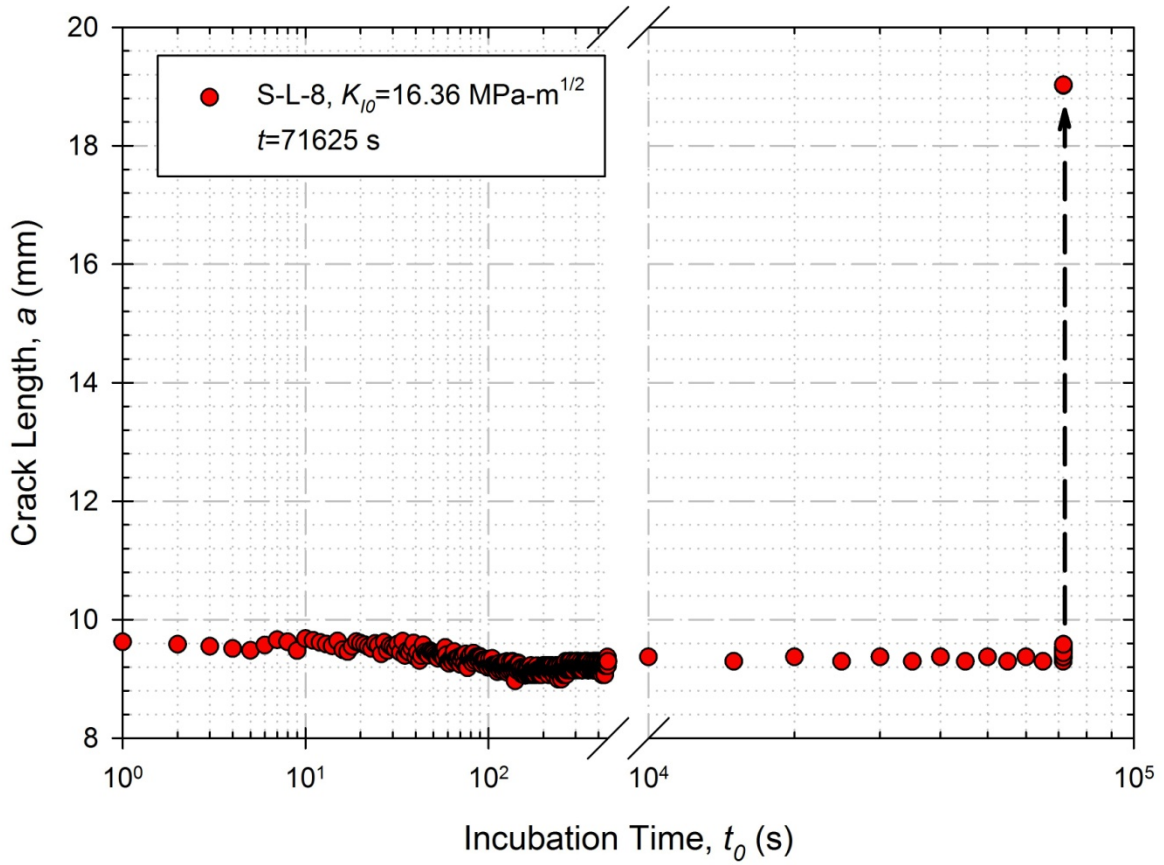
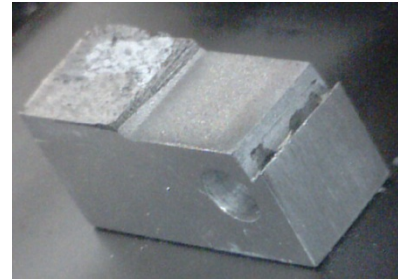
**S-L-2**  
 Environment: Liquid Hg  
 $K_{I0} = 17.22 \text{ MPa}\cdot\text{m}^{1/2}$   
 (15.67 ksi-in<sup>1/2</sup>)  
 Result: Test Stopped



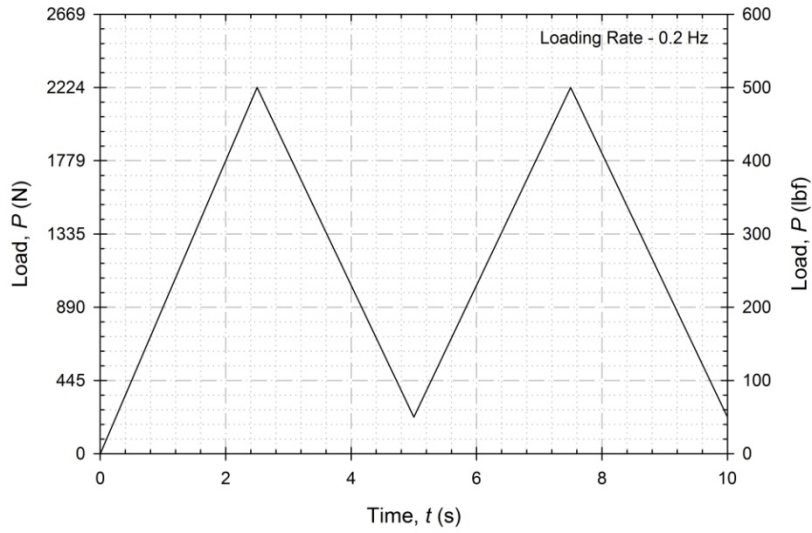
Fatigue Pre-Crack  
1800 Cycles



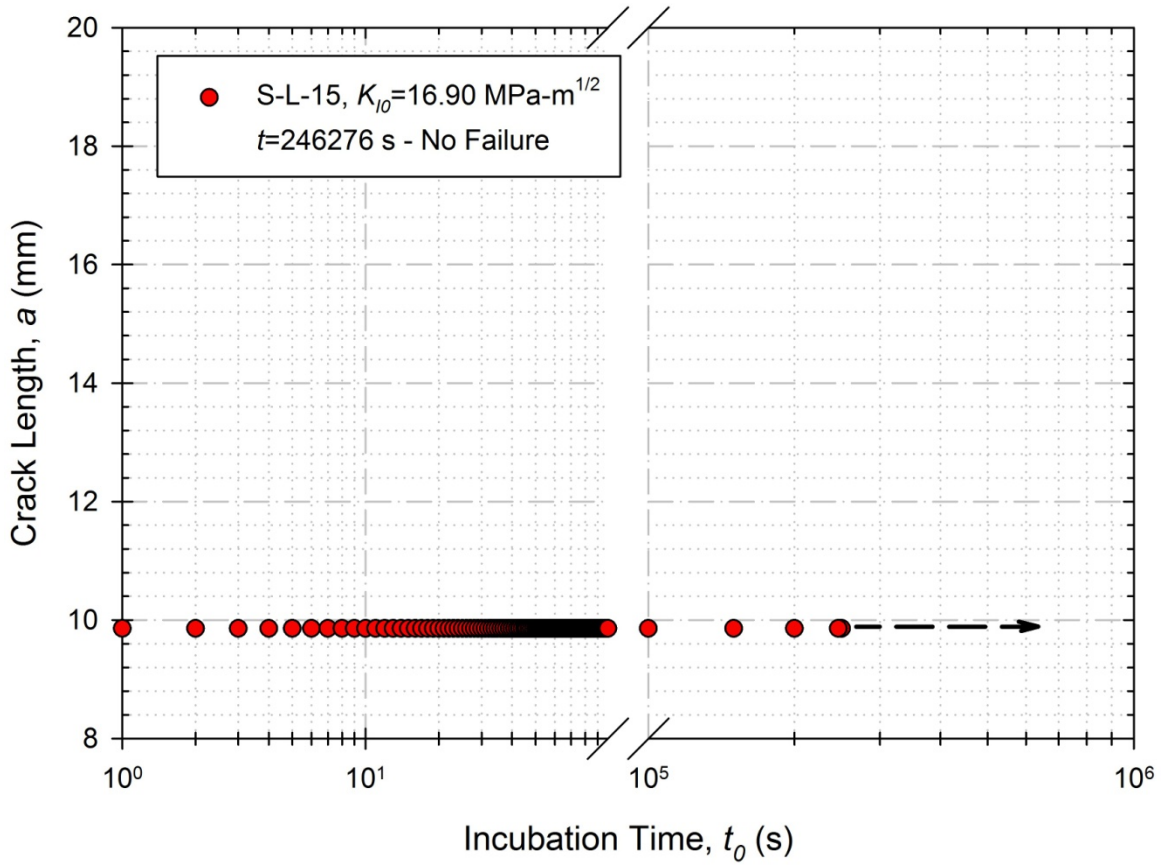
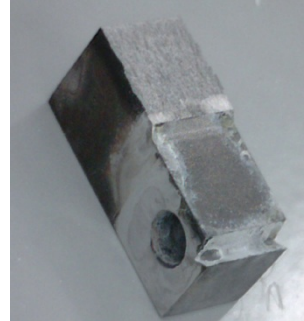
**S-L-8**  
Environment: Liquid Hg  
 $K_{I0} = 16.36 \text{ MPa}\cdot\text{m}^{1/2}$   
(14.89 ksi-in<sup>1/2</sup>)  
Result: Successful  
Incubation



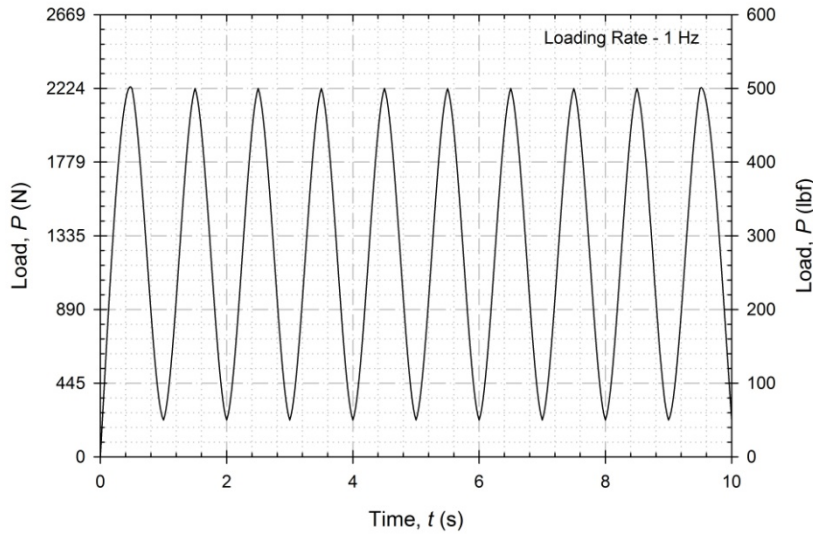
Fatigue Pre-Crack  
1680 Cycles



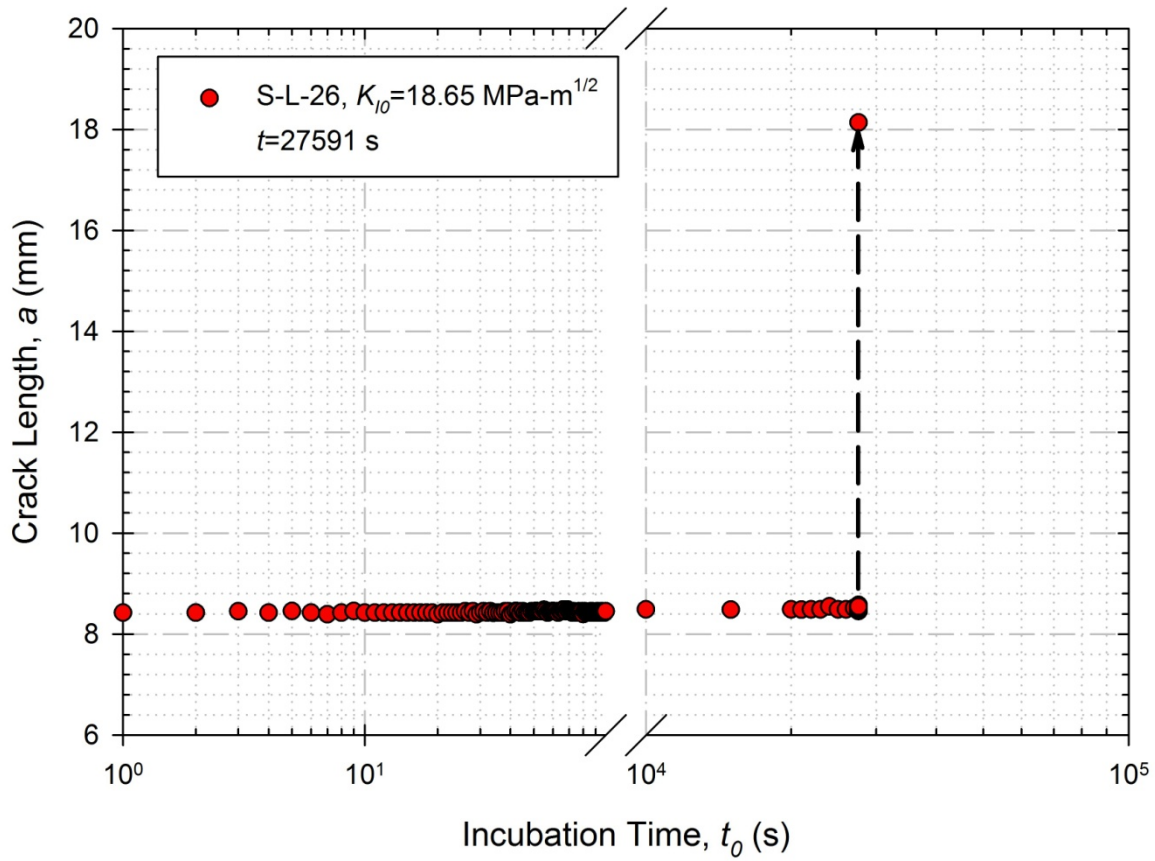
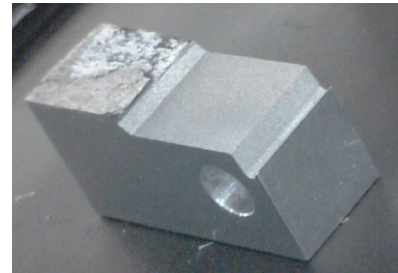
**S-L-15**  
 Environment: 3.5% NaCL  
 $K_{I0} = 16.90 \text{ MPa}\cdot\text{m}^{1/2}$   
 (15.50 ksi-in<sup>1/2</sup>)  
 Result: Test Stopped



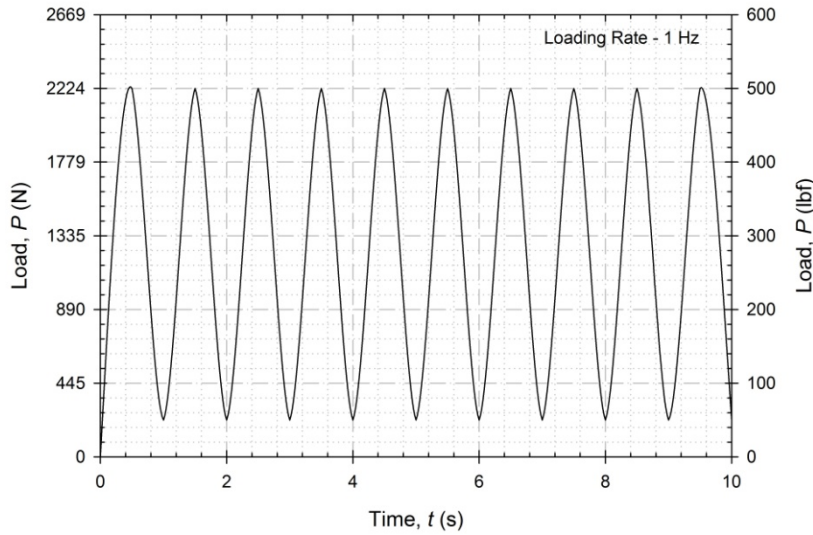
Fatigue Pre-Crack  
1900 Cycles



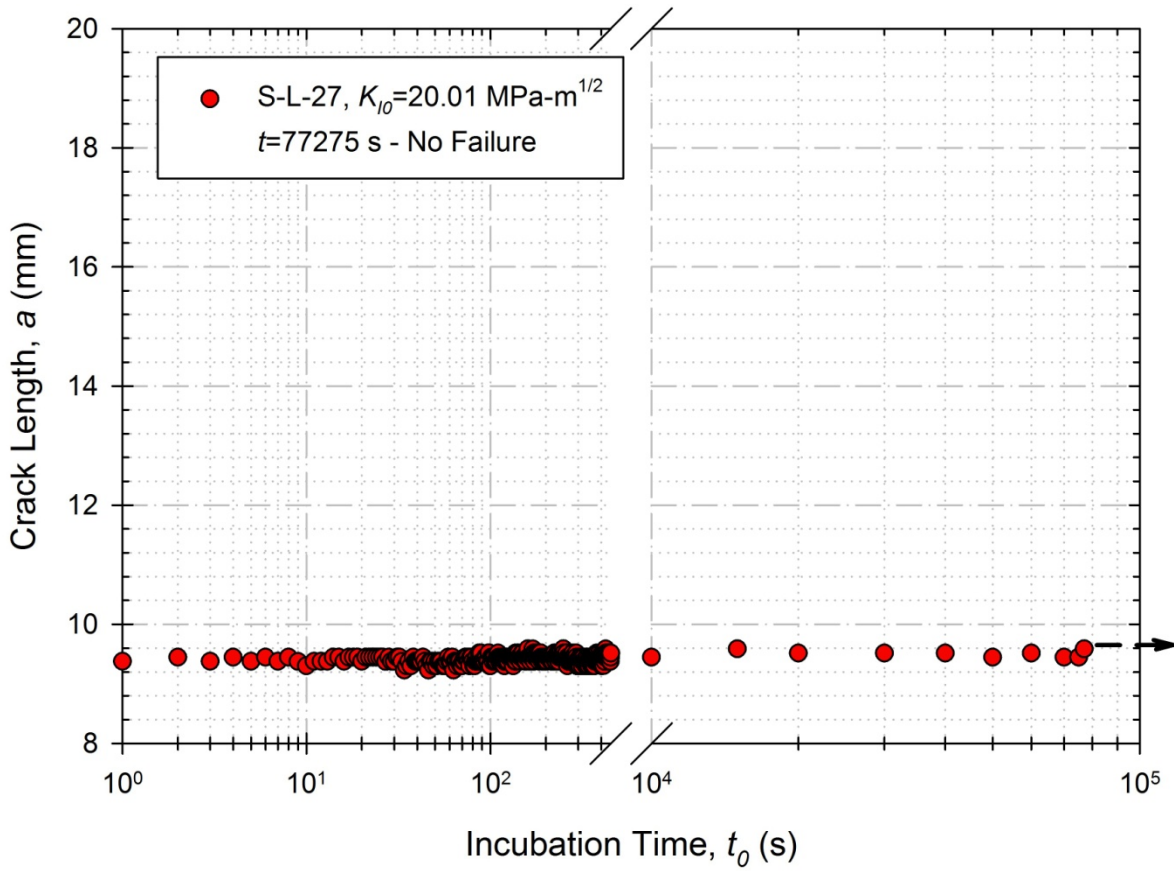
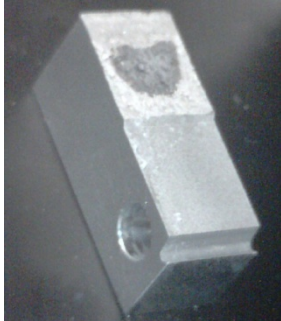
**S-L-26**  
 Environment: Liquid Hg  
 $K_{I0} = 18.65 \text{ MPa}\cdot\text{m}^{1/2}$   
 (16.98 ksi-in $^{1/2}$ )  
 Result: Successful  
 Incubation



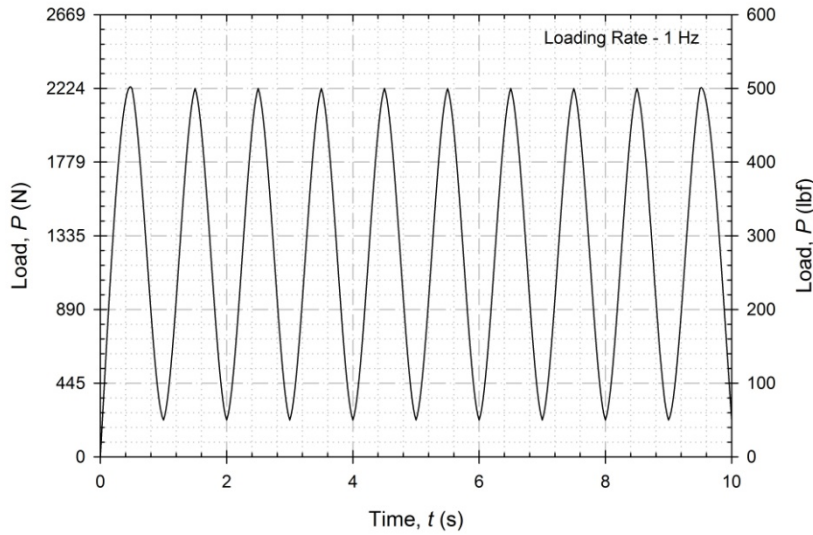
Fatigue Pre-Crack  
1900 Cycles



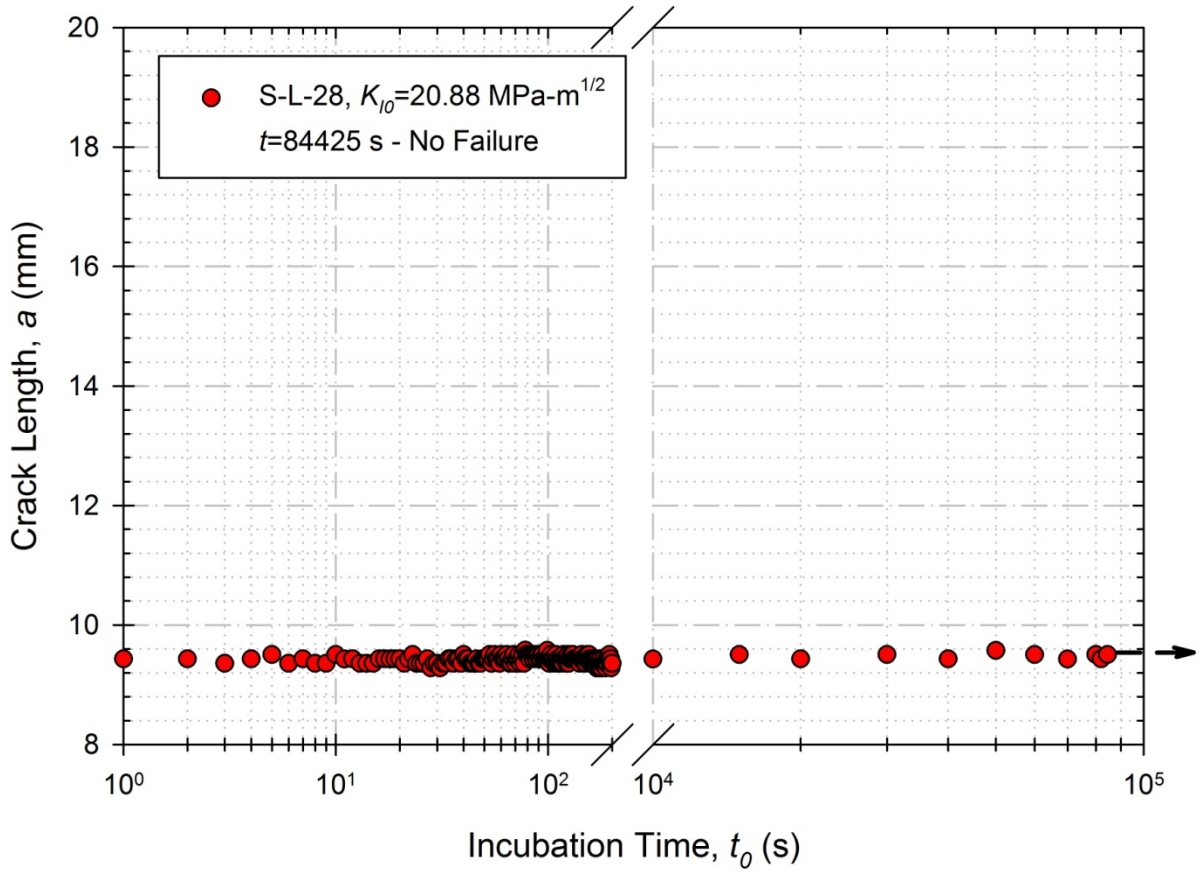
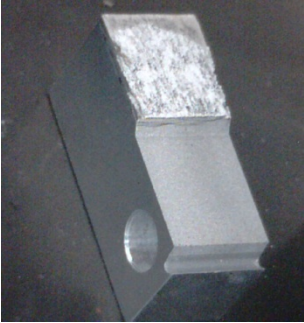
**S-L-27**  
 Environment: Liquid Hg  
 $K_{I0} = 20.01 \text{ MPa}\cdot\text{m}^{1/2}$   
 (18.28 ksi-in<sup>1/2</sup>)  
 Result: Test Stopped



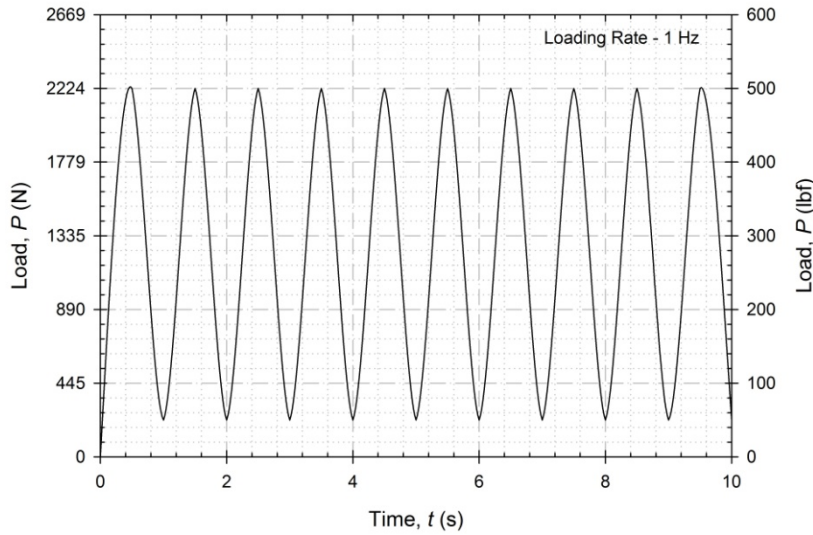
Fatigue Pre-Crack  
1900 Cycles



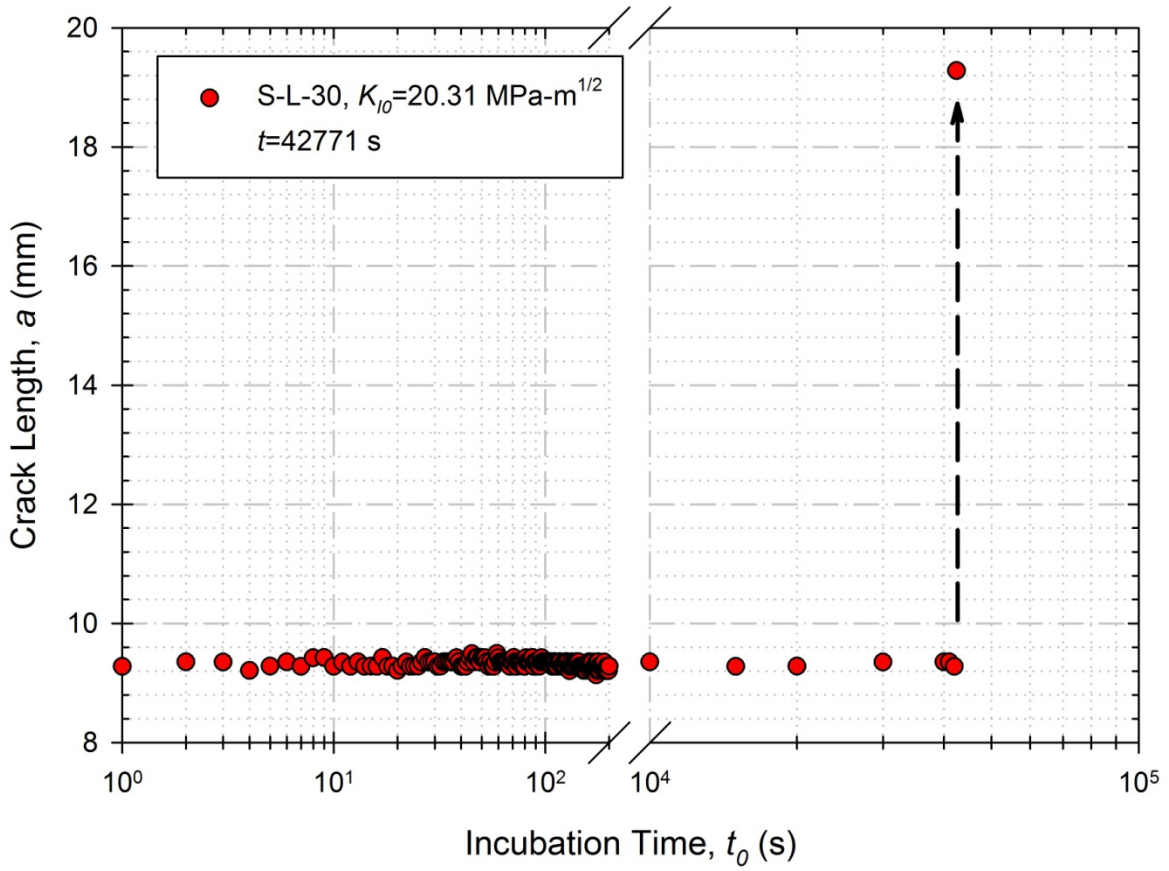
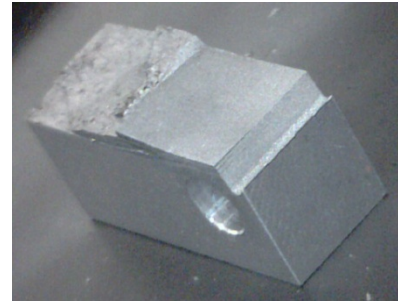
**S-L-28**  
 Environment: Liquid Hg  
 $K_{I0} = 20.88 \text{ MPa}\cdot\text{m}^{1/2}$   
 (19.08 ksi-in<sup>1/2</sup>)  
 Result: Test Stopped



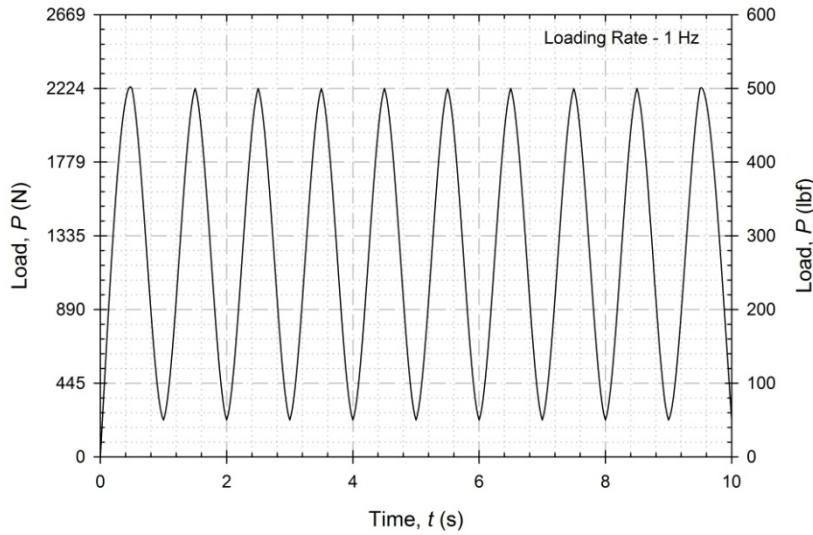
Fatigue Pre-Crack  
1800 Cycles



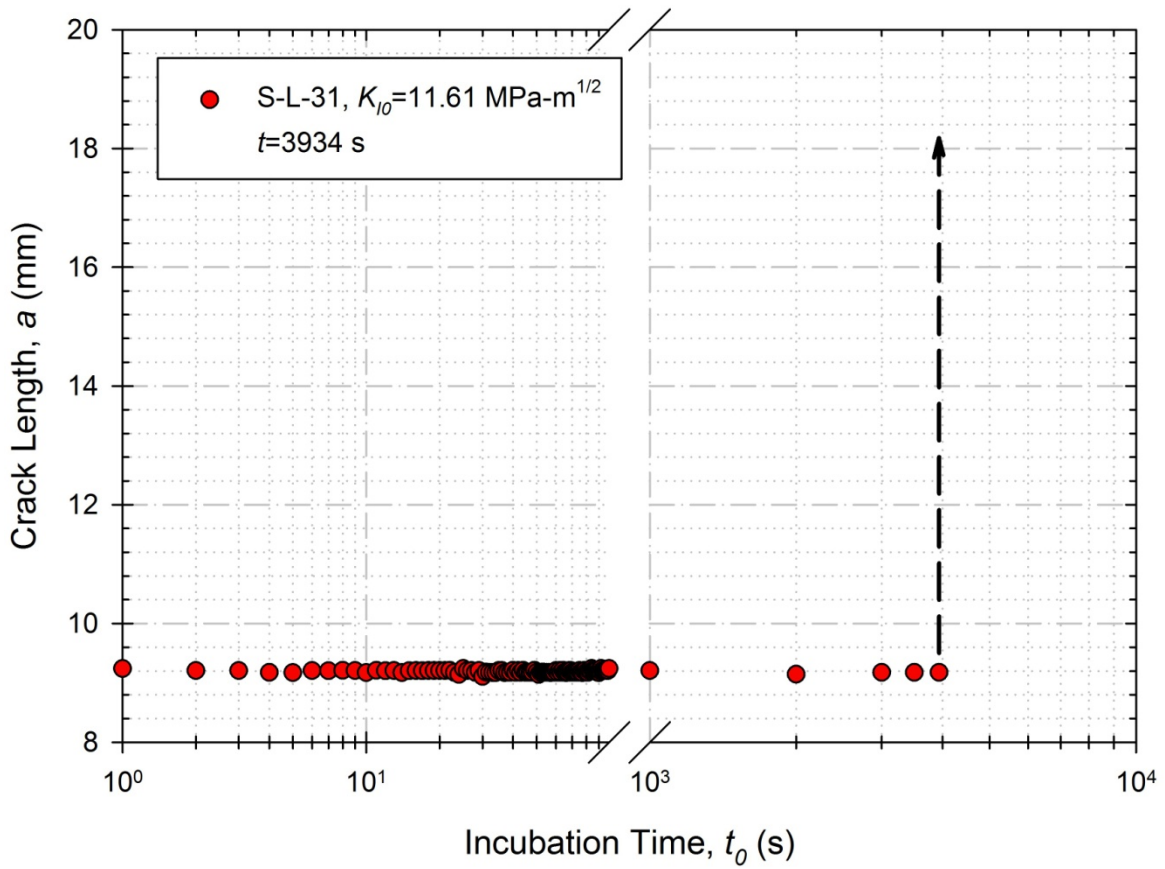
**S-L-30**  
 Environment: Liquid Hg  
 $K_{I0} = 20.31 \text{ MPa}\cdot\text{m}^{1/2}$   
 (18.49 ksi-in $^{1/2}$ )  
 Result: Successful  
 Incubation



Fatigue Pre-Crack  
1900 Cycles



**S-L-31**  
Environment: Liquid Hg  
 $K_{I0} = 11.61 \text{ MPa}\cdot\text{m}^{1/2}$   
(10.57 ksi-in<sup>1/2</sup>)  
Result: Invalid  
Incubation



**APPENDIX B**  
**SEM IMAGES**

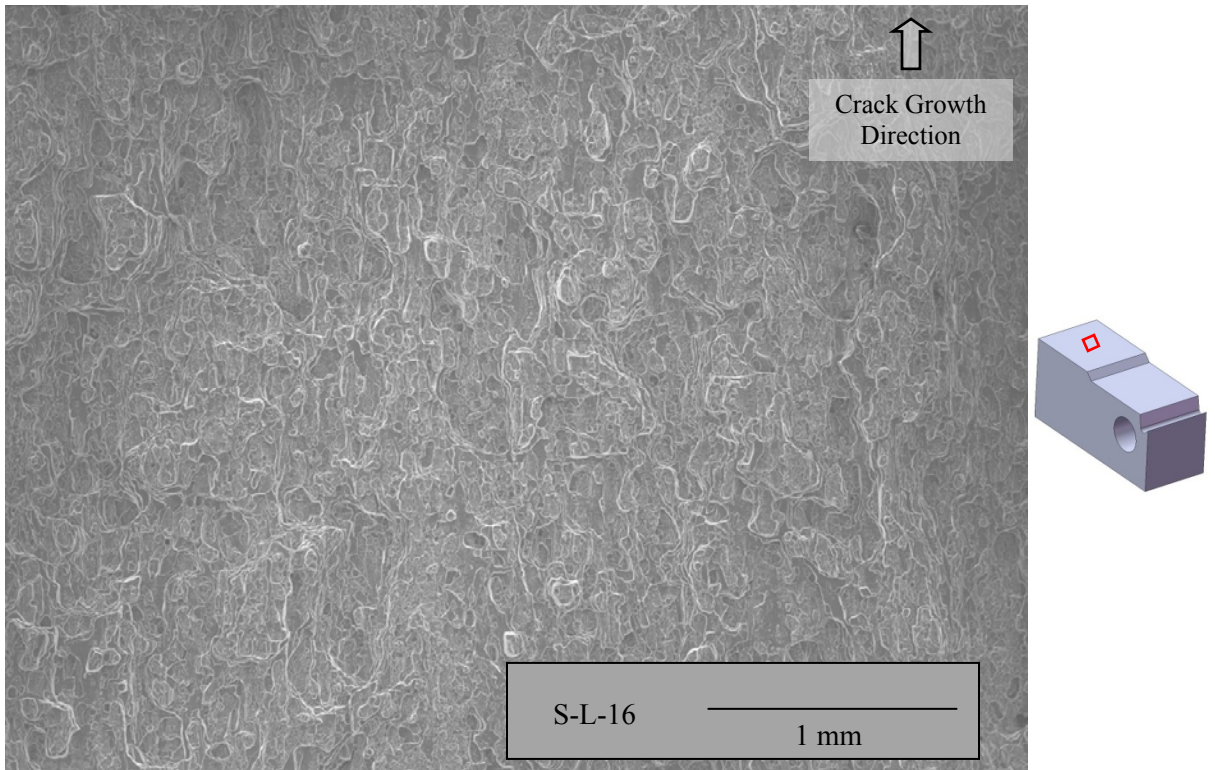


*Figure B.1: View of fast fracture surface of a specimen fractured in air.*

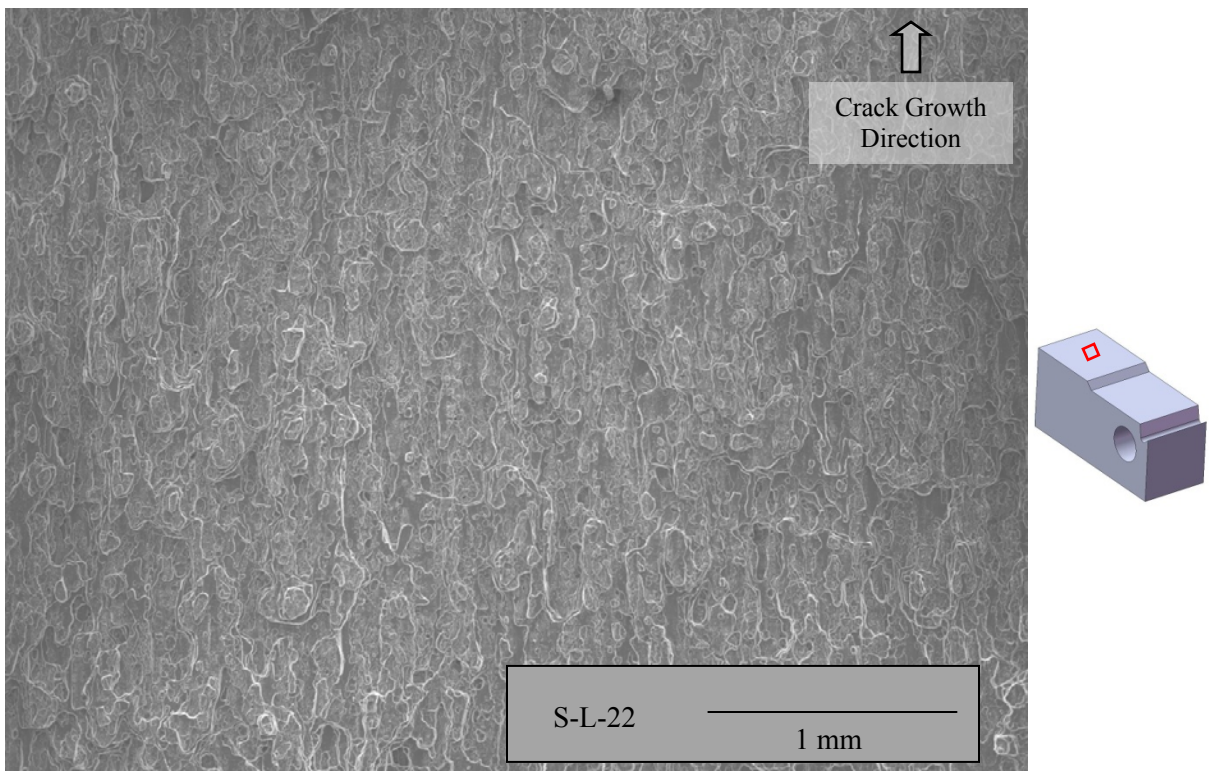


*Figure B.2: View of fast fracture surface of a specimen fractured in air.*

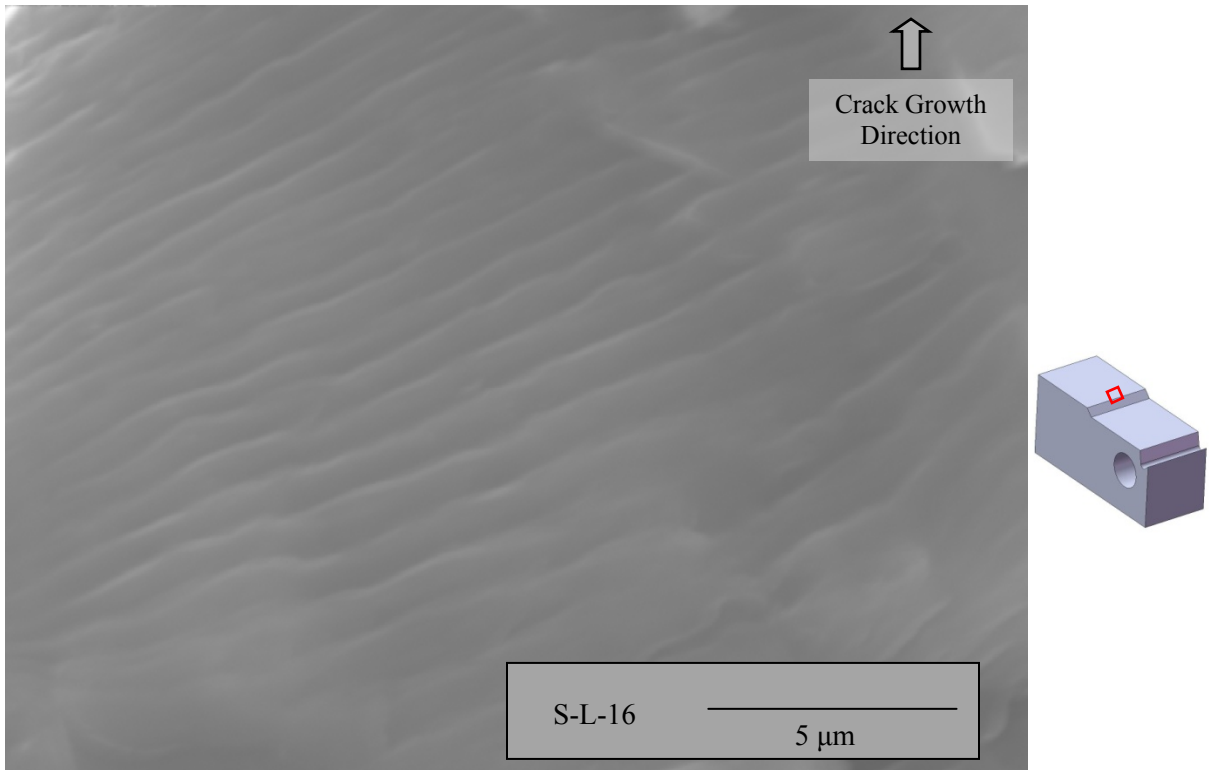


**Figure B.3:** Fatigue pre-crack region of a specimen fractured in air.

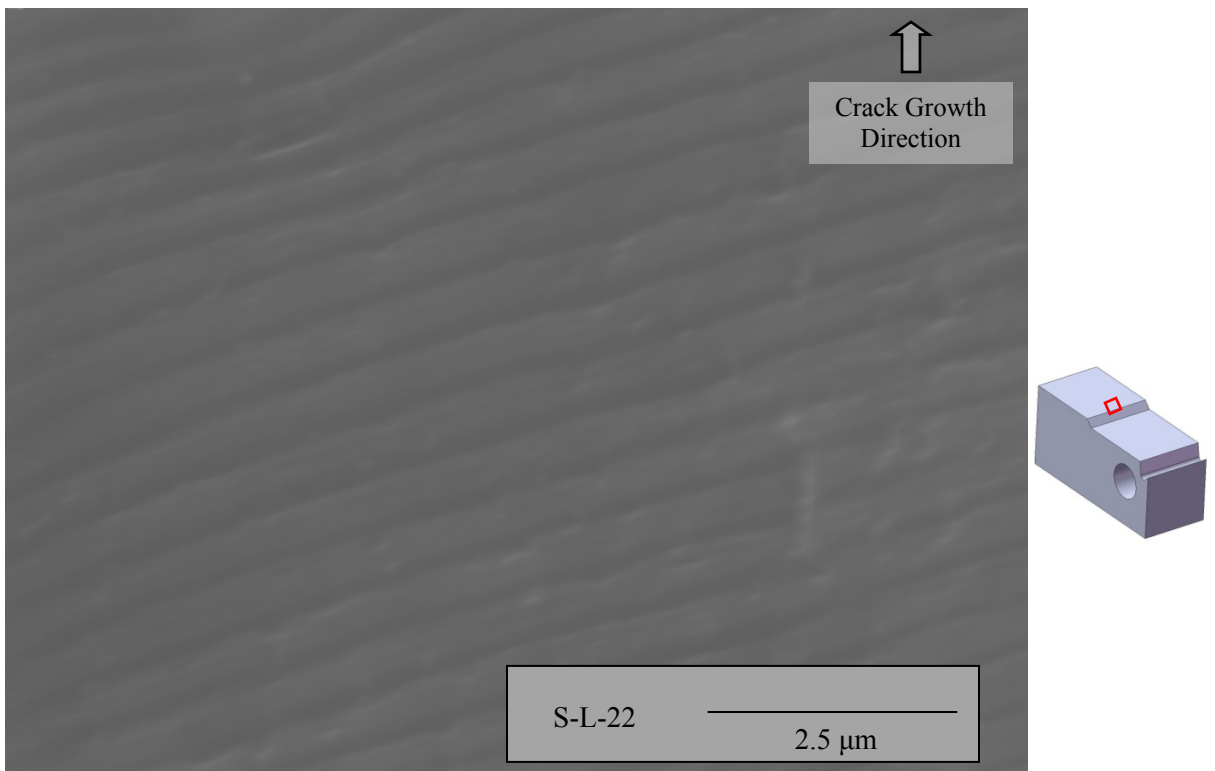


**Figure B.4:** Fatigue pre-crack region of a specimen fractured in air.

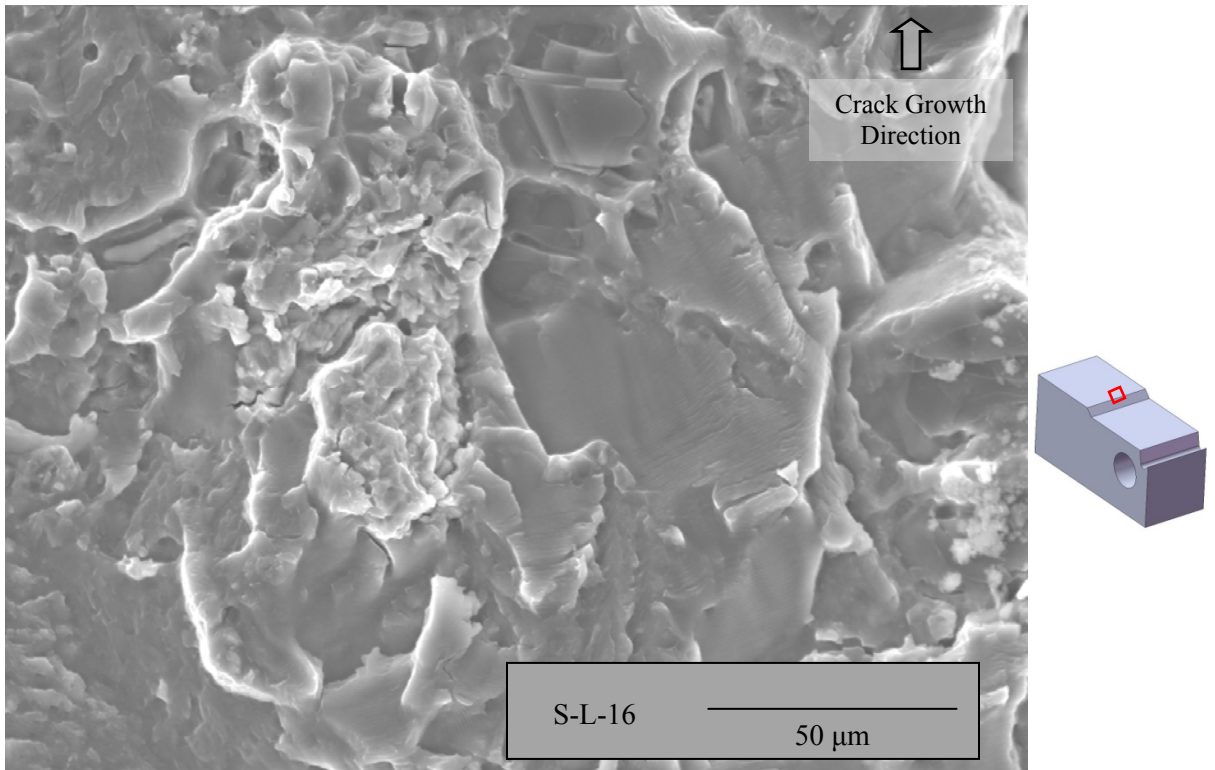


*Figure B.5: Low magnification of a pre-crack region of a specimen fractured in air.*

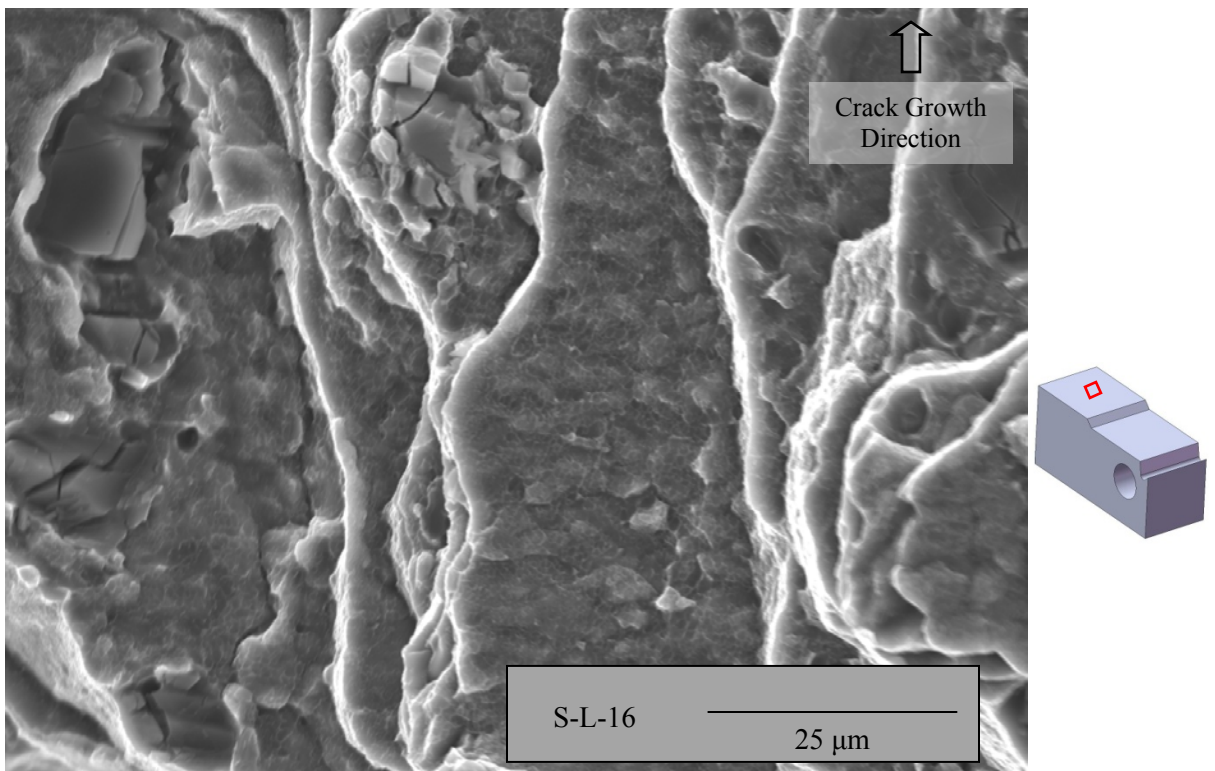


*Figure B.6: Fast fracture region of a specimen fractured in air.*

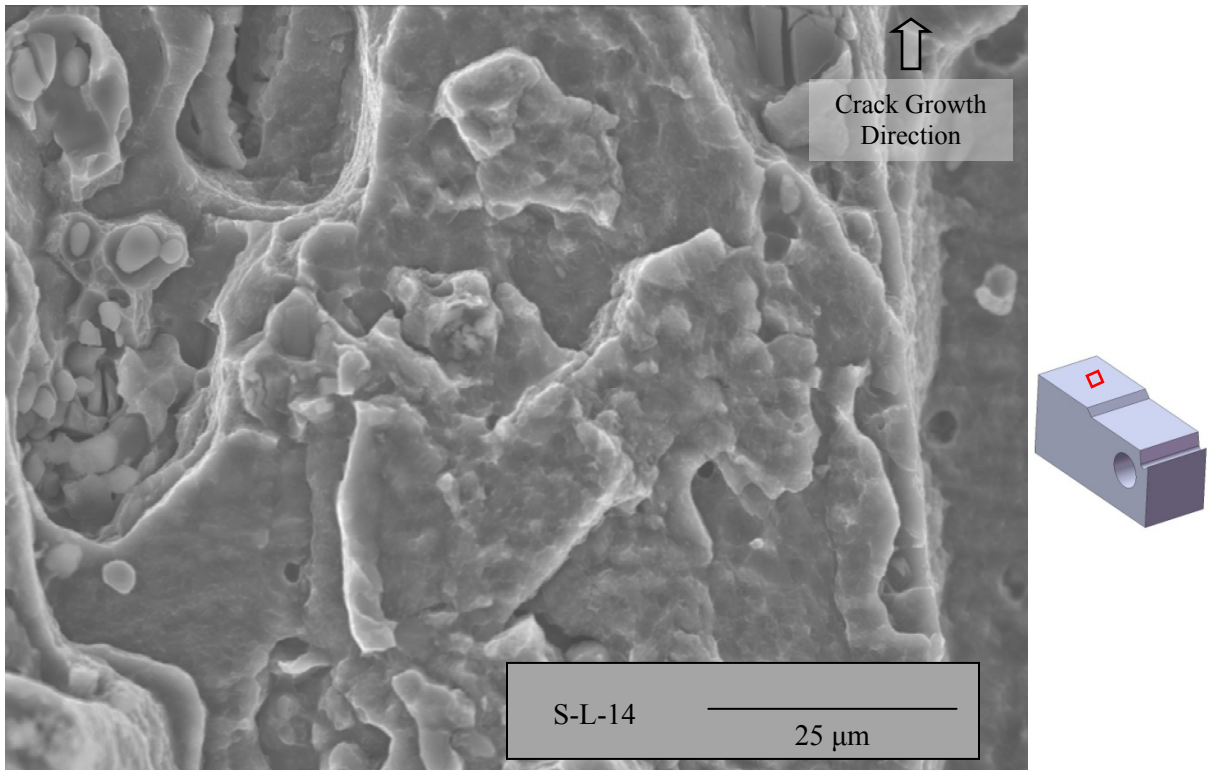


**Figure B.7:** Fast fracture region of a specimen fractured in 3.5% NaCl.

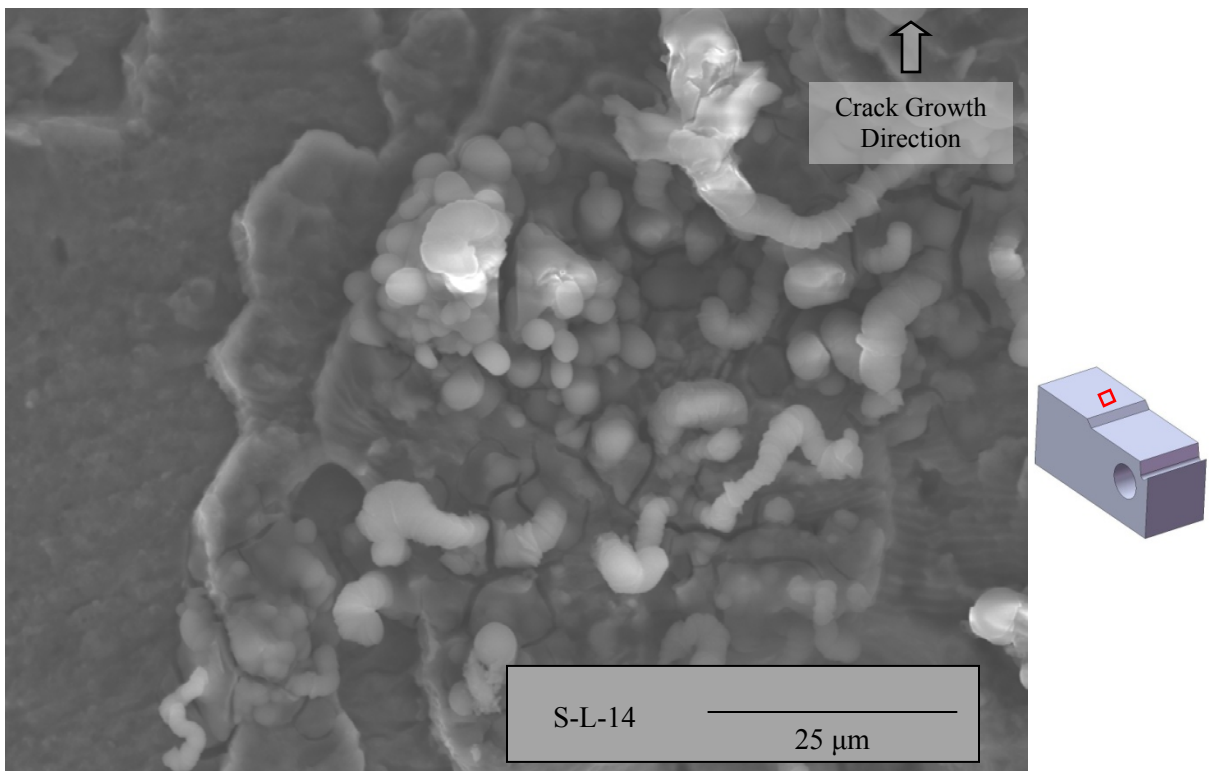


**Figure B.8:** Transition region from pre-crack to fast fracture of a specimen fractured in 3.5% NaCl.

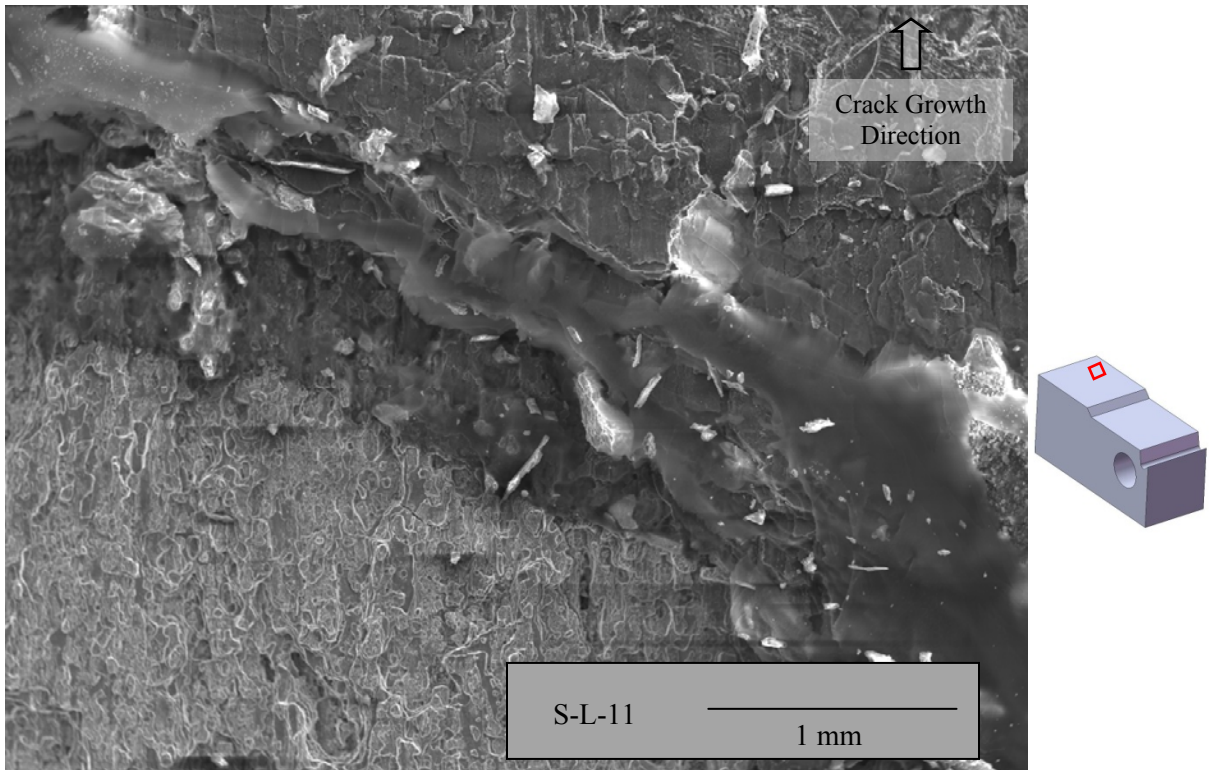


*Figure B.9: Transition between failure modes of a specimen fractured in liquid Hg.*

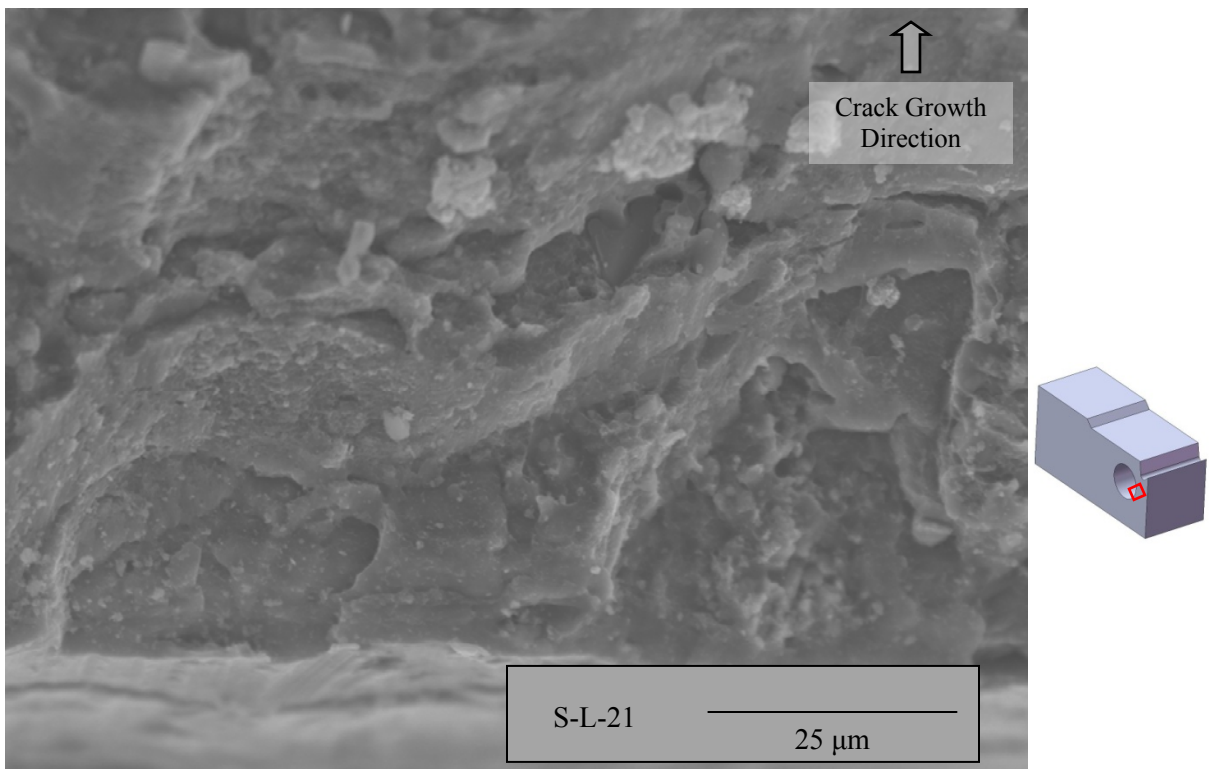


*Figure B.10: Failure of a specimen through the load pin hole in liquid Hg.*

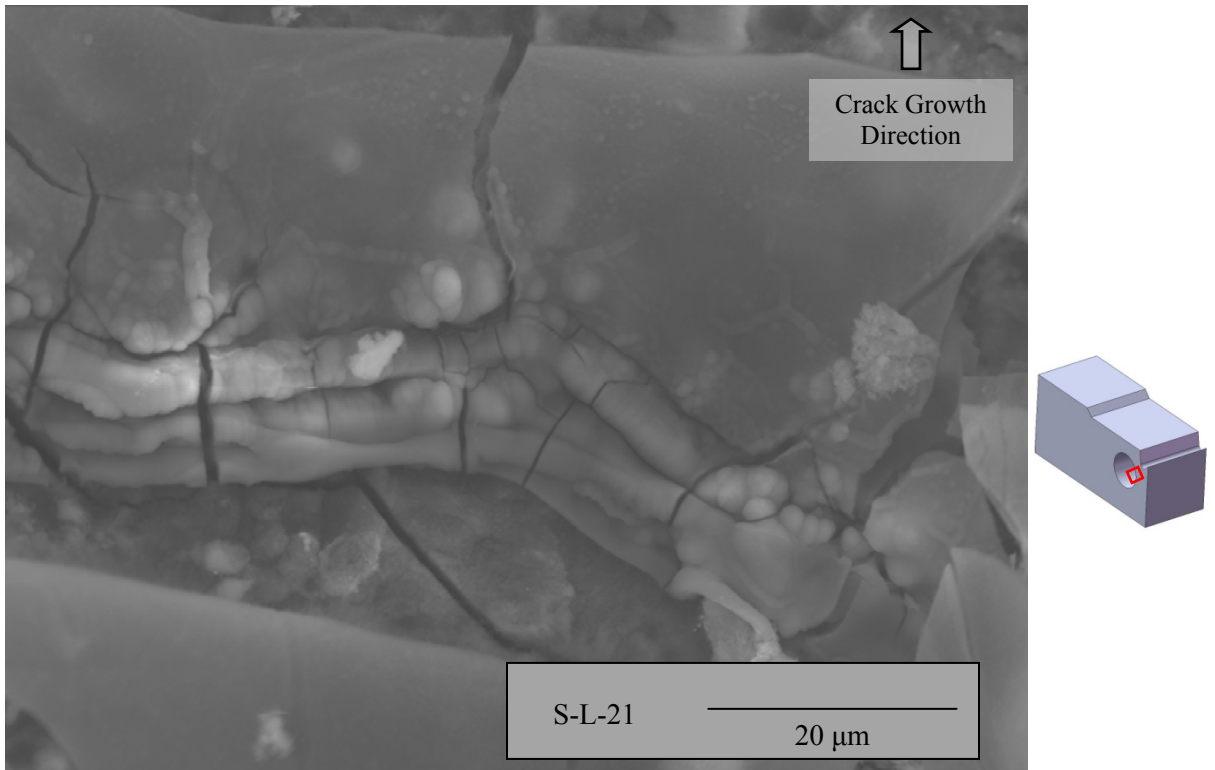


*Figure B.11: Crack initiation at the load pin hole of a specimen fractured in liquid Hg.*

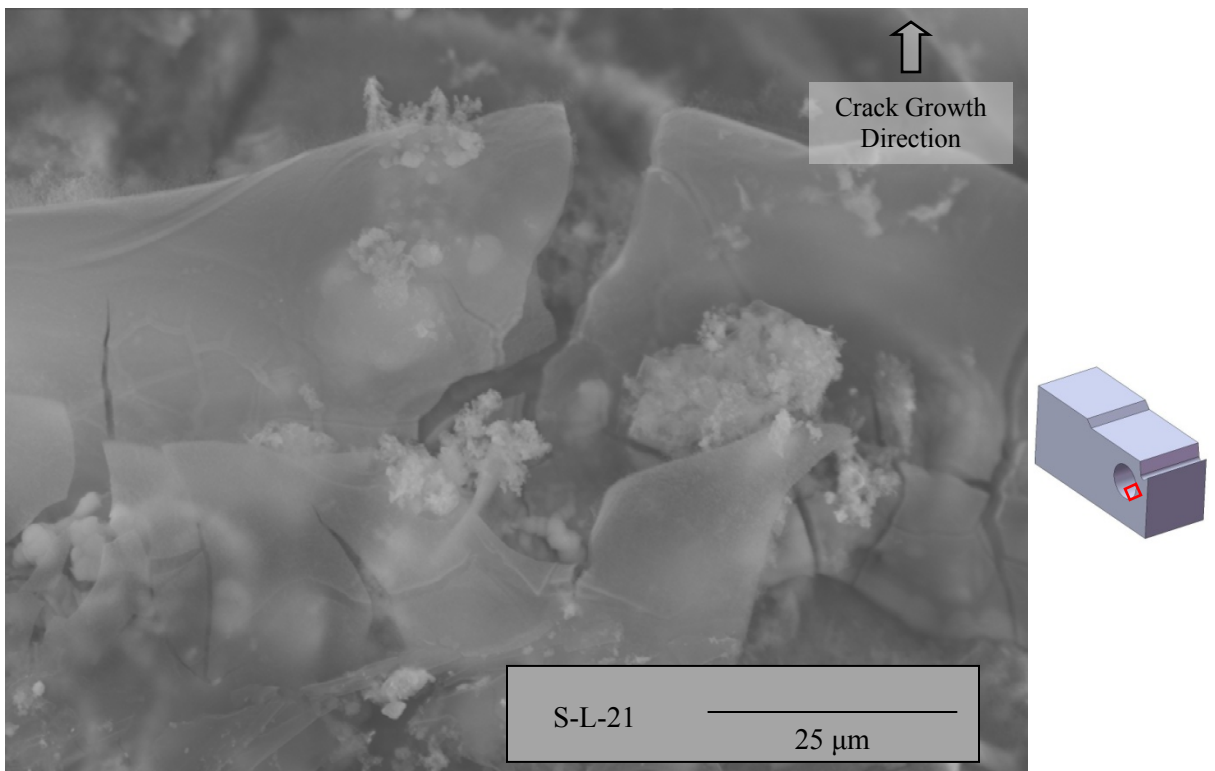


*Figure B.12: Crack initiation at the load pin hole of a specimen fractured in liquid Hg.*

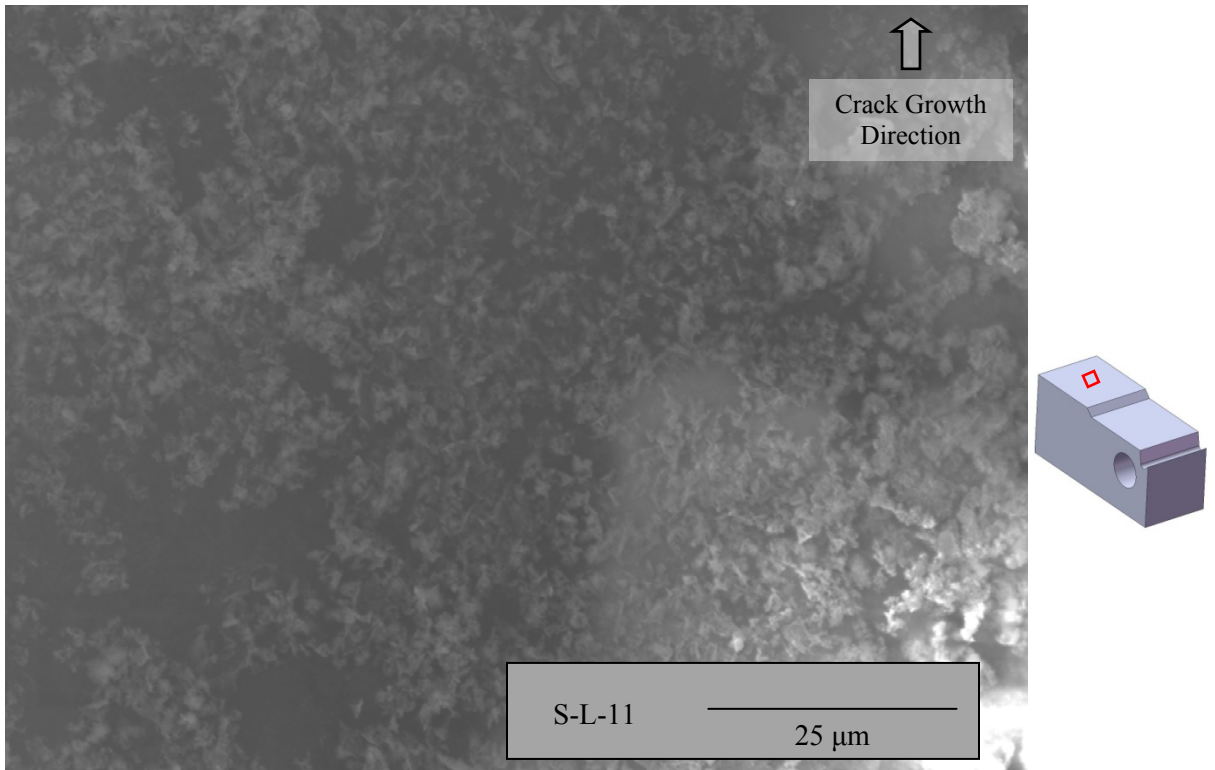


**Figure B.13:** Flat surface observed in the fast fracture region of a specimen fractured in liquid Hg.

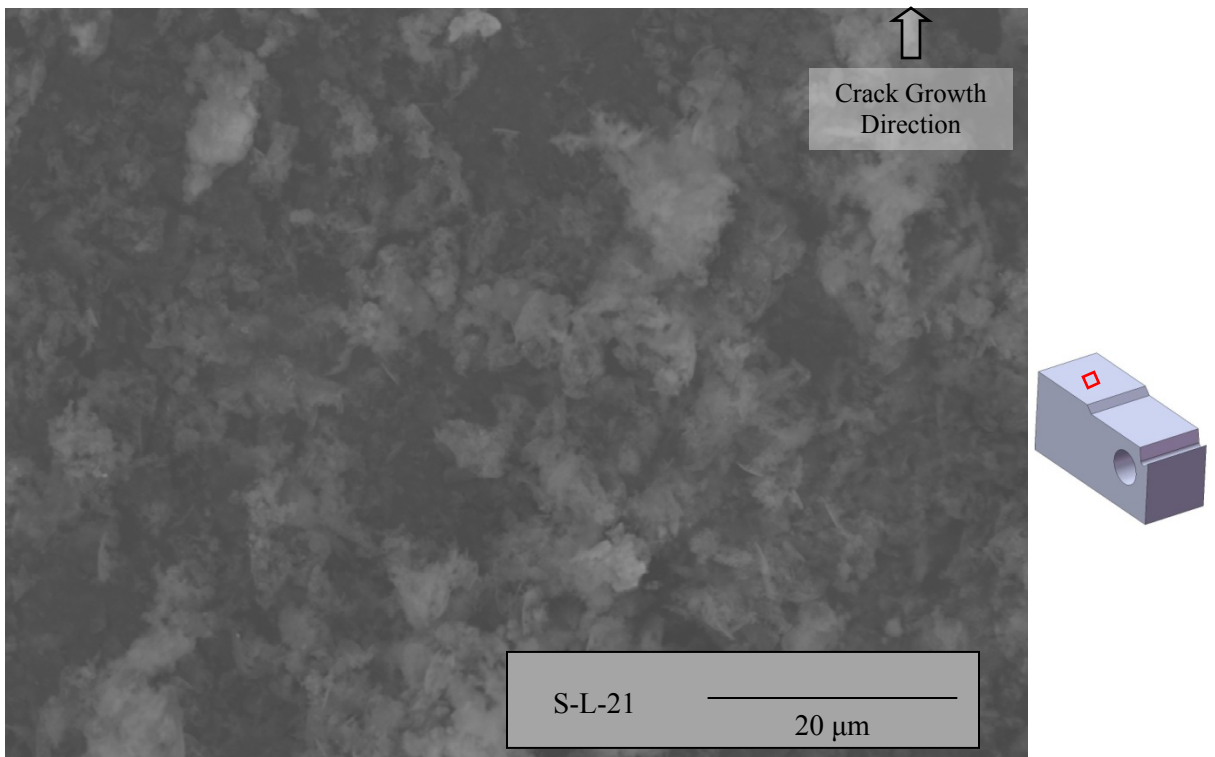


**Figure B.14:** Flat surface observed in the fast fracture region of a specimen fractured in liquid Hg.

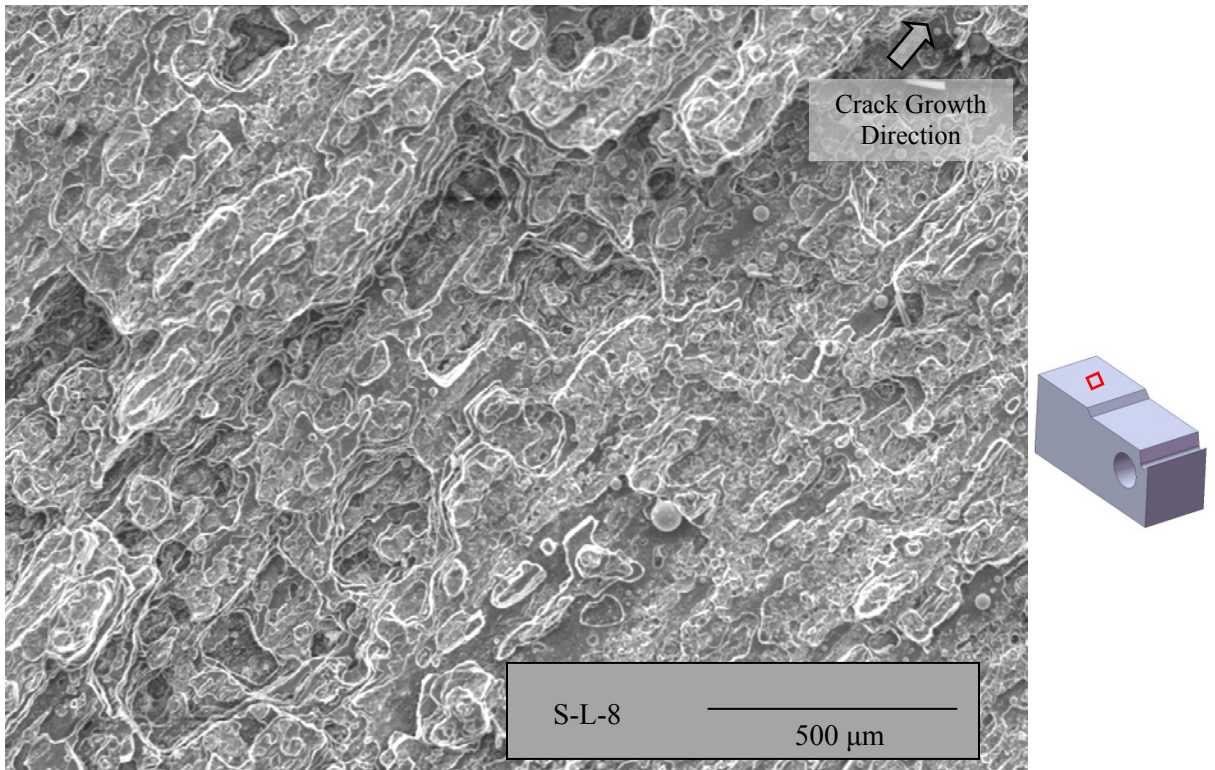


**Figure B.15:** View of fast fracture surface of a specimen fractured during an incubation experiment liquid Hg.

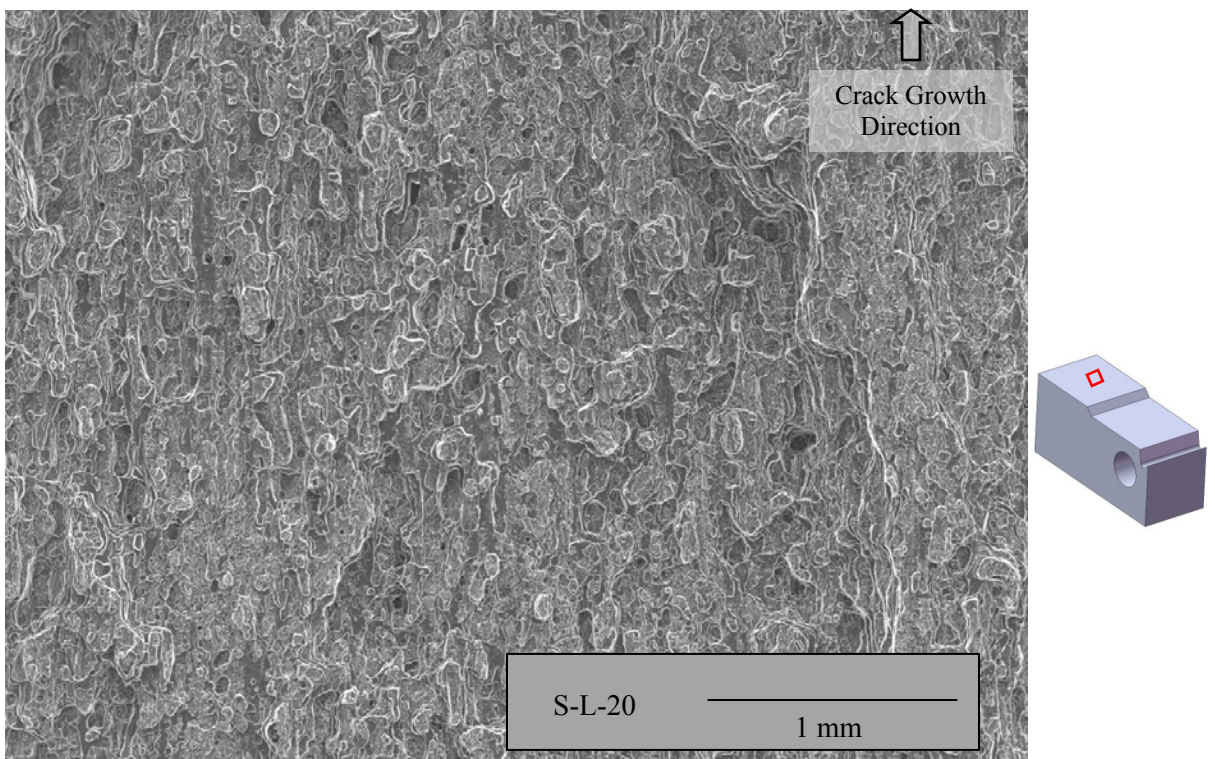


**Figure B.16:** View of fast fracture surface of a specimen fractured during an incubation experiment liquid Hg.

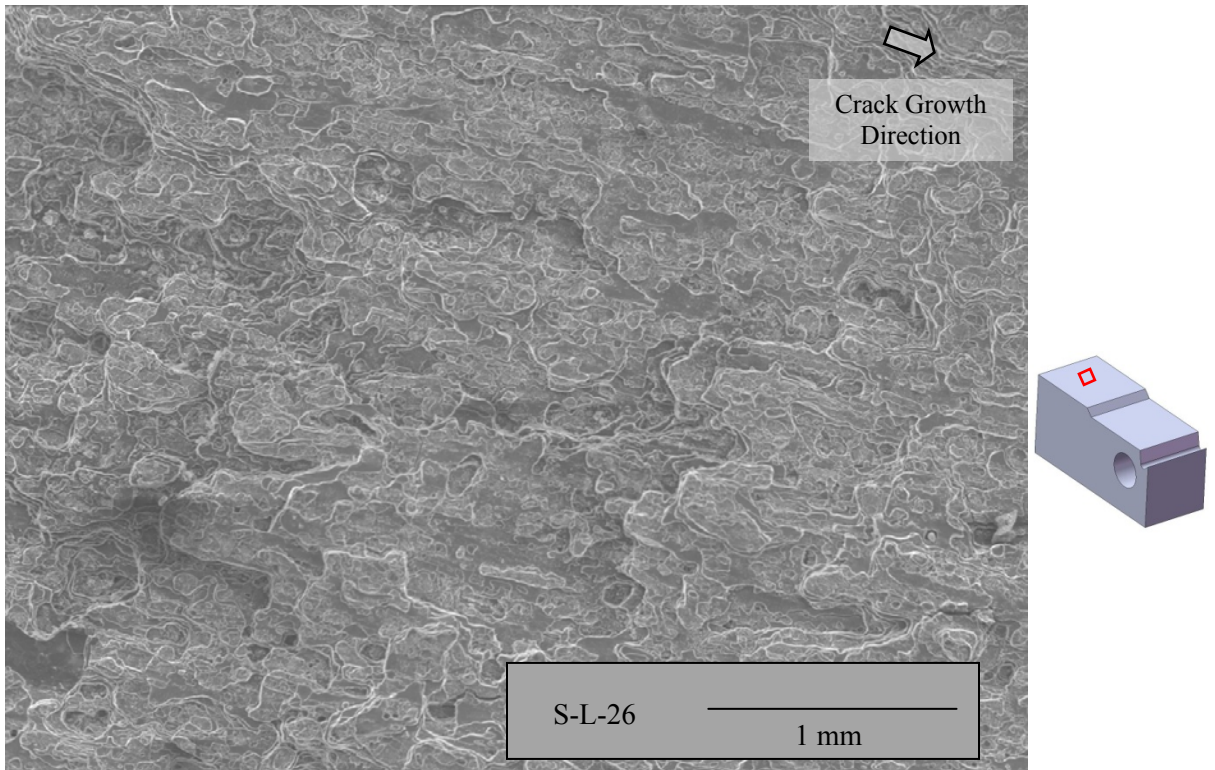


**Figure B.17:** View of fast fracture surface of a specimen fractured during an incubation experiment liquid Hg.

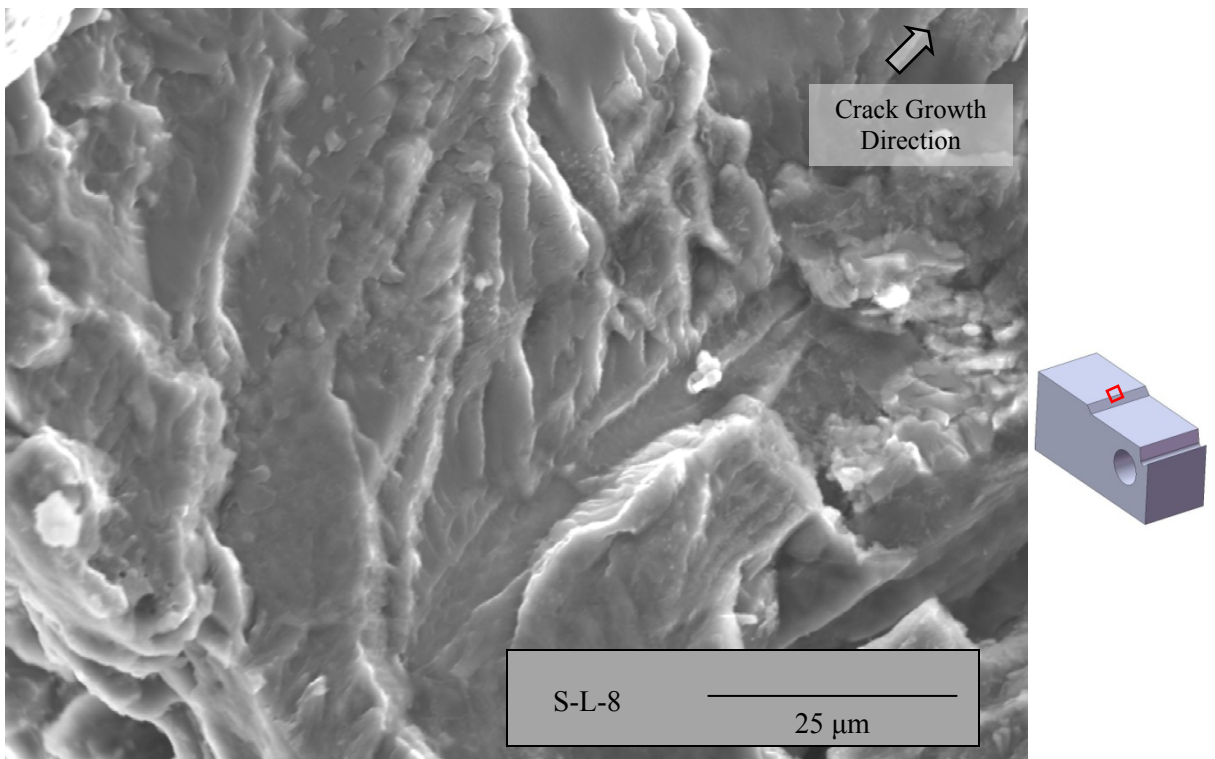


**Figure B.18:** Pre-crack region of a specimen fractured during an incubation experiment in liquid Hg.

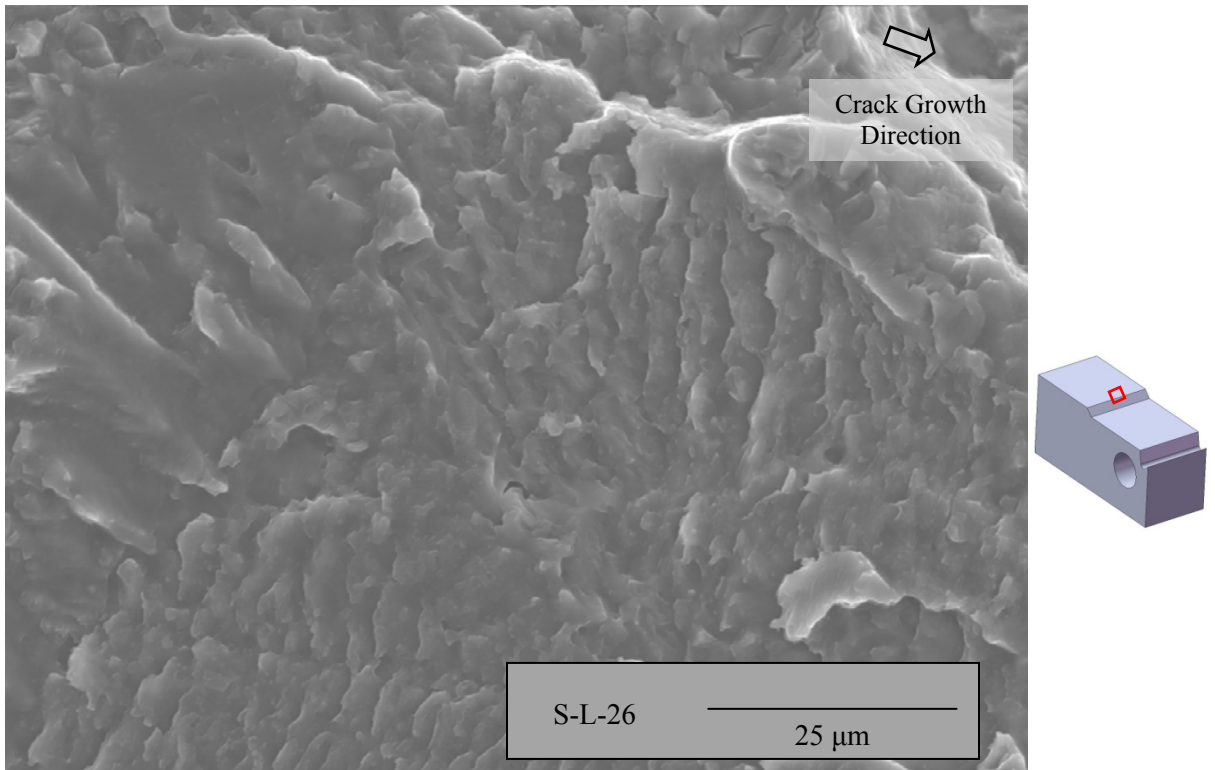


**Figure B.19:** Pre-crack region of a specimen fractured during an incubation experiment in liquid Hg.

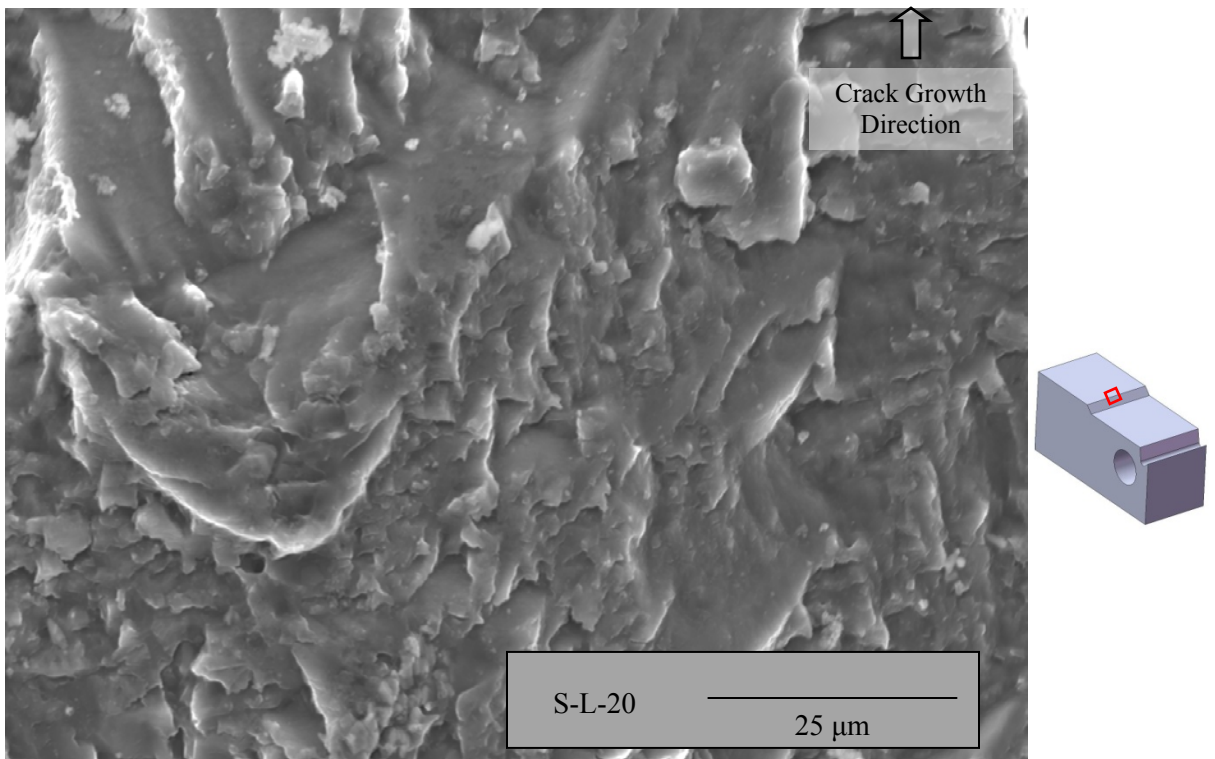


**Figure B.20:** Pre-crack region of a specimen fractured during an incubation experiment in liquid Hg.

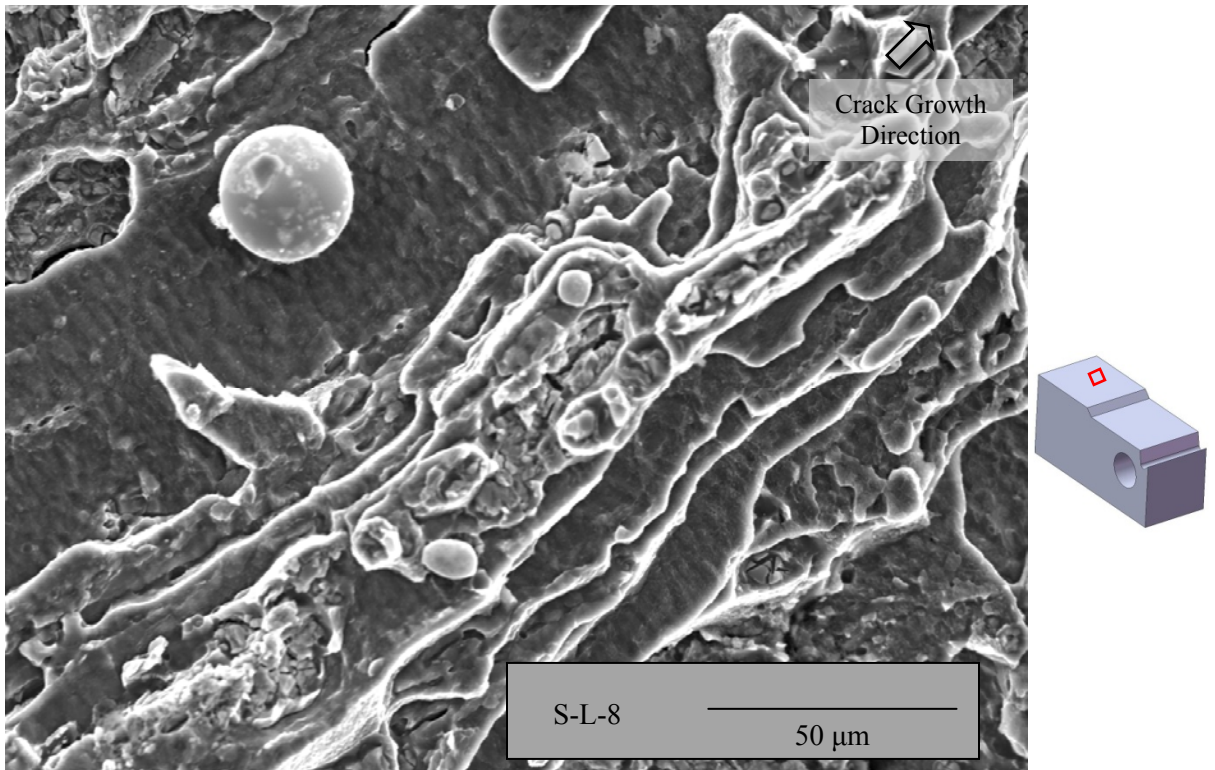


**Figure B.21:** Fast fracture region of a specimen fractured during an incubation experiment in liquid Hg.

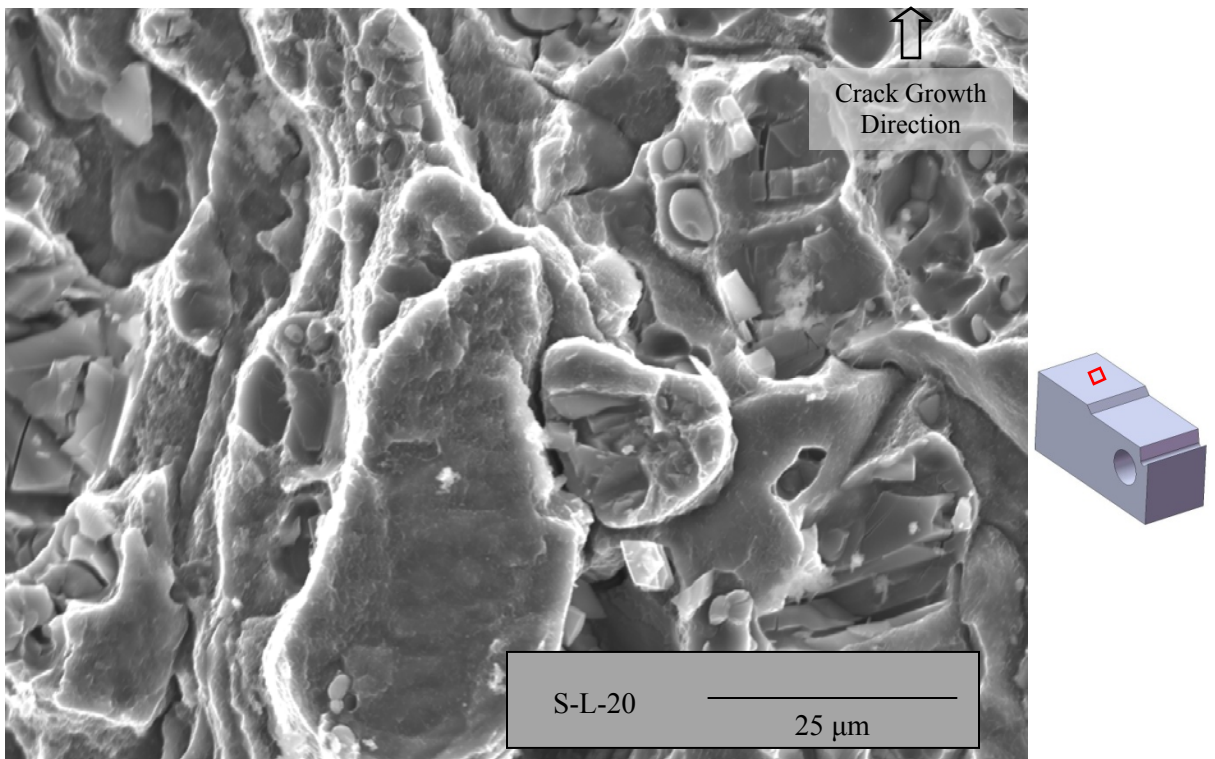


**Figure B.22:** Fast fracture region of a specimen fractured during an incubation experiment in liquid Hg.

## LIST OF REFERENCES

- ASM Handbook Volume 2, *Properties and Selection: Non-Ferrous Alloys and Special-Purpose Materials*, Seventh Printing, ASM International, Materials Park, OH, 2007.
- ASTM Standard E399, 1990 (1997), *Standard Test Method for Linear-Elastic Plane-Strain Fracture Toughness,  $K_{Ic}$ , of Metallic Materials*, ASTM International, West Conshohocken, PA, DOI: 10.1520/E0399-90R97.
- ASTM Standard E647, 2000, *Standard Test Method for Measurement of Fatigue Crack Growth Rates*, ASTM International, West Conshohocken, PA, DOI: 10.1520/E0647-00.
- ASTM Standard E1457, 2000, *Standard Test Method for Measurement of Creep Crack Growth Rates in Metals*, ASTM International, West Conshohocken, PA, DOI: 10.1520/E1457-00.
- ASTM Standard E1290, 1999, *Standard Test Method for Crack-Tip Opening Displacement (CTOD) Fracture Toughness Testing*, ASTM International, West Conshohocken, PA, DOI: 10.1520/E1290-99.
- Benson, B.A. and Hoagland, R.G., *Crack Growth Behavior of a High Strength Aluminum Alloy during LME by Gallium*, Scripta Metallurgica, Volume 23 (11), pp. 1943-1948, 1989.
- Dowling, N.E., *Mechanical Behavior of Materials*, 3<sup>rd</sup> ed., Upper Saddle River, NJ: Pearson Prentice Hall, 2007.
- English, J.J. and Korbin, G., *Liquid Mercury Embrittlement of Aluminum*, Materials Performance, Volume 28 (2), pp. 62-63, 1989.
- Glickman, E.E. and Goryunov, Yu. V., *Mechanism of Embrittlement by Liquid Metals and Other Manifestations of the Rebinder Effect in Metal Systems*, Soviet Materials Science, Volume 14 (4), pp. 355-364, 1978.
- Gordon, A.P., *Engineering Fracture Mechanics in Design: A Historical Perspective*, Engineering Fracture Mechanics in Design, Lecture/Class, UCF, Orlando, Fl, 2009.
- Gordon, D.E., et al., *Effects of Salt Water Environment and Loading Frequency on Crack Initiation in 7075-T651 Aluminum Alloy and Ti-6Al-4V*, Corrosion Cracking Conference, ASM International, pp. 157-165, 1986.
- Gordon, P. and An, H., *The Mechanisms of Crack initiation and Crack Propagation in Metal-Induced Embrittlement of Metals*, Metallurgical Transactions A, Volume 13A, pp. 457-472, 1982.
- Hagedorn, K.E. and Pardun, M., *Some aspects of fracture mechanics research during the last 25 years*, Journal of Iron and Steel Research, Volume 69 (4), pp. 206-213, 1998.

- Jiang, Y. et al., *Stress Corrosion of AISI 4340 Steel and 7075-T651 Aluminum Alloy*, ONR Workshop on Fatigue and Corrosion Cracking, New York, June 2009.
- Johnson, R., *Aging Aircraft and structural worthiness*, Society of Automotive Engineers, Volume 100 (1), 1991, pp. 2731-2748.
- Joseph, B. et al., *Liquid Metal Embrittlement: A State-of-the-Art Appraisal*, EPJ Applied Physics, Volume 5 (1), pp. 19-31, 1999.
- Kamdar, M.H., *Liquid-Metal Embrittlement*, Metals Handbook, ASM, Volume 13, pp. 171-184, 1987.
- Kane, R.D., et al., *Use of Slow Strain Rate Tests to Evaluate the Embrittlement of Aluminum and Stainless Alloys in Process Environments Containing Mercury*, ASTM Special Technical Publication, n1210, pp. 181-192, 1993.
- Kapp, J., et al., *Crack Growth Behavior of Aluminum Alloys Tested in Liquid Mercury*, Journal of Engineering Materials and Technology, Volume 108 (1), pp. 37-43, 1986.
- Kolman, D.G. and Chavarria, R., *Liquid-Metal Embrittlement of 7075 Aluminum and 4340 Steel Compact Tension Specimens by Gallium*, Journal of Testing and Evaluation, Volume 30 (5), pp.452-456, 2002.
- Krishtal, M.A., et al., *Diffusion of Impurity Atoms along Dislocations in Aluminum*, Physics of Metals and Metallography, Volume 36 (5), pp. 191-193, 1973.
- Krupowicz, J.J., *Slow Strain Rate Fracture Characteristics of Steel and Aluminum Alloys Tested in Mercury Environments*, Journal of Engineering Materials and Technology, Volume 111 (July), pp. 229-234, 1989.
- Liu, Y. and Hoagland, R.G., *Transient and Intermittent Crack Growth during Embrittlement of 7075-T651 Aluminum by Mercury*, Scripta Metallurgica, Volume 23 (3), pp. 339-344, 1989.
- Lynch, S.P., *Effect of Environment on Fracture – Mechanisms of Liquid Metal Embrittlement, Stress-Corrosion Cracking and Corrosion-Fatigue*, International Conference on Fracture 4, Pergamon Press, Volume 2, pp. 859-866, 1977.
- Lynch, S.P., *Failures of Structures and Components by Environmentally Assisted Cracking*, Engineering Failure Analysis, Volume 1 (2), pp. 77-90, 1994.
- Lynch, S.P., *Failures of Engineering Components Due to Environmentally Assisted Cracking*, Practical Failure Analysis, Volume 3 (5), pp. 33-42, 2003.
- Lynch, S.P. and Moutsos, S., *A Brief History of Fractography*, Journal of Failure Analysis and Prevention, Volume 6 (6), pp. 54-69, 2006.

- Malu, M.K. and Preece, C.M., *The Role of Solute Additions to Aluminum on its Embrittlement by Mercury*, Materials Science and Engineering, Volume 11 (4), pp. 223-226, 1973.
- MTS Insight Electromechanical Testing Systems, MTS Systems Corporation, April 2009 Brochure, <<http://www.mts.com/insight>>.
- Murphy, E., *Aging Aircraft: too old to fly?*, IEEE Spectrum, June 1989, pp. 28-31.
- Nichols, H. and Rostoker, W., *On the Mechanism of Crack Initiation in Embrittlement by Liquid Metals*, Acta Metallurgica, Volume 9 (5), pp. 504-509, 1961.
- Nichols, H. and Rostoker, W., *Mercury Embrittlement of an Al-4½ Pct Mg Alloy*, Metallurgical Society of American Institute of Mining, Metallurgical and Petroleum Engineers – Transactions, Volume 230 (1), pp. 251-253, 1964.
- Otto, H.E., et al., *Embrittlement of Aluminum Alloys by Mercury*, ASM Transactions, Volume 55 (3), pp. 429-438, 1962.
- Papirno, R., et al., *Fracture in Axial Compression Testing of Cylinders*, Compression Testing of Homogenous Materials and Composites, ASTM STP 808, Richard Chait and Ralph Papirno, Eds., American Society for Testing and Materials, pp. 40-63, 1983.
- Perez, N., *Fracture Mechanics*, Boston, MA: Kluwer Academic Publishers, 2004.
- Petit, J. and Zeghloul, A., *Environmental and Microstructural Influence on Fatigue Propagation of Small Surface Cracks*, ASTM Special Technical Publication, n 1049, pp. 334-346, 1990.
- Robertson, W.M., *Propagation of a Crack Filled with Liquid Metal*, Metallurgical Society of American Institute of Mining, Metallurgical and Petroleum Engineers – Transactions, Volume 236 (10), pp. 1478-1482, 1966.
- Romaniv, O., et al., *Kinetic Effects in the Mechanics of Delayed Fracture of High-Strength Alloys*, Soviet Materials Science, Volume 12 (4), pp. 347-360, 1976.
- Sanford, R.J., *Principles of Fracture Mechanics*, Upper Saddle River, NJ: Pearson Education Inc., 2003.
- Sawayanagi, F. and Hasiguti, R.R., *Diffusion of Mercury, Thallium and Lead in Aluminum*, Nihon Kinzoku Gakkai shi., Volume 42 (12), pp. 1155-1160, 1978.
- Speidel, M., *Stress Corrosion Cracking of Aluminum Alloys*, Metallurgical Transactions A, Volume 6 A (4), pp. 631-651, 1975.

- Stoloff, N.S. and Johnston, T.L., *Crack Propagation in a Liquid Metal Environment*, Acta Metallurgica, Volume 11 (4), pp. 251-256, 1963.
- Sumpter, J.D.G., and Kent, J.S., *Prediction of Ship Brittle Fracture Casualty Rates by a Probabilistic Method*, Journal of Marine Structures, Volume 17 (8), pp. 575-589, 2004.
- Vander Voort, G.F., *Metallography, Principles and Practice*, Materials Park, OH: ASM International, 1999.
- Wanhill, R.J.H., *Cleavage of Aluminum Alloys in Liquid Mercury*, Journal of Corrosion Science and Engineering, Volume 30 (10), pp. 371-378, 1974.
- Westwood, A.R.C and Kamdar, M.H., *Concerning Liquid Metal Embrittlement, particularly of Zinc Monocrystals by Mercury*, Philosophical Magazine, Volume 8 (89), pp. 787-804, 1963.
- Wheeler, D.A. and Hoagland, R., *Observations of Cracking Behavior and Non-Unique Cracking Thresholds during the LME of Aluminum*, Scripta Metallurgica, Volume 20, pp. 1433-1438, 1986.
- Wheeler, D.A., *Stable Crack Growth during the Liquid Metal Embrittlement of Aluminum by Mercury*, PhD Dissertation, The Ohio State University, 1987.
- Wheeler, D.A., et al., *Evidence for Crack Tip Oxidation Effects During the Liquid Metal Embrittlement of AA 7075 Aluminum Alloy by Mercury*, Corrosion, Volume 45 (3), pp. 207-212, 1989.
- Wheeler, D.A. et al., *Effect of Solid Metal Strength Level on the Liquid Metal Embrittlement of Aluminum by Mercury*, Scripta Metallurgica, Volume 22, pp. 533-538, 1988.
- Zweig, T., *A Universal Method for the Mechanical Preparation of Aluminum Alloy Specimens with High Edge Retention and their Subsequent Colour Etching*, Praktische Metallographie, Volume 38 (2), 2001.